ABSTRACT

ELECTRO-CHEMO-MECHANICS OF THE INTERFACES IN 2D-3D HETEROSTRUCTURE ELECTRODES

by
Vidushi Sharma

Unique heterostructure electrodes comprising two-dimensional (2D) materials and bulk three dimensional (3D) high-performance active electrodes are recently synthesized and experimentally tested for their electrochemical performance in metal-ion batteries. Such electrodes exhibit long cycle life while they also retain high-capacity inherent to the active electrode. The role of 2D material is to provide a supportive mesh that allows buffer space for volume expansions upon ion intercalation in the active material and establishes a continuous electronic contact. Therefore, the binding strength between both materials is crucial for the success of such electrodes. Furthermore, battery cycles may bring about phase transformations in the active electrodes. Thus, altering the characteristics of its existing interface with the 2D material. Conversely, surface characteristics of 2D material can also initiate new microstructural orders in the bulk electrodes. The resultant structural variations impact the overall functionality of the electrode. Obtaining an insight into the nature of these interfaces has become a necessity to design heterostructure electrodes for commercial applications. However, it is not practiced to date due to limitations imposed by experimental techniques.

The purpose of this research is to computationally investigate the interface between 2D materials with 3D bulk systems and highlight the implications of these interfacial attributes on electrode performance. The precise aims are: (i) determine interface strength between 2D materials and 3D active electrode in the light of phase transitions and surface

modifications; (ii) differentiate the electrochemical performance of heterostructure electrodes from their free counterparts; and (iii) develop new deep learning-based algorithm to model multiphasic interface systems. Key results of this research are quantitative interface strength values of selenium(Se) and silicon(Si) with 2D materials such as Graphene and MXene. First principle calculations show that bulk materials Se and Si bind with 2D materials with low interface strength, mostly below 0.6 J/m^2. The presence of out-of-plane surface functional groups on MXenes can further create stearic effects and low interface stability, resulting in curtailed interface strength. The vdW forces are the primary mode of binding at the interface of 2D materials. Next, a relation between the state of charge and interface structure of the Se-Graphene heterostructure electrode is presented for the potassium ion batteries. More atomic investigations into the 2D-3D interfaces reveal that the interface alone is a cause of crystalline distortions and new phase transitions in the bulk materials. These interfacial disorders cannot be accurately traced by empirical potentials. To overcome this gap, deep learning-based potential energy surfaces (PES) are developed from density functional theory(DFT) data of multiphasic tin(Sn)-Graphene interfaces. Developed PES predict the energies of new interfaces with close to first principles accuracy.

ELECTRO-CHEMO-MECHANICS OF THE INTERFACES IN 2D-3D HETEROSTRUCTURE ELECTRODES

by
Vidushi Sharma

A Dissertation
Submitted to the Faculty of
New Jersey Institute of Technology
in Partial Fulfillment of the Requirements for the Degree of
Doctor of Philosophy in Mechanical Engineering

Department of Mechanical and Industrial Engineering

December 2021

.

APPROVAL PAGE

ELECTRO-CHEMO-MECHANICS OF THE INTERFACES IN 2D-3D HETEROSTRUCTURE ELECTRODES

Vidushi Sharma

Dibakar Datta, Dissertation Advisor — Date
Assistant Professor of Mechanical Engineering, New Jersey Institute of Technology

---

Shawn A. Chester, Committee Member — Date
Associate Professor of Mechanical Engineering, New Jersey Institute of Technology

---

Eon Soo Lee, Committee Member — Date
Associate Professor of Mechanical Engineering, New Jersey Institute of Technology

---

Lin Dong, Committee Member — Date
Assistant Professor of Mechanical Engineering, New Jersey Institute of Technology

---

Fatemeh Ahmadpoor, Committee Member — Date
Assistant Professor of Mechanical Engineering, New Jersey Institute of Technology

---

Cristiano L. Dias, Committee Member — Date
Associate Professor of Physics, New Jersey Institute of Technology

---

Joshua Young, Committee Member — Date
Assistant Professor of Chemical and Materials Engineering, New Jersey Institute of Technology

BIOGRAPHICAL SKETCH

Author: Vidushi Sharma

Degree: Doctor of Philosophy

Date: December 2021

Undergraduate and Graduate Education:

- Doctor of Philosophy in Mechanical Engineering,
  New Jersey Institute of Technology, Newark, NJ, 2021

- Master of Technology in Molecular Engineering and Advanced Chemical Analysis,
  National Institute of Technology, Kurukshetra, India, 2017

- Bachelor of Technology in Biotechnology,
  Banasthali University, India, 2015

Major: Mechanical Engineering

Peer-reviewed Publications:

V. Sharma, D. Mitlin, D. Datta, Understanding the Strength of the Selenium–Graphene Interfaces for Energy Storage Systems, *ACS Langmuir*, 2021, 37, 6, 2029–2039.

V. Sharma, D. Datta, Variation in the Interface Strength of Silicon with Surface Engineered Ti3C2 MXenes, *Physical Chemistry Chemical Physics*, 2021, 23, 5540-5550.

P. Solanky, V. Sharma, K. Ghatak, J. Kashyap, D. Datta, The Inherent Behavior of Graphene Flakes in Water: A Molecular Dynamics Study, *Computational Material Science*, 2019, 162, 140-147.

K. Ghatak, S. Basu, T. Das, V. Sharma, H. Kumar, D. Datta, Effect of Cobalt Content on the Electrochemical Properties and Structural Stability of NCA Type Cathode Materials, *Physical Chemistry Chemical Physics*, 2018, 20, 22805-22817.

V. Sharma, K. Ghatak, D. Datta, Amorphous Germanium as a Promising Anode Material for Sodium Ion Batteries: A First Principle Study, *Journal of Materials Science*, 2018, 53: 14423.

V. Sharma, D. Mitlin, D. Datta, Correlating Electrochemistry with Microstructural Changes in Graphene-enclosed Selenium Cathode for Potassium Ion Battery. *Manuscript under preparation.*

V. Sharma, J. Datta, D. Datta, Developing Deep Learning Potentials for Graphene based 2D-3D Interface Systems. *Manuscript under preparation.*

Book Chapters:

V. Sharma, K.Ghatak, D. Datta, Book Chapter 17, Two Dimensional Materials and its Heterostructures for Energy Storage, *Synthesis, Modelling and Characterization of 2D Materials and their Heterostructures*, 1st Edition, 2020, USA: Elsevier.

S. Basu, V. Sharma, Book Chapter 8, Monte Carlo Methods in Two-Dimensional Materials, *Synthesis, Modelling and Characterization of 2D Materials and their Heterostructures*, 1st Edition, 2020, USA: Elsevier.

Conference Presentations (Oral):

V. Sharma, D. Datta, 'Performance of Seleneium-Graphene Composite as Potassium ion Battery Cathode', *Material Research Society (MRS), Virtual Spring Meeting*, 2021, April, 18-23, 2021.

V. Sharma, D. Datta, 'Interface Strength of Silicon with Surface Engineered Two-Dimensional Materials', *American Physics Society (APS),* March 15-19, 2021.

V. Sharma, K. Ghatak, D. Datta, 'Modeling of Graphene-Anode Interface for Ion Battery Technology', *Society of Engineering Science (SES),* St. Louis, October 13-15, 2019.

V. Sharma, K. Ghatak, D. Datta, 'Current Collector Interface for Phase Changing Tin Anode in Sodium Ion Batteries: Insight from First Principle Calculations', *The Electrochemical Society (ECS),* Dallas, Texas, May, 26-30, 2019.

V. Sharma, D. Datta, 'Chemo-mechanical Modeling of Defective Graphene for Energy Storage in Lithium-ion Battery', *American Physics Society* (APS March Meet), Boston, Massachusetts, March, 4-7, 2019.

V. Sharma, K. Ghatak, D. Datta, 'Chemo-mechanical Modeling of 2D Materials based Anodes for Lithium-ion Battery', *International Conference on Functional Nanomaterials (ICFNM-2019)*, IIT-BHU, India, February, 22-25, 2019, ***First Prize in Oral Presentation Category.***

V. Sharma, K. Ghatak, S. Nadimpalli, D. Datta, 'Atomistic and Molecular Modeling of Amorphous Germanium as Negative Electrode for Sodium Ion Battery', *13th WCCM/ 2nd PACCM 2018*, New York City, USA, July 22 - 27, 2018.

V. Sharma, K. Ghatak, D. Datta, 'Computational Modeling of 2D Materials and their Heterostructures for Sustainable Energy Storage: Opportunities and Challenges', *MRS Fall 2018*, Boston, Massachusetts, November, 25-30, 2018.

Conference Presentations before NJIT:

V. Sharma, A. Bhatia, M. Senthilkumar, J.K Kapoor, 'Effect of Increasing Methylene Linkage of diamine on Biological Activity of Salen Schiff bases: In vitro screening and Molecular docking studies', *Thematic Conference in Chemical Sciences (TC2S)*, IIT Ropar, India, May 15-16, 2017, ***Best Poster Presentation Award.***

A. Bhatia, V. Sharma, M. Senthilkumar, 'Acceptorless Dehydrogenation of Secondary Alcohols using Ruthenium-PTA Complexes in Aqueous Medium', *International Symposium on New Trends In Applied Chemistry (NTAC-2017)*, Kochi, India, February, 9-11, 2017.

V. Sharma, M. Senthilkumar, J.K Kapoor, 'Synthesis and Complexation studies of PTA included Schiff Bases', *International Conference on Recent Trends in Chemical Sciences (ICRCS- 2017)*, Bikaner, India, January 12-13, 2017.

V. Sharma, S. Srivastava, 'Chemical Sensing Based ABC Swarm Intelligence Algorithm for Cancer Treating Nanorobots', *1st International Conference On Innovative Advancements in Engineering and Technology (IAET-2014),* Jaipur, India, March 7-8, 2014.

V. Sharma, 'Biocompatibility of Nanorobots', *15th Annual Conference Of Society Of Statistics, Computer and Applications*, Banasthali, India, February 24-26, 2013, ***Best Poster Presentation Award.***

Conference Publications before NJIT:

V. Sharma, S. Srivastava, Chemical Sensing Based ABC Swarm Intelligence Algorithm for Cancer Treating Nanorobots, *INROADS*, Special Issue, January-June, 2014, Volume 3, 1, 101-105.

To my parents
Alok Kumar Sharma and Barkha Sharma
and
My dearest little sister
Arushi Sharma

ACKNOWLEDGMENT

My dream to become a doctorate is coming to a full circle and there are several people I would like to acknowledge here without whom this Dissertation wouldn't have been possible. First and foremost, I would like to thank my Ph.D. advisor Dr. Dibakar Datta for giving me this opportunity and constant support throughout the graduate years. I have greatly benefitted from being part of his research group. My research life was easier because of his patience, mentorship and academic freedom he provided to explore the unknown. I would also like to thank my graduate advisor Dr. Zhiming Ji for his constant guidance and help.

I would like to extend my gratitude to my committee members Dr. Shawn A Chester, Dr. Eon Soo Lee, Dr. Lin Dong, Dr. Fatemeh Ahmadpoor, Dr. Cristiano Dias and Dr. Joshua Young for their time and thoughtful feedbacks that enhanced my research. Special thanks to Dr. Siva P.V. Nadimpalli who taught me basics of mechanical engineering and enlightened me regarding the essence of Ph.D. research. I would also like to thank my collaborator Dr. David Mitlin from U.T. Austin for giving my projects guidance and sharing his experience. Another person who periodically had conversations with me and provided his valued insight, Dr. Susanta Ghosh from Michigan Technological University must know I am very grateful.

I am happy to acknowledge the organizations that provided me the financial and technical resources throughout these years. I thank Extreme Science and Engineering Discovery Environment (XSEDE) for the computational facilities (Award Number – DMR180013), Department of Mechanical Engineering at NJIT for Teaching Assistanceship, National Science Foundation (NSF Award Number 1911900) for financial

support, High-Performance Computing (HPC) facilities managed by Academic and Research Computing Systems (ARCS) in the Department of Information Services and Technology (IST) of the New Jersey Institute of Technology (NJIT).

I am thankful to have met many supportive peers who listened to my research problems and gave their best advice. Thanks to Dr. Kamalika Ghatak for mentoring my DFT work in the first year which established the foundation of my research. My research group members Mr. Jatin Kashyap, Nil Dhankecha (graduated) and Joy Datta have been wholly supportive.

Lastly and most importantly, I want to express my heartfelt gratitude to my parents and sister for their love, encouragement, and emotional support. If it were not for their patience, I wouldn't have embarked on this journey. They listened to my research finding and constantly gave their feedback. Knowing that my family knows what I am accomplishing every step of the way was the biggest inspiration to keep going forward.

TABLE OF CONTENTS

TABLE OF CONTENTS
(Continued)

TABLE OF CONTENTS
(Continued)

TABLE OF CONTENTS
(Continued)

LIST OF TABLES

LIST OF FIGURES

LIST OF FIGURES
(Continued)

LIST OF FIGURES
(Continued)

Figure **Page**

LIST OF FIGURES
(Continued)

Figure **Page**

LIST OF FIGURES
(Continued)

Figure **Page**

LIST OF FIGURES
(Continued)

Figure **Page**

LIST OF FIGURES
(Continued)

LIST OF FIGURES
(Continued)

Figure **Page**

LIST OF FIGURES
(Continued)

Figure **Page**

CHAPTER 1

BACKGROUND

1.1 Lithium-Ion Batteries and Challenges

Global energy demand is constantly challenging existing energy storage systems and calling for new innovations. With the imminent exhaustion of fossil fuel and its subsequent environmental consequences, there has been enormous stress on eco-friendly, renewable, cheap, and portable secondary battery that could provide energy storage for variable applications. The last few decades saw the rise of Lithium-ion batteries (LIBs) as market-leading battery technology. They have become the primary power source in portable electronic devices and electric vehicles owing to their high output voltages, high power density, long cycle life, high-rate capability, low maintenance, and wide working temperature ranges [1-3]. As expected, LIB earned the prestigious Nobel Prize in Chemistry for three Scientists: John B. Goodenough, M. Stanley Whittingham, and Akira Yoshino in 2019 for their foundational work towards wireless, fossil fuel-free society.

Like all electrochemical devices, LIB comprises an anode, cathode, separator, electrolyte, and two current collectors (positive being a cathode and negative being anode), as shown in Figure 1.1. The anode and cathode in LIB store the lithium in a state of charged or discharged, respectively. During charging, the lithium ions move from the cathode to the anode through the electrolyte and the separator while electrons flow from the positive electrode (cathode) to the negative electrode (anode) via the outer circuit. At the anode, Li ion gets reduced to Li atoms and intercalate inside the anode material. The primary role of a separator is to block the flow of electrons inside the battery. During the discharging

process, Li atoms get oxidized to Li ions to move to cathode across electrolyte and separator while electrons move to the cathode in the outer circuit. Commercially, lithium-cobalt-oxide, $LiCoO_2$ (LCO) cathode and graphite anode were first to be recognized due to their excellent intercalation nature and reasonable capacities of 274 $mAhg^{-1}$ and 372 $mAhg^{-1}$, respectively [4, 5]. The search for efficient electrodes with higher capacities and stability has been ongoing since the LIB discovery[1]. However, after 4 decades of research and development, there exist two primary concerns associated LIBs [6, 7] :

(i) Current commercial LIBs fall short of meeting the automotive industry's capacity and power density demands.

(ii) With the ever-increasing demand for LIBs, there have been concerns about depleting Lithium (Li) reserves and the cost associated with this technology.

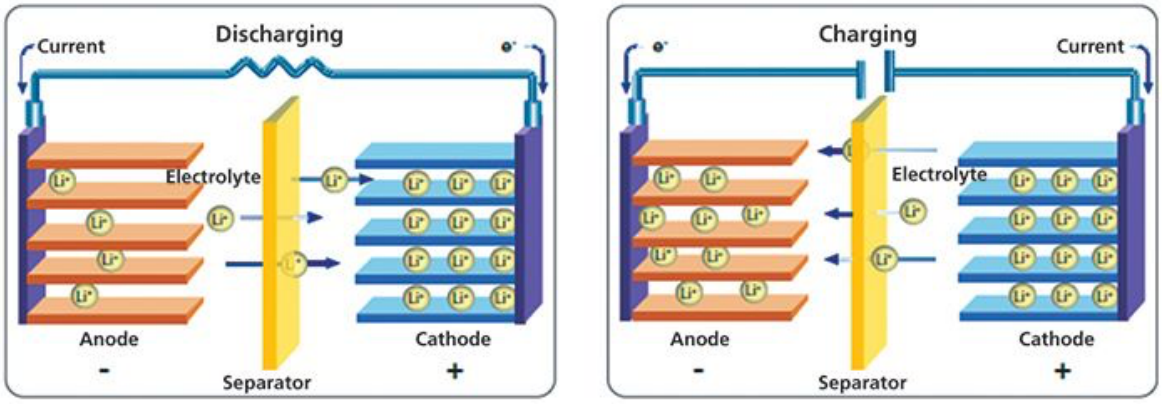

Figure 1.1 Schematic representation of charge and discharge kinetics in Lithium-ion battery (LIB). Li ions shuttle between cathode and anode across electrolyte and separator. *Source: [8]*

The first concern with regards to LIBs dictates finding stable electrodes with high capacity among next generation materials. LIB cathodes must have the ability to intercalate lithium (Li) ions reversibly without causing significant changes to the atomic structure. As

such, LCO is one of the well-studied cathode materials that has essential properties responsible for commercial success, such as low self-discharge, higher discharge voltage, around 500-700 deep discharge cycle life, and relatively high theoretical specific capacity as well as volumetric capacity [9, 10]. Yet, some of the drawbacks associated with LCO are its low thermal stability, rapid capacity loss with cycling, and the presence of Co [11], which makes it not only an expensive material but also very toxic. Beyond LCO, there are more commonly used lithium metal oxides with pure or a combination of transition metals such as cobalt (Co), nickel (Ni), manganese (Mn), iron (Fe), and titanium (Ti) which offer cheaper, eco-friendly and structurally stable cathode alternatives [12]. In the other end of LIBs, the primary and most accepted anode is a graphite system with a specific capacity of 372 $mAhg^{-1}$ for fully lithiated graphite, LiC_6 [13]. This capacity is not sufficient for vehicular applications where the demands are in the order of thousands of $mAhg^{-1}$. Bulk materials anodes such as Silicon (Si) offer a very high specific capacity (3000 $mAhg^{-1}$) but suffer from huge volume expansion of the order 300% and subsequent mechanical failures associated with volumetric strains [14].

The second LIB concern demands the world to address the problem of Li shortage. Lately, sodium-ion batteries (NIBs) and potassium-ion batteries (KIBs) have garnered interest as alternatives to LIBs for small-scale energy applications owing to the earthly abundance of sodium (Na) and potassium (K) metals [15-18]. Although the energy density of NIB and KIB is generally lower than that of LIB, high energy density becomes less critical for small-scale energy applications [19]. Energy storage mechanism for NIB and KIB is alike LIBs, except for the ion carriers. Both Na and K are heavier than Li, which greatly differentiates the electrode intercalation mechanism and diffusion kinetics in these

battery systems. Therefore, while most LIB electrodes can be tailored for NIB and KIB electrodes, they mostly lack the necessary structural design for long-term stability due to large atomic size of intercalating Na/K atoms [19].

1.2 Heterostructure Electrodes

With ever-increasing technological demands, we greatly rely on new and composite materials to model systems possessing advanced properties with an increased life cycle. These composites materials are modeled in fore-seen design and ratio to tune the system properties to one of our requirements for the respective application that range from automotive industry to aerospace, packaging, electronics, biotechnology, flexible sensors, and further [20]. Similarly, the development of 'next-generation' electrodes by combining materials into heterostructure is gaining attention to enhance the energy and power density of existing battery technologies. Two or more materials are amalgamated in varied nano- and micro-structures, where each component can contribute in one or many ways as an active electrode [21, 22], composite additive and a binder [23-30], porous matrix [31], or even a current collector [32, 33]. To this end, silicon (Si) is an exemplar anode where issues of cycle life, capacity, volume expansion, pulverization and surface reactivity have been successfully addressed by nano-engineering strategies such as Si alloys [34], Si film composites [35], Si and carbon (C) nanoparticles composites [36], and porous Si mixed with carbon-based nanostructures [37]. LIB has Copper (Cu) at anode end as conventional choice for the current collector based on preferred operational voltages. The interface between electrode and current collector has been recognized as the primary determinant of mechanical longevity of a battery (see Figure 1.2). Maranchi et al. [38] studied the

efficiency of a-Si thin film electrode over Cu substrate and showed that Cu-Si delaminated over time as Si continuously expanded and contracted during battery cycles, leading to eventual failures. Cause of this delamination was recognized to be weak interface adhesion strength. Thus, efficient interfacial architecture needs to be designed which can provide electrode a window to accommodate large strains following repeated Li insertion/extraction while maintaining a continuous electrical contact. Incorporation of additional materials provide Si electrode a porous skeleton that allows it to expand/contract easily with low mechanical stresses and continuous electrical contact.

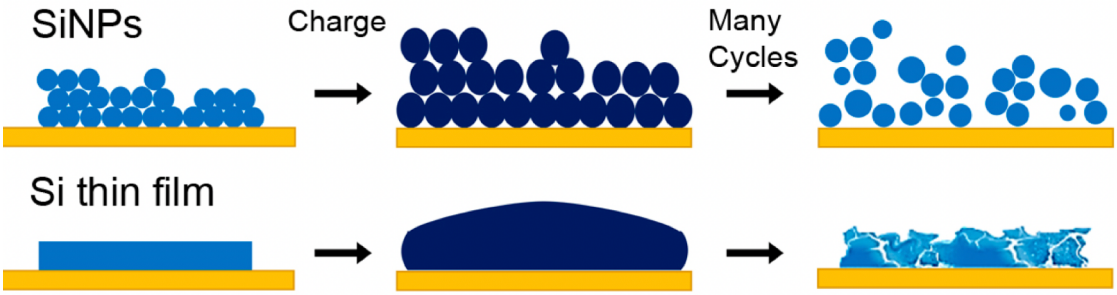

Figure 1.2 Morphological and volumetric changes during electrochemical cycling in the electrode of silicon nanoparticles and Si thin film that makes it prone to detachment from the Cu substrate.
Source: [27]

1.2.1 Graphene Based Heterostructure Electrodes

The groundbreaking discovery of multifunctional novel 2D material graphene in 2004 revolutionized the role of nanomaterials in almost every field [39]. Graphene is a hexagonal arrangement of sp^2 hybridized carbon atoms, or in simpler terms, it is a single atomic layer of a 3D graphite structure. It is characterized with exceptional mechanical strength, light-weight, unique electronic structure, high thermal conductivity, and advantageous surface

to volume ratio [40]. Following graphene, we have seen emergence of several 2D materials varying from single atomic thickness to five atomic thickness. All these materials have exhibited singular yet spectacular properties due to their high surface area and surface reactivities. In spite of being structurally diverse, these singular class of 2D materials can be stacked differently, held via van der Waals (vdW) interactions to form 2D heterostructures [41]. 2D heterostructures will not exhibit properties of any individual 2D material, but an entirely new set of characteristics which are a complement of all the materials stacked together and their respective arrangement. Therefore, resultant heterostructures have found applications in diverse fields of science and technology ranging from electronics to nanomedicine [42, 43]. 2D-2D heterostructures and 2D- three-dimensional (3D) bulk heterostructures are widely explored as electrodes for metal ion batteries since the interlayer space in such intercalating materials can be engineered effectively. Usually, two-dimensional (2D) materials are taken up as additive due to their prominent flexibility, good conductivity, lightweight and high surface Li diffusivity. New class of heterostructures comprise of graphene stacked with or encapsulating 3D bulk high capacity electrode material [44]. The earliest examples are of Si/graphene structures as graphene is a 2D alternative of graphite, a viable anode for LIB. Initial attempts to form Si/graphene heterostructure was done by simply mixing commercially available Si nanoparticles with graphene. Chou et al. 2009 show that Si/graphene heterostructure maintains a capacity of 1168 mAh g^{-1} and an average coulombic efficiency of 93% up to 30 cycles with Si maintaining a constant electrical contact [23]. Another study by Lee et al. 2010 [45] pointed out that Si/graphene anode can provide better cycle stability and storage capabilities if Si nanoparticles are well dispersed and portions of graphene sheets

stack to form a graphite-like network that would provide the structure a strong mechanical framework as shown in Figure 1.3. On the similar lines, next few years followed extensive creativity in creation of Si nanoparticles and graphene-based heterostructures followed by their electrochemical study as LIB anode, some of which are depicted in Figure 1.4 [24-27, 46, 47]. Occasionally polymer based binders such as CMC were also involved to keep the connectivity [25].

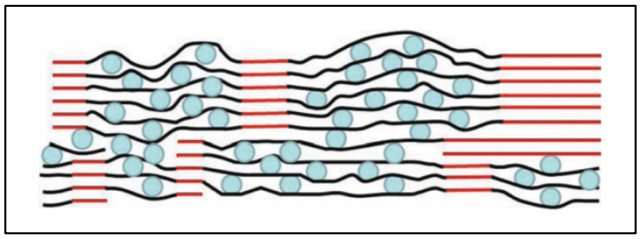

Figure 1.3 Cross-sectional schematic drawing of a high-capacity, stable electrode, made of a continuous, conducting 3D network of graphite (red) anchoring regions of graphene–Si composite. Blue circles: Si nanoparticles, black lines: graphene sheets.
Source: [45]

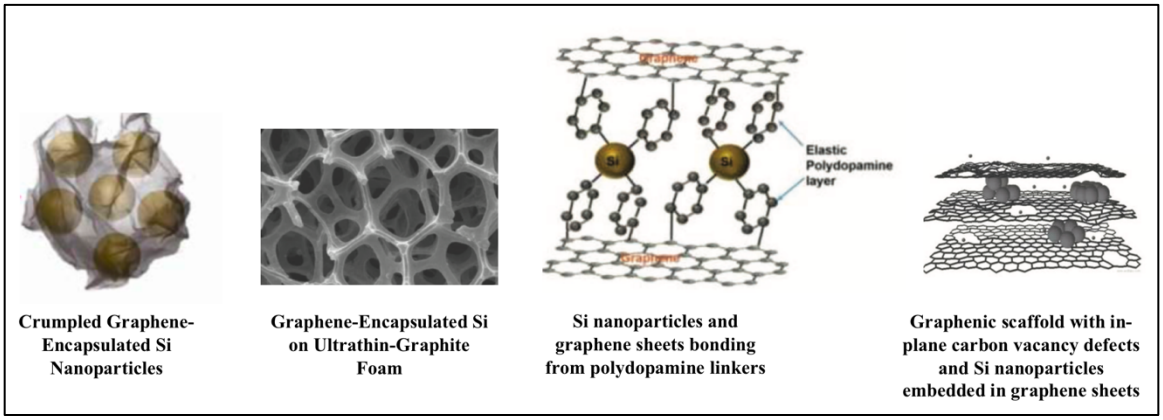

Figure 1.4 Schematics of a few Si/graphene-based anodes tested for electrochemical performance experimentally.
Source: [24-27, 46, 47]

Success of graphene additive in Si electrode further inspired emergence of graphene based advanced electrodes with high capacity alloying active electrodes such as tin (Sn) [30, 48-50], germanium (Ge) [51-53], sulfur (S) [54, 55], and selenium (Se) [55-57] to name a few, most of which can also be successfully employed in NIBs and KIBs. Naturally, it is the interface of 2D graphene and 3D electrode bulk materials in these systems that becomes the focal point and dictates their applicatory success. Experimental studies reveal Si/graphene composites to have superior electrochemical performance and mechanical stability, yet same effects have not been recognized in few of the above-mentioned electrodes. It is for this reason that these complex interfaces need to be characterized and studied in detail.

1.2.2 Heterostructure Electrodes Based on New 2D Materials

There has been an increasing interest towards alternative 2D materials in replacement of graphene chiefly because graphene is not easy to synthesize in large scale and the resultant cost is very high for an upscale commercial application. In this regard, transition metal disulfides (TMD) such as Molybdenum Disulfide (MoS_2) and MXenes are another class of 2D materials that are actively being explored for their applications as electrode materials in recent years. While individually both suffer from drawbacks such as conversion reactions and low capacity, which renders either of them as a poor electrode in itself, they have a huge scope which is still under-investigated when paired with high capacity electrodes material such as Si. A study by Zhang et al. 2018 used MoS_2 nanosheets to interconnect Si-C nanoshells and showed the reversible capacity of 1365.7 $mAhg^{-1}$ at 0.5 Ag^{-1} after 500 cycles, accompanied by a high initial coulombic efficiency of 81.5 % [58].

MoS_2 was considered because of its high reported specific capacity (669 $mAhg^{-1}$) and very high Li surface diffusivity [59]. The work also showed that even though in contact with Si-C, MoS_2 does undergo conversion reaction with Li to form Li_2S providing anode with extra Li adsorption sites. Another experimental investigation led by Kawade et al. synthesized silicon (Si)/molybdenum disulfide-graphene (MoS_2-G) nanocomposites with various Si/MoS_2 ratios as anode materials for LIB. Cyclic voltammetry study revealed that the intercalation of Li ion into the MoS_2 is followed by MoS_2 reduction to Mo embedded in Li_2S matrix. On extraction of Li ion from Li_nMoS_x lattice, there is the oxidation of Li_2S into S, an irreversible conversion which is not favorable for battery [60].

In contrast to MoS_2, there are a greater number of studies involving MXenes as a replacement of graphene due to their structural stability during cell cycling, high conductivity, high surface Li diffusion and flexibility. MXenes are a family of two-dimensional materials composed of early transition metal carbides discovered by Gogotsi and coworkers in 2011[61]. Among them, Ti_3C_2 is the most commonly studied one because of its easier synthesis and more porous structure [62]. One of the first reports of Si nanoparticles in Ti_3C_2 layers was by Kong et al. who simply sonicated Si with Ti_3C_2 to form a composite and tested it for its electrochemical performance. They reported a reversible capacity of 188 $mAh \cdot g^{-1}$ at 0.2 $A \cdot g^{-1}$ after 150 cycles with improved capacity retention as compared to pure Si [63]. More recently, Zhang et al. 2019 synthesized a similar structure of Si nanoparticles bounded by aqueous MXene Ti_3C_2 binder to form a composite anode material [64]. It is to be noted while both the studies primarily had similar target structure, their mode of synthesis were different. In the later study, role of Ti_3C_2 as a conductive binder and adhesive that improves mechanical stability were well established

experimentally. The study also reported much better electrochemical performance of the system. Figure 1.5 depicts schematic representations of Si/Ti_3C_2 composite structures directed by two synthesis techniques in the two mentioned studies which differed in their electrochemical output by order of 10s. It is indeed conclusive that slight difference in Si-Ti_3C_2 interaction led to this vast performance change, reasons for which are centered around the Si/ Ti_3C_2 interface investigation.

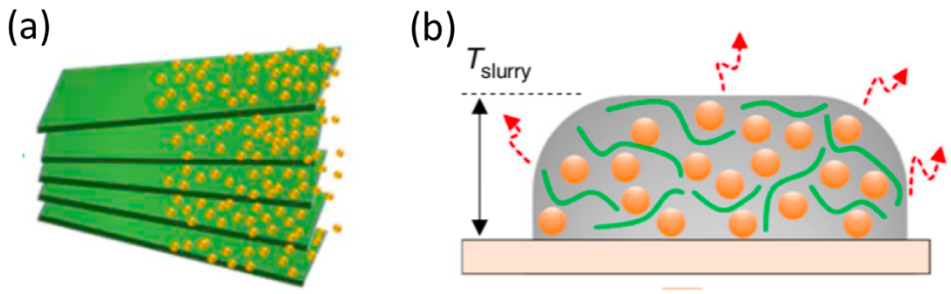

Figure 1.5 (a) Si nanoparticles mixed with MXenes multilayered structure by ultrasonication. (b) Si nanoparticles mixed with aqueous MXenes to form a slurry that is coated over a current collector.
Source: [63, 64]

1.3 Alternative Batteries

1.3.1 Sodium Ion Batteries

Sodium (Na) being the fourth most abundant element on earth, offers a potential rechargeable electrochemical energy storage (EES) in the form of sodium-ion battery (NIB) [15, 65-67]. Na metal is cheaper and has its redox potential closer to that of Li ($E^{o}_{(Na+/Na)}$ = -2.71V) [68]. All these advantages make NIB a real alternative to LIB. Although Na is heavier than Li, resulting in comparatively lower energy density than LIBs,

it is a small penalty to pay for safer, cheaper, abundant, and rechargeable energy storage system.

Concerning battery components and electrical storage mechanisms, NIB is very similar to LIB; the only exception lies in their ion carriers. Na, is in the same group as Li and possesses similar chemical behavior, shows identical diffusion kinetics and comparable diffusion barriers as that of its Li counterpart while combined with solid state host materials [69]. Similar charge/discharge profiles are reported for NIBs and LIBs except for some different plateau observed in NIB due to Na size induced strain effects [15]. Na being bigger in size offers sluggish transport, and therefore, it has been reported that NIB electrodes tend to exhibit diminished cycle stability.

Much advancement has already been made in studying cathode materials for NIB [70-72]. Analogous to LIB, mostly sodium layered oxide compounds, and polyanion compounds have been reported [73]. Most of these studies are based on improved designing of the host species to accommodate large Na ions so that minimal structural change takes place during the charge/discharge cycle. On the contrary to the positive electrode research, negative electrodes for NIB are less explored and still a conundrum. Initially, crystalline carbonaceous anode such as graphite was investigated as a potential electrode material for NIB owing to their success as the anode in LIB [74], but the degree of Na intercalation through graphite framework was found to be negligible due to its larger diameter [75-77]. To overcome this, Wen et al.[19] put forward expanded graphite with large interlayer spacing as an anode material for NIB that could ease Na^+ ion intercalation and provides the decent capacity of 150 $mAhg^{-1}$. However, such structures are synthesized via oxidation of graphene followed by partial reduction which results in the residual oxygen-

containing groups in the interlayers. These oxygen-containing groups hinder Na^+ ion intercalation and therefore affecting the overall efficiency of the electrode [78].

Henceforth, focus shifted towards the disordered carbonaceous materials such as hard carbon and metal oxides such as titanium-based oxides [79, 80]. These materials were found to exhibit better reversibility during electrochemical processes in NIBs and provide comparatively high specific capacities. Table 1.1 lists some of the anode materials with their specific capacities as reported in the respective literature. It has been studied that heteroatom doping in carbonaceous materials significantly improves its specific capacity by creating defect sites which eventually facilitates Na^+ absorption and charge transfer process [81]. Transition metal oxides (TMOs) and transition metal sulfides (TMSs) have also been reported as potential anodes for NIBs due to their high capacities [82]. However, their sodiation/desodiation mechanism is based on conversion reaction which leads to significant structural changes in the electrode and substantial volume expansions. Further, group 14 and 15 elements tend to form alloys with Na, which exhibit very high capacities (ranging from 350 – 850 $mAhg^{-1}$ in case of group 14 elements and 385 – 2560 $mAhg^{-1}$ in case of group 15 elements) [83]. Despite high capacities, their practical application is currently limited as they have lower cycle life and undergo high-volume expansion [76, 84]. These alloys with high storage capacity can be exploited further with improved structural design and additives to enhance the charge-discharge cycle life of NIBs and control the volume expansions. However, the existing studies lack the detailed understanding of the bulk electrodes and interfacial characteristics in composite electrode systems.

Table 1.1 Anodes for NIB with their Investigated Capacities

S. no.	Anode material	Capacity in mAh g^{-1}
1.	Hard Carbon	300[85]
2.	Expanded Graphite	150[78]
3.	Reduced Graphene oxide	141[86]
4.	N doped porous nanofibres	212[87]
5.	S doped Carbon	516[81]
6.	$TiNbO_2$	160[88]
7.	S-TiO_2	320[89]
8.	$Na_2Ti_3O_7$	89[90]
9.	$Na_2Ti_3O_{15}$	258[91]
10.	*a*-Si	725[92]
11.	*a*-Ge	369[93]
12.	Sn	847[94]

1.3.2 Potassium Ion Batteries

The motivations to study potassium ion batteries (KIBs) are as competitive as NIBs. Though, Na is cheaper and smaller in size than K, K has lower standard reduction potential, which is closer to Li (-3.04V $E^0 = Li^+/Li^-$ < -2.93V $E^0 = K^+/K^-$ < -2.71V $E^0 = Na^+/Na^-$) [19]. This permits KIBs to operate at higher potentials with better energy density than NIBs [95]. Moreover, the ionic mobility of K remains unhindered by its weight due to smaller stokes radius as shown in Figure 1.6 [96]. On the electrode front, K intercalated graphite is found stable even at a high alkali density of KC_8 [97]. The electrochemical analysis by Komaba et al. demonstrated graphite anode to have 244 $mAhg^{-1}$ reversible capacity for KIB in 0 - 0.3 V range [96]. Thus, commercially acceptable LIB anodes show good performance for KIBs at relatively safer voltages [95].

KIB research is still lacking in finding a reliable cathode material. Transition metal layered oxide cathodes exhibit fast capacity fading because it is not easy to extract or re-intercalate large K ions without any structural damage [98]. Layered birnessite $K_{0.3}MnO_2$ was one of the first layered oxide cathodes investigated for KIB by Vaalma et al.[99] in non-aqueous electrolyte, and it only showed a reversible capacity of 65 $mAhg^{-1}$ between 3.5 - 1.5V with only 57% capacity retention. Instead, metal organic frameworks (MOFs) are preferred alternatives to layered oxides as KIB cathodes. Pore sizes on MOF are adjustable and promising for reversible K storage. Eftekhari et al. introduced K containing MOF called Prussian Blue (PB) cathode $KFe_4^{III}[Fe^{II}(CN)_6]$, which could achieve 78.62 $mAhg^{-1}$ reversible capacity and only 12% capacity fade post 500 cycles [17]. This stability marked PB as a prospective cathode for KIB and encouraged experimental electrochemical studies on several PB analogs [100-103]. Despite these studies, cathodes for KIB still remained a major limiting factor in terms of specific capacity. The next options for high-capacity KIB cathodes were recognized among K-free materials such as organic perylene tetracarboxylic dianhydride (PTCDA) and poly (anthraquinonyl sulphide) that exhibited capacities as high as 131 $mAhg^{-1}$ and 190 $mAhg^{-1}$ due to larger interlayer spaces. Still, these advantages come at the price of poor conductivity in these organic electrode [104, 105]. Once again, high-capacity alloying electrodes (such as S and Se) mixed with conductive and supportive additive mesh are viable options to overcome existing challenges in KIB cathodes.

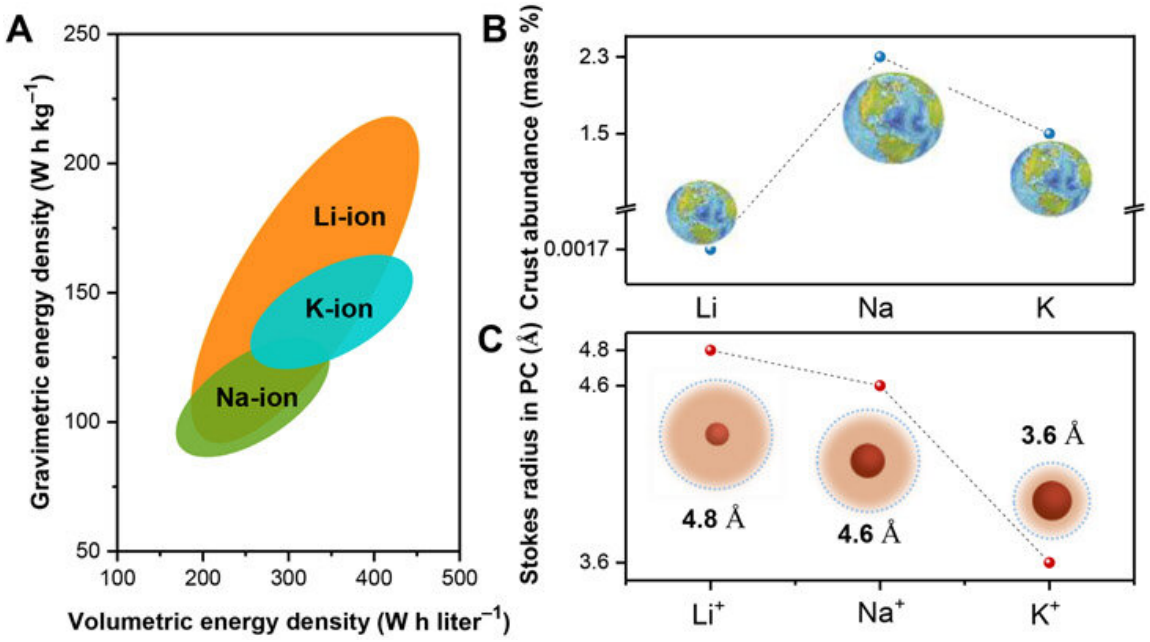

Figure 1.6 (A) Comparison of LIB, SIB, and PIB in terms of energy density. (B) Abundance of lithium, sodium, and potassium metal in Earth's crust (wt %). (C) Stokes radius of Li^+, Na^+, and K^+ in PC.
Source: [19]

1.4 Motivation

1.4.1 Introduction to First Principles Techniques

Material properties and behavior can be determined from modeling approaches derived from physics and chemistry. Each modeling approach is particularly best suited for a limited length and time scale as shown in Figure 1.7. Quantum mechanics based methods like ab-initio are best suited for nanoscale simulations where atom count is no greater than a few hundreds. For microscale modeling of large atomic systems (< million atoms), classical mechanics methods like molecular dynamics (MD) have been recognized to be best choice. At mesoscale, coarse-grained models are adopted to model conformational space of large systems. Monte Carlo (MC) methods further average and homogenize micro

and mesoscale simulations to extended time scales. All these models are uniquely capable in predicting material properties based on structure-property relationships. Continuum mechanics models are used to model materials at macroscopic scale but their limitation in providing nanoscale phenomenological insight cannot be denied [106-108].

Recent years have seen emergence of Machine Learning (ML) approaches that rely on mathematical functions rather than physics or chemistries to predict material properties [109-111]. Their only dependence is on large amount of data associated with targeted property or material. This makes ML approaches applicable to almost all scales conditioning on availability of large amount of uniform data to learn from.

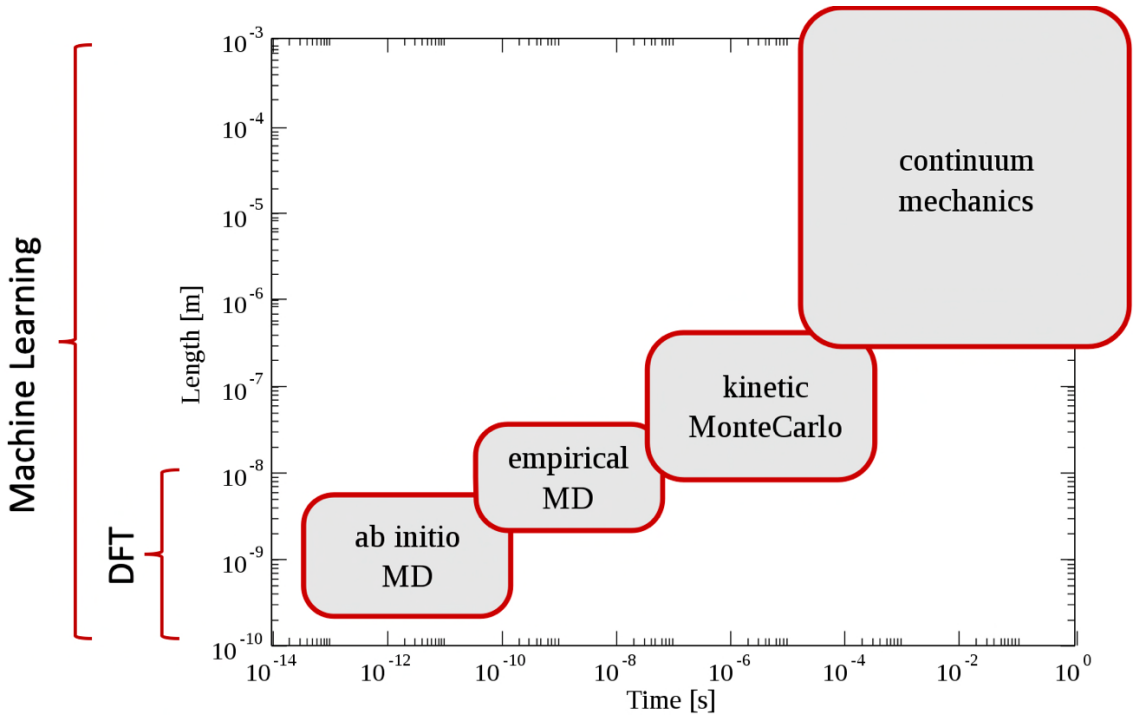

Figure 1.7 Length and time scales for simulation models for materials.

Ab-initio Methods and Density Functional Theory. At the bottom of every science, there lies simple interaction between atoms as all grounds of stability are based on principles of thermodynamics. These properties associated with microscopic processes cannot be obtained from experimentation but atomic simulations. Atomic simulation, also called first principles techniques use laws of quantum mechanics rather than classical physics as the basis of their calculations. Prominently called ab-initio methods, they solve Schrödinger equation (equation 1.1) for every atom in the atomic configuration and as such are free from the errors posed by fitting parameters [112].

$$H\psi = E\psi \tag{1.1}$$

Major shortcoming of Schrödinger equation is the difficulty it poses in solving for many body problem. For systems larger than tens of atoms, it is impractical and computationally expensive to solve [113]. Approximations such as Born-Oppenheimer which considers nuclei a single stationary body that interacts with electrons, targets to simplify the complex problem [114]. Another prominent example is of Hartree Fock method [115] which further attempts to simplify many body Hamiltonian wavefunction in the form of standard base functions for antisymmetric electron wavefunction determined by Slater determinant. Dependent upon wave function for every electron, Hartree Fock method fails to consider electron correlations.

Density Functional Theory (DFT) is an appealing alternative approach where the complexities of Hartree Fock are reduced by reformulation of energies as a functional of ground state electron densities $\boldsymbol{n_0}$ in the system. This reduces the cost of computation and

makes atomic simulations inclusive of electron correlations [116]. The ground state wave function $\boldsymbol{\psi_0}$ becomes a function of $\boldsymbol{n_0}$:

$$\psi_0 = \psi\,[n_0] \tag{1.2}$$

The ground state energy $\mathbf{E_0}$ is the functional of $\boldsymbol{n_0}$:

$$E_0 = E\,[n_0] = \langle \psi\,[n_0]|\, \hat{\mathbf{T}} + \hat{\mathbf{V}} + \hat{\mathbf{U}}\, |\psi\,[n_0]\rangle \tag{1.3}$$

where $\hat{\mathbf{T}}$ is the kinetic energy, $\hat{\mathbf{V}}$ is the potential energy and $\hat{\mathbf{U}}$ is the internal energy due to electron-electron interaction. $\hat{\mathbf{V}}$ of a system can be written in terms of its density $\boldsymbol{n}$ and is therefore minimized to obtain ground state energy of the system.

$$V\,[n] = \int V(r) n(\mathrm{r})\, \mathrm{d}^3\mathrm{r} \tag{1.4}$$

DFT methods are effective in analysis of thermodynamics properties of battery materials such as Gibbs free energy calculations which can provide a theoretical estimate of chemical potentials of battery electrodes and chemical driving forces [117]. Besides, distinctive chemical, electronic and mechanical insights regarding new electrodes can be obtained in a short time by DFT simulations of solid state periodic units of electrode materials. As Li content variations in electrodes is accompanied by structural, mechanical, phase and volume evolution, ab-initio based simulations can give insight into volume and density changes in electrodes [118]. Dependence of first principles techniques on quantum

mechanics makes them theoretically accurate and free from errors associated with empirical potentials. Therefore, they are preferred means to study physicochemical properties of battery electrodes that are closely dependent upon energetics of the system.

Approximations to Density Functional Theory. Equations (1.3) and (1.4) are used to calculate energy of the system **E** with electronic density ***n***. However, primary theory of DFT neglects to define energy contribution by 'correlation', i.e., energy due to interaction between electrons. To correct this, an additional correlation function $\mathbf{E_{xc}}$ is added to the Hamiltonian [113]. One of the prominent and simplest functional to define $\mathbf{E_{xc}}$ is local density approximation (LDA) which is based on exchange and correlation energy per atom $\mathbf{e_{xc}}(\boldsymbol{n}(\mathbf{r}))$ as

$$E_{XC}^{LDA}\,[n(\mathrm{r})] = \int e_{XC}(n(\mathrm{r}))\; n(\mathrm{r})\; \mathrm{d}^3\mathrm{r} \tag{1.5}$$

LDA is favorable for homogeneous systems but fails to predict for materials where charge densities fluctuate noticeably. To improve this, gradient corrections are applied to LDA which make $\boldsymbol{E_{XC}^{LDA}}\ \mathbf{[}\boldsymbol{n}\mathbf{(r)]}$ function of electron density and gradient. These are called generalized gradient approximations (GGA) [119] where $\mathbf{E_{xc}}$ is defined by

$$E_{XC}^{GGA}\,[n(\mathrm{r})] = \int e_{XC}^{LDA}\left(n(\mathrm{r})\right)\; F_{XC}\;(n(\mathrm{r}),\, \nabla n(\mathrm{r}))\; \mathrm{d}^3\mathrm{r} \tag{1.6}$$

GGA greatly improves the energy predictions for non-homogeneous systems or heavy atoms. It is important to note that GGA does not have a single formulation and has several versions which will be discussed and used in this dissertation.

1.4.2 Computational Modeling of Battery Interfaces

Batteries have prominently three interfaces, namely: Current collector and electrode, electrode and additive, electrode and electrolyte. Battery performance is sensitive to all the three interfaces and therefore needs special analysis in battery design. A thorough characterization of these complex nanoscale interfaces is yet a challenge experimentally. Techniques like scanning tunneling microscopy (STM) and atomic force microscopy (AFM) have enabled studying interfaces between ordered 2D material heterostructures [120], yet their scope is not expandable to complex 2D-3D interfaces. Computational modeling methods such as density functional theory (DFT) and molecular dynamics (MD) simulations are good alternatives to develop a deeper understanding of these interfacial characteristics.

Current Collector and Electrode Interface. Cu at anode end and Al at cathode end are the conventional choices for current collectors based on preferred operational voltages in LIBs. Interface between electrode and current collector has been recognized as the primary determinant of mechanical longevity of a battery. Efficient interfacial architecture needs to be designed, which can provide electrode a window to accommodate larger strains following repeated Li insertion/extraction. Maranchi et al. [38] studied efficiency of a-Si thin film electrode over Cu substrate and showed that Cu-Si delaminated over time, leading

to eventual failures. Cause of this delamination was recognized to be weak interface adhesion strength. Stournara et al. in their computational study of Si/Cu interface with ab-initio methods demonstrate that interface adhesion decreases upon Li insertion into the Si electrode [121]. They used measure of work of separation (Wsep) based on Density Functional Theory (DFT) to calculate the interface adhesion between Cu and Si electrode with varying Li concentration. Their calculated interface adhesion between amorphous Si and Cu was 1.85 J/m^2 which reduced by 16% to 1.55 J/m^2 in completely lithiated state. The value of Wsep was further correlated with Young's modulus E to determine critical stress of mode I fracture along the interface. This study showed that increase in Li concentration weakens the interface, imparts ductility to the structure with increased plastic deformations and fracture toughness which can collectively cause delamination of Si from Cu substrate.

Ideally, high adhesion between active electrode material and current collector is identified as beneficiary for battery cyclability [122-124]. Contrary to popular belief regarding essential high interface strength between current collector and electrode, Basu et al.[32] recognized benefits of slippery graphene surface at current collector end in combating stresses in Si anode upon lithiation, thereby increasing the cycle life of the electrode (demonstrated in Figure 1.8 using MD snapshots). Similar to earlier works, they also measured Wsep to calculate interface strength between Si electrodes with substrates like Ni, Cu, Si, and Graphene. Among the four studied interfaces, Si/graphene interface had the lowest interface strength of 0.41 J/m^2 while Si/Ni and Si/Cu had highest interface strengths of 1.6 J/m^2 and 1.5 J/m^2, respectively. Despite the low interface strength condition, graphene interface enhanced the electrochemical performance of Si anode and

stabilized it for up to 150 cycles with 800mAh g^{-1} capacity, which was far greater than Ni interface. Latter could only retain the capacity of 190 mAh g^{-1}.

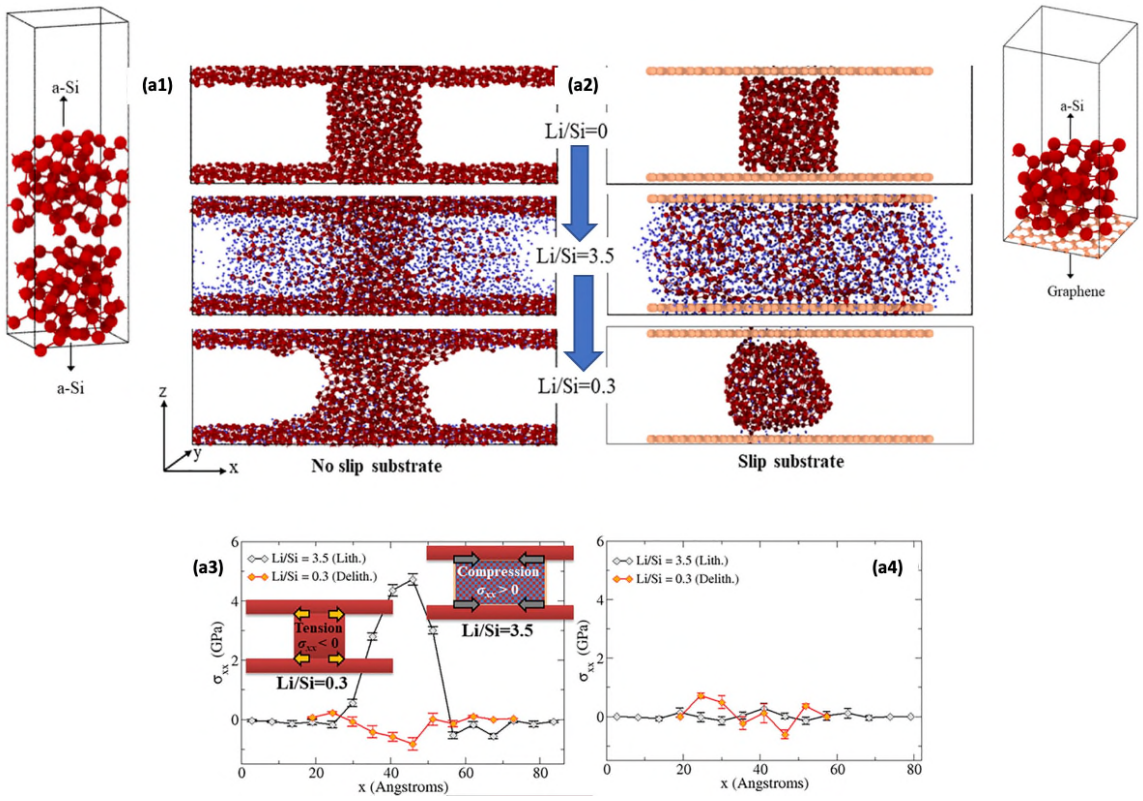

Figure 1.8 Si simulation systems with a rigid nonslip substrate (a1) and a rigid slip substrate (a2) during a lithiation and delithiation cycle. The snapshots indicate highly lithiated stage (Li/Si = 3.5) and a highly delithiated stage (Li/Si = 0.3), from top to bottom. The red atoms are silicon, while the blue atoms are lithium. (a3) and (a4) show the normal stress σ_{XX} profile at Li/Si = 3.5 (black lines) and Li/Si = 0.3 (orange lines) for the systems with nonslip and slip substrate, respectively.
Source: [125]

Electrode and Additive Interface. Continued electrical contact between active electrode and additive is as crucial as it is between electrode and current collector. Therefore, measure of interface adhesion between active electrode and additive needs to be properly determined before experimental procedures. Yet, very few studies emphasize on this.

Interface adhesion between amorphous Si and microporous C determined by Wsep calculations is very high 3.13 J/m^2 when compared to the graphene interface, mostly due to covalent bonding between Si and C, which is missing in interface provided by pristine graphene [126]. It has been realized that Li insertion mostly reduces the interface strength between electrode and substrate. The interface strength value reduced to 2.44 J/m^2 in $Li_{3.75}Si/Li_{0.75}C$ from 3.13 J/m^2 of Si/C, as shown in Figure 1.9 [126].

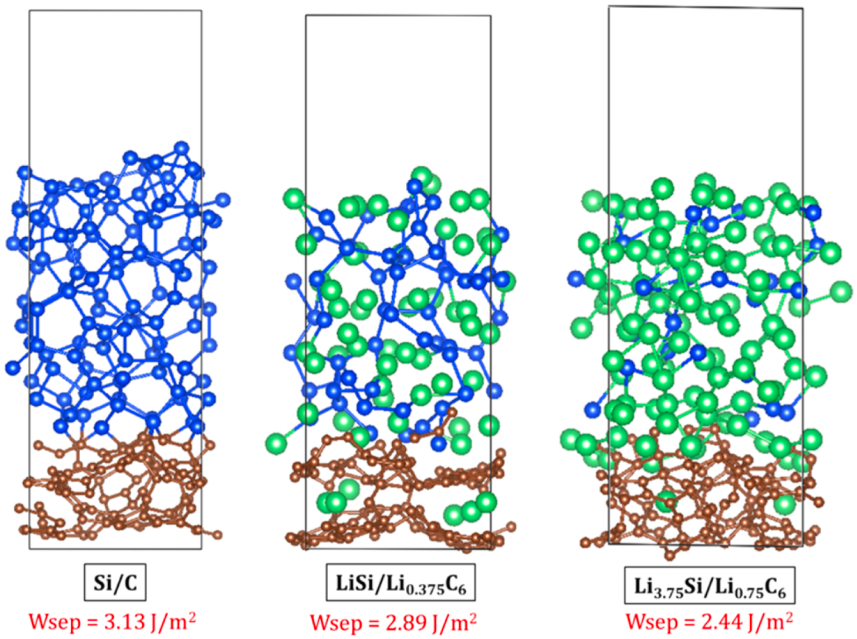

Figure 1.9 Si/C interface weakening upon lithiation demonstrated by work of separation calculations.
Source: [126]

Electrode and Electrolyte Interfaces. Electrode- electrolyte interface has been primary safety hazard in commercial LIBs [127]. Thermal runaways caused by damage to insulating separator, Li dendrites, deflection of the electrodes etc. are the onset of mechanical abuse of the electrodes [128]. As a result, several strategies to restrict Li dendrite formation and

damage to solid electrolyte interface(SEI) have been studied experimentally as well as computationally. In this regard, monolayer graphene coating over Si anode is again recognized as a good means to stabilize SEI layer over repeatedly expanding-contracting Si electrode in electrochemical studies supported by MD simulations [129]. However, more interesting and less structurally complex approach is to alter the separator itself. Additives to electrode add weight of inactive electrode material and lower the capacity of the system. Instead, a safe coating over a separator that permits selective Li diffusion appears to be a better alternative. Foroozan et al. utilized DFT-based ab initio molecular dynamics simulations (AIMD) to show atomic interactions between diffusing Li ions and defected graphene oxide (GO) coated over a surface of glass fiber separator [130]. Adsorption energy calculations via DFT detail how Li ions first get adsorbed on GO layer, which delays its migration to the Li metal anode surface, preventing formation of dendrites in the process. Process of Li diffusion through defected GO sites has been further simulated with AIMD simulations demonstrating initiation of C-C bond breaking due to Li diffusion, which generates more diffusion sites. Climbing image nudged elastic band (CI-NEB) method to calculate activation energy barrier for the diffusion of Li across the separator showed that Li atoms diffuse through the defected sites on GO by knocking off Li atoms adsorbed on the GO layer. The energy barrier is reduced to 0.38 eV when diffusing Li ion is knocked off by Li atom entering a defective site. Thus, a large flux of Li ions on anode is moderated by a GO coated separator. This study uniquely regulates the Li transport and delays the tip-effect in Li dendrite formation.

Future Direction of Interface Modeling. All these computational studies emphasize the important contributions that can be provided about battery design and stability with first principle simulations. Recent years have seen emergence of Machine Learning (ML) based models that have proven to be effective means to discover new battery materials [131-138]. Yet, they have not been sufficiently utilized to study interface systems. Unique complexities of the interface pose a challenge in complete chemical representation and prediction of interfacial systems. Most importantly, there is a lack of data on interface structures in databases which makes ML training dependent on ab-initio and MD simulations. An exemplar ab-initio ML-based framework have been reported by Chandran et al. [139], which utilizes DFT to generate training data of interfaces and independent materials followed by training regression ML models that predict the energies and stable configurations of Ni| Ni alloys interface systems.

1.5 Goal and Organization of the Dissertation

Section 1.2 throws light on the electrochemical potential of heterostructure electrodes consisting of 2D additives and the bulk alloying materials that can address the major challenges in the further development of LIBs and metal ion batteries. Sub section 1.4.2 summarizes important attempts made in evaluating the interfaces in batteries with computational simulations. The exemplar works show how knowledge of interfacial chemo-mechanical characteristics such as interface adhesion strength, bonding, and diffusion kinetics can contribute towards electrode design. It is needless to say that the impact of interface characterization is extendable to heterostructure applications beyond batteries. The goal of this dissertation is to investigate interfacial chemo-mechanical

characteristics of 2D-3D heterostructures that contribute towards their good electrochemical performance and stability by the means of first principles techniques. Important questions that are addressed are: What are the characteristics of promising 2D-3D interface? How does the presence of 2D additive affect the electrochemical performance of the electrode? How do engineered surfaces impact the interface adhesion? What are the challenges associated with modeling these interfaces, and how can they be addressed with Artificial Intelligence (AI)?

In Chapter 2, we present the investigation of high-capacity amorphous Germanium (Ge) anode for NIB by first principles techniques such as DFT and AIMD. Our results highlight the voltage correlation with intermediate sodiation structures and diffusion kinetics that is comparable to LIBs, thus emphasizing on promising NIB alternative to LIB. Chapter 3 focuses on modeling graphene-based interfaces with Selenium (Se) and presents a parallel comparison with Si/graphene interface as its efficacy is well utilized in the batteries [23-27]. We systematically study the variation in interface strength with DFT between Se and graphene as Se undergoes phase transformation from crystalline to amorphous. Longevity of interface or lack of thereof is recognized from physicochemical characterization, which also demonstrates low electronic efficacies between Se and graphene surfaces in comparison to Si and graphene. In Chapter 4, we further explore the performance of Se-graphene composite cathode for KIBs where a reliable cathode material has not been recognized yet. State of charge of cathode is correlated to the graphene-influenced microstructural order in the electrode. In Chapter 5, we investigate the interface strength of Si with a new class of 2D materials such as surface-engineered MXenes. We

report variation in the interface strength between Si and MXenes as surface functional groups (OH, F and O) are altered.

Modeling these interfaces using DFT is computationally exhaustive. Thus, in Chapter 6, we develop machine learning (ML) based potential energy surface (PES) for a complex polymorphing tin (Sn) and graphene interface that can be used to predict energies of new Sn/graphene interfaces. We discuss a new approach to model multiphasic systems with AI and show performance of modified high dimensional neural networks trained on DFT data.

CHAPTER 2

GERMANIUM ANODE FOR SODIUM ION BATTERY

2.1 Introduction

We discuss in Sub section 1.3.1 the significant challenge associated especially with NIB anodes. Si has been one of the most extensively studied anode materials for NIB due to its enormous success in case of LIB. All forms of Si have been probed for their potential as anode in NIBs. Initially, crystalline Si (*c*-Si) was investigated for Na diffusion kinetics. It was reported that despite being chemically similar to Li, Na intercalation in *c*-Si is limited because of its bigger size. Bulk Si has been computationally investigated to have a very high energy barrier (1.41 eV) for Na diffusion [140]. Kulish et al. [141] investigated layered Si such as polysilane as an anode for NIB. They showed using the DFT and Nudged Elastic Band (NEB) method that energy barrier for Na diffusion in such compounds gets reduced to 0.41 eV. Still, these materials exhibit a low capacity of 279 $mAhg^{-1}$ [141]. Failure of layered Si motivated the intense investigations of amorphous Si (*a*-Si), where again Na displayed very low diffusivity that makes it an impractical choice [92].

These trials with Si leaves researchers with the most viable option of considering Ge, as the potential host material for Na^+ ions due to its vast similarities with the Li-Si system. Like Si, Ge too takes up one Na per atom to form Na-Ge alloy [83]. Theoretical capacity for the Na-Ge system has been reported to be 369 $mAhg^{-1}$, which may be lower than other alloys but is still better than C-based and TMOs/TMSs anodes [93]. Furthermore, Na-Ge anode is known to undergo comparatively lower volume expansion than other available alloying alternatives discussed in Sub section 1.3.1. This makes Ge a

promising anode material for NIB. However, unlike Si, Ge is not well studied and requires thorough investigations from both the experimental and theoretical points of view to gain more insights. In this chapter, first principle techniques are employed to analyze Na storage and diffusion kinetics in promising Ge anode. This work was published in the *Journal of Material Science* in 2018 titled as '*Amorphous Germanium as a Promising Anode Material for Sodium Ion Batteries: A First Principle Study'*. Simulation results draw a picture of Na-Ge intermixing at atomistic level and helps to trace Na trajectory through *a*-Ge. Present study manifests higher diffusivity of Na in *a*-Ge as compared to other known anode materials. Moreover, a thorough analysis of Pair Correlation Function (PCF) reveals the microstructural changes at different stages of sodiation into germanium.

2.2 Computational Details

The first principle calculations were done using Vienna Ab Initio Simulation Package (VASP) [142]. The optimized equilibrium structures were obtained via DFT as implemented in VASP. PAW pseudopotentials [143] were taken for the inert core electrons, and valence electrons were represented by plane-wave basis set. The GGA, with the PBE (Perdew-Burke-Ernzerhof) exchange-correlation functionals were taken into account [144]. All DFT relaxation includes force, geometric, volume, and cell shape relaxations until the minimum energy criteria of 1.0×10^{-4} eV was met. All the internal coordinates are relaxed until the Hellmann-Feynman forces are less than 0.02 eV/Å. Plane wave cutoff for all the calculations was taken as 230 eV following high precision convergence as described in VASP and was tested accordingly. The Brillouin zone was sampled with $1\times 2 \times 1$ mesh in Monkhorst pack grid.

In order to model amorphous (*a*-)Ge_{64}, we started from crystalline (*c*-)Ge_{64} and generated *a*-Ge_{64} via computational quenching process detailed in Appendix A. Amorphous Na-Ge alloy is considered in 1:1 ratio ($Na_{64}Ge_{64}$ system) to calculate intercalation potential vs. capacity followed by the consecutive desodiation leading towards the Ge_{64} system. The ratio taken gave specific capacity (369 $mAhg^{-1}$) for *a*-Ge anode closer to experimentally and theoretically investigated capacities [93, 145]. Consideration of *a*-Ge_{64} as the precursor in this mixing process facilitates the Na penetration through the amorphous network. $Na_{64}Ge_{64}$ mixed system was generated via incorporation of 64 Na atoms into *a*-Ge_{64} using AIMD simulation. RDF was used to determine the phase of the final alloy mixture. Figure 2.1 depicts an overall picture of the entire process.

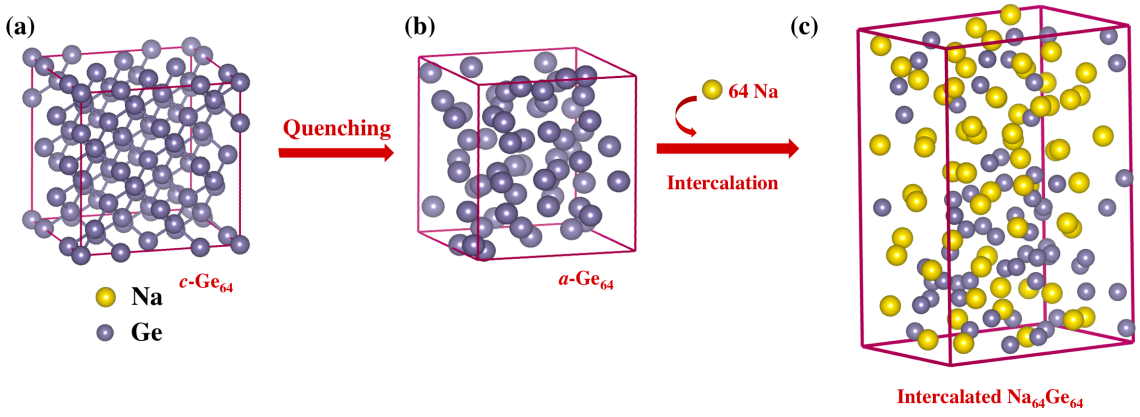

Figure 2.1 (a) Optimized structure of the initial crystalline Ge_{64} (*c*-Ge_{64}) (b) Optimized amorphous Ge_{64} (a-Ge_{64}) system obtained via quenching process of *c*-Ge_{64} (c) Optimized structure of $Na_{64}Ge_{64}$ obtained by intercalating Na_{64} into *a*-Ge_{64} via AIMD simulation.

To compute the intercalation voltage profile (V vs. Na/Na+) for Na-Ge binary anode system, several intermediate structures with Na concentrations varying by 6.25%

were taken into account and optimized by DFT. In a system Na_nGe_{64}, n is the number of Na atoms inserted in the computational cell and varies from 0 to 64. Specific capacity for Na-Ge system was calculated using the formula

$$C = \frac{nF}{3.6 \times M} \tag{2.1}$$

where **C** is the specific capacity ($mAhg^{-1}$), ***n*** is the number of charge carriers (Na in this case), **F** is Faraday's constant, and **M** is molecular weight of the active material used (a-Ge_{64}). The energy minimization calculations provide information about the formation energy of the system ($\mathbf{\Delta E}_f$) and subsequently sodiation potential **V(*n*)** which is given by

$$V = \frac{\Delta G_f}{z_e F} \tag{2.2}$$

where, $\mathbf{z_e}$ is the charge carried by Na in the electrolyte, and $\mathbf{\Delta G}_f$ is the change in Gibbs free energy given by

$$\Delta G_f = \Delta E_f + P\Delta V_f - T\Delta S_f \tag{2.3}$$

The pressure and entropy components in the above equation can be neglected as they are of very small order as compared to $\mathbf{\Delta E}_f$. This makes free energy equivalent to formation energy defined by

$$\Delta E_f = E_{Na_nGe_{64}} - (nE_{Na} + E_{Ge}) \quad (2.4)$$

where $\mathbf{\Delta E}_f$ are the formation energies of the systems with varying Na concentrations, $\mathbf{E}_{Na_nGe_{64}}$ is the energy of systems with varying Na concentrations, $\mathbf{E}_{Ge}$ and $\mathbf{E}_{Na}$ are respective energies of anode system without Na and energy of single Na atom which in our case was calculated to be -1.307 eV.

In order to account for the intermediate phase changes in Na-Ge system, Pair Correlation Function (PCF), ***g(r)*** were calculated for different AIMD trajectories of different Na concentrations in *a*-Ge_{64}. These AIMD run were carried out for different Na_nGe_{64} species for 5000 MD steps with the time interval of 3 femtosecond (fs). PCF throws light on inter-atomic distances between the atoms throughout the process. Such an analysis helps in determining amorphous or crystalline nature of the system. PCF, ***g(r)*** for homo-atomic pairs in our system (Ge-Ge and Na-Na) were calculated and plotted. Here, the ***g(r)*** is the second order correlation function $g^2(r_{12})$, where $\boldsymbol{r_{12}\,(=r_2-r_1)}$ represents the distance between two atoms. The mathematical formula for PCF is given below, where (***Z-1***) represents the number of nearest pairs and ρ is the probability density.

$$\int_{r=0}^{\infty} \rho\, g(r).4\pi r^2\, dr = Z - 1 \quad (2.5)$$

Next, we investigated diffusivity of single Na in equilibrated *a*-Ge_{64}. Diffusion of single Na through *a*-Ge_{64} was determined by stimulating intercalation of Na atom at three elevated temperature conditions (1100 K, 950 K, 800 K) using AIMD for 15000 MD steps

with the timestep of 1fs. These AIMD trajectories were then used to compute mean squared displacement (**MSD**) for the determination of diffusion trajectory and diffusivity of Na atom in the Ge_{64} system. The MSD was computed by

$$\text{MSD} = \frac{1}{N}\sum_{n=1}^{N}(x(t) - x_n(0))^2 \tag{2.6}$$

where ***N*** is the number of particles to be averaged and ***x*** represents positions of the particle at different time frames. Further, Einstein equation **MSD = 6Dt** was taken into consideration to compute diffusivity of Na in Ge at various temperatures, where **D** is the diffusivity to be calculated and **t** is the time taken. In general, these AIMD simulations are done at high temperatures to reduce the simulation time by accelerating the rate of reaction. Diffusivities calculated at elevated temperatures were then extrapolated to room temperature (~300K) using Arrhenius equation:

$$\text{D} = \text{D}_0 \; e^{\frac{-E_b}{kT}} \tag{2.7}$$

Where, $\mathbf{D_0}$ is pre-exponential factor, $\mathbf{E_b}$ symbolizes the energy barrier, and **k** and **T** represent the Boltzmann constant and simulation temperature respectively [146].

2.3 Results and Discussion

2.3.1 Intercalation Voltage and Volume Changes

Using DFT, the equilibrium curve between charge and discharge curve can be obtained. Tracing such equilibrium Voltage vs. Capacity curve is the essential part of an electrochemical process. It gives the idea about battery performance and provides insight into significant structural or phase change phenomenon happening during the process. In order to compute intercalation potential, we started from the $Na_{64}Ge_{64}$ system and obtained the intermediate Na_nGe_{64} structures by removing 4 Na atoms (~6.25%) at a time, where n varies from 0 to 64. After modeling the initial structures for all of the Na_nGe_{64} phases, they were fully relaxed until the energy minimized structures were obtained. The potential value of each of these corresponding structures was computed by implementing the Equation (2.2). Figure 2.2(a) depicts the potential curve obtained for intermediate Na_nGe_{64} phases for the Na-Ge system. It is seen that voltage profile ranges from 2.08 V to 0.48 V. As Na concentration increases, there is a gradual potential drop until n = 16 (92 $mAhg^{-1}$ capacity) which then reduces upon further Na incorporation. There is a rise in voltage vs. capacity curve at around 100 $mAhg^{-1}$ (when n = 20). Such a 'voltage spike' is seen when there is a small energy difference in total energy of similar neighboring phases. When Na concentration reaches up to 50% (n = 32, 150 $mAhg^{-1}$ capacity), potential drop seems to become insignificant, and a plateau-like curve is noticeable henceforth. Such a plateau also indicates the existence of single-phase system inside the battery during the electrochemical process. This stability of single phase (for Na > 50%), i.e., the plateau-like curve, is in contrast with initial voltage jumps and spikes in the curve, where Na concentration (n =

20) is less. Therefore, we can say that structural phase instability is observed at low Na concentrations.

In general, the addition of Na atoms should lead to volume expansion due to large atomic radii of Na atoms. A single Na atom occupies around 31.9Å^3 volume in *a*-Ge_{64} and increases the volume of *a*-Ge_{64} by 2.23% However, during the DFT relaxation at different Na concentrations, a little different trend was observed regarding the volume change. It is essential to note here that upon addition of a small percentage of Na, there was initially a reduction in cell volume up to 19% of Na content (n = 12), which increased later on. This initial volume reduction and instability of equilibrium voltage vs. capacity curve for n < 20, strongly imply that chemical interactions are going on upon insertion of a small number of Na atoms in the *a*-Ge_{64} cell. Addition of Na atoms causes rapid bond formation among neighboring atoms which is the probable reason behind the volume contractions. On the other hand, with the increasing concentration of Na (n>16), the compressive stresses in battery anode also increase. As a result, the system acquires amorphousness by breaking these bonds to relieve these stresses. There is a subsequent Brownian motion in the system causing mixing of Na atoms, and hence there is overall volume expansion noted for the system. This hypothesis is supported by Na-Ge interatomic distances measured for various Na concentrations. There were significant variations seen for short-range atomic distances for small Na concentrations. The nearest average neighboring distance for 6% Na content (n= 4) was 3.327 Å, while for 19% Na content, it was 3.193 Å. Beyond 19%, there is a steady increment in the average Na-Ge neighboring distances upon further Na addition. Finally, in a fully sodiated state ($Na_{64}Ge_{64}$), cell volume expanded by 149.51%, which is less than the other alloying compounds studied as a potential electrode material [92, 147].

Figure 2.2(b) illustrates DFT derived equilibrium curve overlaid on the experimental charge/discharge curve for the first cycle in *a*-Ge taken from the Galvanostatic Intermittent Titration Technique (GITT) investigation by Baggetto et al. [145]. This GITT investigation is the constant current and quasi-equilibrium measurements. DFT, as implemented in VASP, deals with equilibrium thermodynamics, and thus DFT-derived curve represents the equilibrium configurations between the experimental charge and discharge profile. As per the expectation, our theoretical curve falls in the middle potential values, i.e., close to the mean voltages from experimental charge/discharge. This curve provides a good match with the reported GITT measurements. In experimental discharge curve, there is a sudden potential drop until 0.9 V, which is close to our calculated curve. [145] Eventually, the possibility of phase instability during lower Na concentration as seen in our equilibrium curve.

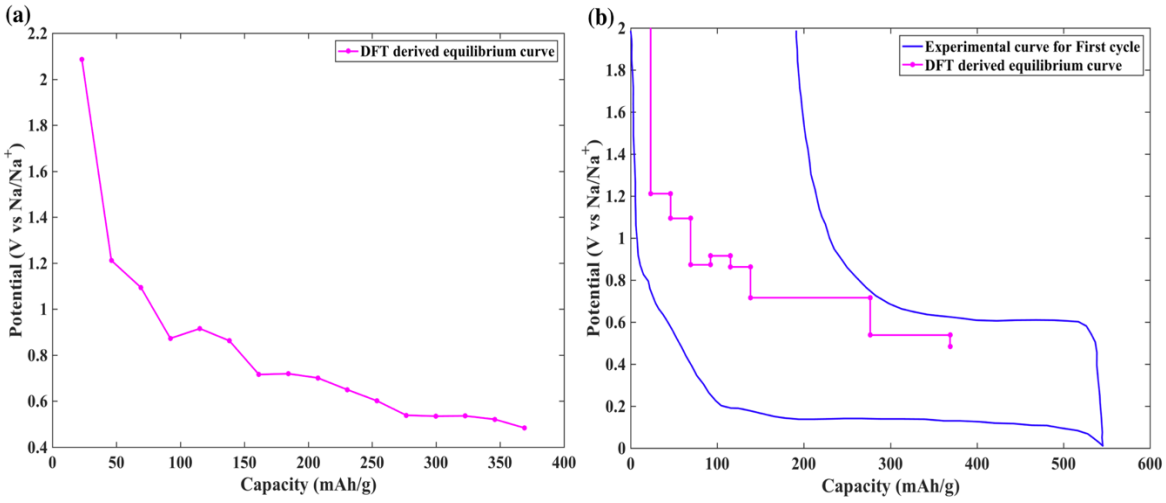

Figure 2.2 (*a*) DFT calculated Voltage vs. Capacity curve for Sodium Intercalation in *a*-Ge and (b) DFT derived equilibrium curve for intermediate stages of intercalated Na overlaid on experimental curve for Sodiation and Desodiation for first cycle in *a*-Ge.

2.3.2 Structural Analysis with PCF

The evolution of phase and structural changes of the electrode during intermediate stages were analyzed by evaluating PCF, *g(r)* of atomic pairs (Ge-Ge and Na-Na) in the system with varying Na concentrations. AIMD simulations were performed for Na-Ge systems with intermediate Na concentrations (6%, 19%, 31%, 50%, 69% and 88%). These concentrations were randomly chosen to get an idea of phase evolution throughout the sodiation cycle. *g(r)* was calculated using previously described Equation (2.5) and plotted against neighboring distance *(r)*. Figure 2.3(a) illustrates Ge-Ge PCF at 1000 MD time step for different Na concentrations. A single prominent peak at 2.8 Å was observed for all of the frames, which is close to the expected Ge-Ge first neighboring distance in the amorphous state (2.55 Å) [148]. No other significant peak was detected beyond the range of first neighboring distances. The absence of other peaks clearly signifies the amorphous nature of the Ge-Ge pairs. Highest *g(r)* value was obtained for the frame with 50% Na concentration. It is quite visible from Figure 2.3(a) that Ge displays amorphous nature throughout intermediate Na-Ge phases. This result is similar to previously reported analysis [149]. Still, so far, not much attention has been given to the effect of Na-Na pairs on structural changes in Ge anode upon sodiation.

This inspired us to perform the PCF analysis of Na-Na pairs to account for their phase change activity during initial sodiation. Therefore, we calculated *g(r)* for Na-Na at 1000 MD time step for Na concentrations varying from 6% to 88 %. 6% Na showed a high peak at 5.6 Å. The nearest neighboring distance between Na atoms in *c*-Na is 3.7 Å which matched with the molecular structure with 19% Na concentration. With increasing Na concentration, nearest neighboring distance decreases, indicating mixing of the system.

Significant loss of peak intensity was also detected with increasing Na concentration indicating loss of crystallinity and complete amorphization. At 88% Na concentration, no prominent peak was observed, and it became almost constant, suggesting total amorphous phase. These results imply that single phase detected (plateau-like curve in Figure 2.2(a)) for higher Na concentration (beyond 50%) is representative of the amorphous phase. On the other hand, in case of lower Na concentrations, brief crystalline phases and volume contraction were detected due to their inter-atomic interactions. In case of NIB, such phase transitions are common and are typically induced by biphasic reactions. Previous literature reported the similar biphasic nature for several other alloying anode materials [83, 84], and one of the most well-studied examples is the Na-Sn system [150].

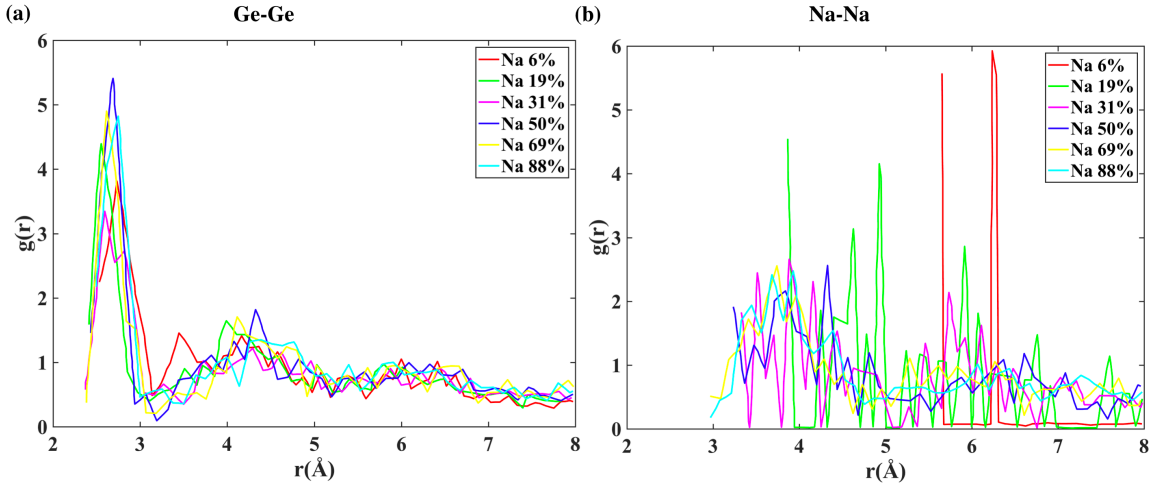

Figure 2.3 (a) Ge-Ge PCF at 1000 MD step for sodium concentrations varying from 6% to 88%. (b) Na-Na PCF at 1000 MD step for sodium concentrations varying from 6% to 88 %.

2.3.3 Diffusivity of Na in Amorphous Ge

Another critical feature that is important for battery performance is fast diffusion kinetics of Na in anode material. Diffusivity determines the ability of Na to mix with the anode material and charge/discharge rates of the battery. Diffusivity of Na in Ge was determined by calculating average MSD (Equation (2.6)) of single Na in bulk *a*-Ge_{64} as a function of MD time step at different temperatures. Here, the simulation temperatures are below the melting point of Ge (1200 K). This is in accordance with the previous diffusion studies [146]. Figure 2.4(a) depicts mean squared displacement of Na with respect to MD time steps for different temperatures, namely 1100 K (red), 950 K (green), and 800 K (magenta). The linear increment in MSD plot with time and the increasing temperature is evident from our calculation. It was observed during AIMD run that diffusion of Na in *a*-Ge was slower at first and impeded by Na size, but with increasing time step, it shows gradual increment. The Einstein equation was implemented to calculate the diffusivity of Na in Ge (D_{Na}) at various temperatures (Table 2.1), which was then extrapolated to room temperature (300K) using Arrhenius equation for diffusivity (Equation (2.7)) [146]. We calculated D_{Na} value for the Na_1Ge_{64} system to be about 4.876×10^{-9} cm^2/s at 300 K. This magnitude is comparable to reported data for Li diffusivity in graphite anodes which is of about 10^{-8} to 10^{-10} cm^2s^{-1} [151]. This shows that Na atoms diffuse in Ge faster than in other alloying anode materials by about one order of magnitude [92]. An Arrhenius plot (lnD vs 1000/T) for Na_1Ge_{64} system is shown in Figure 2.4(b). Such plot provides an estimate of migration activation energy for Na in *a*-Ge. Migration activation energy was derived to be 0.709 eV, which compares well with currently applicable LIBs [151] and thus holds a promise of good charge/discharge rate in Na-Ge anode based NIB. This activation energy for Na in *a*-

Ge is calculated from single atom diffusion model. However, diffusivity is expected to increase with Na concentration as it is established that dopant-dopant interaction (Na-Na in this case) significantly lowers the energy barrier by causing additional relaxation of surrounding atoms [140]. So, one can expect higher overall diffusivity in case of the $Na_{64}Ge_{64}$ system due to the presence of higher Na concentration during the process of charging and discharging.

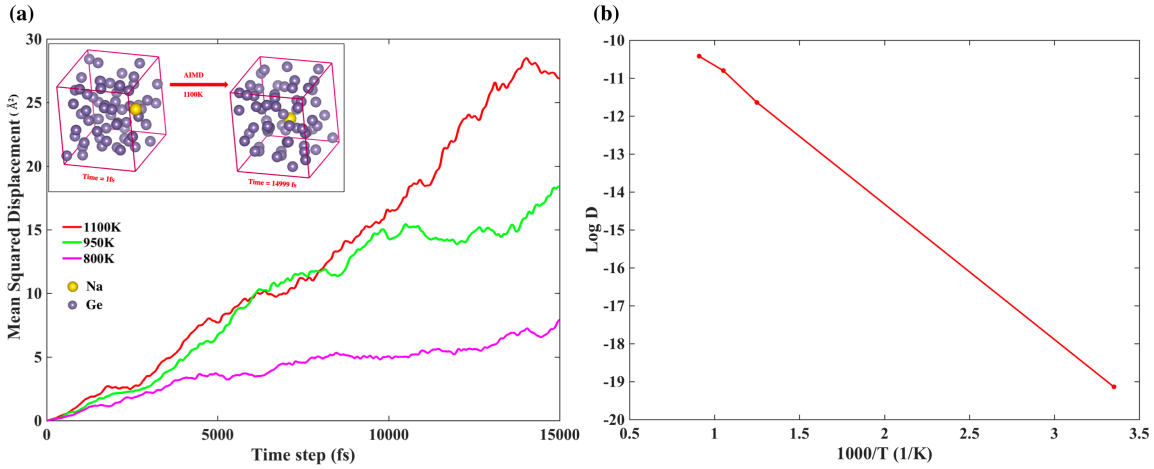

Figure 2.4 (a) MSD plot for Na in *a*-Ge with respect to time corresponding to different temperatures namely 1100K (red), 950K (green) and 800K (magenta). (b) Arrhenius plot of log of diffusivity vs inverse of temperature (1/K) for diffusion of Na in *a*-Ge extrapolated to room temperature.

Table 2.1 Mean Squared Displacement (MSD) and Calculated Diffusivities of Na in Ge

Temperature (K)	MSD (Å^2)	Diffusivity (cm^2/s)
1100	26.89	29.87 X 10^{-6}
950	18.3413	20.37 X 10^{-6}
800	7.928	8.80 X 10^{-6}

2.4 Summary

In summary, we investigated sodiation kinetics in *a*-Ge anode, which is the least explored alloying element of group 14 but has potential to be a promising anode for NIB due to its similarities to Li-Si system. We analyzed the intercalation potential and capacity correlation for intermediate equilibrium structures, and our computational results are in excellent agreement with the existing experimental data. Our equilibrium curve lies in middle potential values of experimental curve. From our first principle results, we also computed the volume expansion of Na-Ge alloy electrode to be approximately 149.51% in the fully sodiated state ($Na_{64}Ge_{64}$). It is well established that in Na-Ge battery system, starting with *a*-Ge, upon complete sodiation results in an amorphous system ($Na_{64}Ge_{64}$). However, not much information about the intermediate stages of Na-Ge system exists. In the present study, intermediate Na concentrations (6%, 19%, 31%, 50%, 69% and 88%) in Na-Ge system were assessed to identify any possible phase change during sodiation. We found that despite starting and final stable amorphous phases, system undergoes minute phase transitions to crystallinity for smaller Na concentrations (Na < 20%). This information was revealed in PCF analysis of Na-Na pairs in the system. While PCF of Ge-Ge pairs showed amorphous nature throughout, we observed peaks referring to crystallinity in Na-Na PCF plot for Na concentration below 20%. It was noted that after 50% sodiation, system was amorphous throughout. Moreover, we calculated diffusivity of single Na in *a*-Ge_{64} to be 4.876×10^{-9} cm^2/s at 300 K, which is greater than previously reported diffusivities of Na in other group 14 and 15 elements. Our systematic investigation yields in-depth insight into the sodiation kinetics and provides guidelines for experimentalists for optimal design of Ge-based NIB for real-life applications.

CHAPTER 3

INTERFACE STRENGTH OF SELENIUM WITH 2D GRAPHENE ADDITIVE

3.1 Introduction

Inspired by reported importance of graphene interface for Si anode, the present work investigates the 3D-2D interface between Se bulk and graphene. Presently, cathodes are the limiting factors for energy density in battery technologies. Elemental sulfur (S) cathode can deliver the high specific capacity of 1675 $mAhg^{-1}$, with its projected energy density being two to three times higher than conventional cathodes [152]. However, having the primary concern of shuttle effects [153] due to dissolution of Li-S reaction intermediates [154-156], S is being replaced by heavier chalcogens such as selenium (Se) [157-160]. Li-Se cathode is favored replacement for Li-S as Se possesses superior electrical conductivity ($1X10^{-3}$ $S.m^{-1}$ for Se and $5X10^{-28}$ $S.m^{-1}$ for S) and lithiation rates [161] [162]. Li-Se cathodes have reported good gravimetric capacity (678 $mAhg^{-1}$) and very high volumetric capacity (3253 mAh cm^{-3}) [163, 164]. Since Se is comparatively heavy and less reactive element than S [165] shuttle effects in Li-Se cathode due to dissolution of polyselenides are much controlled, if not negated. Chalcogens directly react with Li/Na to undergo a conversion-type reaction accompanied by shuttle effects and significant volume expansions, causing chemo-mechanical degradation. To overcome these, micro and mesoporous C has been used as an additive to Se [166]. The porous matrix of C provides a buffer space for the active electrode Se to expand at ease, maintaining the continuity of electronic contact. Electrochemical activity and cycle life of Se-C improve when morphology of C is shifted towards more refined nanostructures such as nanofibers [167],

carbon nanotubes[168] and graphene [55-57]. Therefore, in the latest studies, porous C is now being replaced by graphene in Se-C systems.

The electrochemical promise of graphene is already established; however, the greater challenge lay in characterizing the interface between graphene and active electrode material. In an experimental and computational study on Si over graphene substrate by Basu et al.[32], slipperiness of graphene surface proved to be effective in combating stresses in Si anode upon lithiation, thereby increasing the cycle life of the electrode. Low interface strength between Si and the graphene substrate was the primary determinant of electrode cycle life. While many prior studies claim that high adhesion between active electrode material and additive will be beneficial for battery cyclability [122-124], this study proves that low interface adhesion due to slippery graphene surface could be instead more favorable for the battery life. A latest report [169] suggests high interface strength between two materials can cause the formation of structurally-disconnected aggregates within electrode. This condition could be avoided if the interface strength between two materials is carefully adjusted along with other physicochemical factors. These findings emphasize the need for prior characterization of material interfaces before their respective applications.

In this chapter, an atomic-level detailed investigation of the Se-graphene interface is presented, which targets properties such as interfacial strength supported by interfacial bonding, and analysis is correlated to the respective application of Se-graphene systems in the batteries. A comparative investigation of amorphous Si/graphene interface is also presented to act as a baseline in this work. Differences in the interface strength of monoclinic and amorphous Se with the 2D hexagonal lattice of graphene are determined.

Se comes in several allotropic forms: monoclinic, trigonal, and amorphous. Being temperature and pressure-sensitive, it undergoes phase transformations during its applications, which remain less understood due to the marginal difference between structures of its different allotropes[170]. This work was published in *ACS Langmuir* in 2021 as '*Understanding the Strength of the Selenium–Graphene Interfaces for Energy Storage Systems*'.

3.2 Computational Details

All the first principle DFT calculations were done in VASP package [142]. Projector-augmented-wave (PAW) potentials were used to mimic inert core electrons, while valance electrons were represented by plane-wave basis set [143, 144]. Plane wave energy cut-off was set as 550 eV for all the structures taken, and convergence tolerance for all relaxations was maintained as 1.0×10^{-6} eV to ensure the accuracy of results. The GGA with the PBE exchange-correlation function has been taken into account [119]. Since the focus of this analysis is primarily on the interface of two materials, the vacuum interface model was used to calculate interface energies. For such systems, gamma centered 4 X 4 X 1 k-meshes were employed for good convergence and energy minimization was done by conjugate gradient method with Hellmann-Feynman forces less than 0.02 eV/Å. Additionally, our GGA functional was inclusive of vdW correction in order to incorporate the effect of weak long-range van der Waals (vdW) forces [171]. All DFT-based calculations were done with optPBE functional within vdW-DF-family, as implemented in the VASP package [172, 173].

Investigation of interface strength required surface energies of individual materials and energies of their interface systems. For surface energy calculation, material slabs with an added vacuum of 12 Å in z dimensions were subjected to DFT. For interfaced systems, vacuum interface model [126] with added vacuum of 14 Å in z-dimensions (normal to graphene plane) was used to calculate the interface energies. In total, we studied three Se interface systems: 3D/2D (*a*- and *c*-)Se_{64}/Gr and 3D/3D *c*-Se_{64}/Al for comparison. In addition to Se, physicochemical characterization of 3D/2D *a*-Si_{64}/Gr interface is also presented for correspondence. In present configuration, 64 is the number of Se and Si atoms in bulk, while Gr comprised of 112 and 60 sp^2 carbon atoms arranged in a hexagonal lattice, respectively. Atom count in Gr considers the surface area of *c*-Se_{64} crystal in (001) direction. In *c*-Se_{64}/Al system, monoclinic Se_{64} was interfaced with four atomic layers of Al as substrate. These structures are periodic in x-y dimensions.

Crystalline(*c*-) and amorphous(*a*-) phase of Se in interface were modeled (Figure 3.1) before the interface analysis. Monoclinic Se with eight-membered monomer rings S_8 was opted as *c*-Se. The latter has structural parameters such as interatomic bond lengths, bond angles, and dihedral angles similar to its other crystalline allotropes [170]. Starting from *c*-Se, amorphous selenium (*a*-Se) was derived by computational quenching [146, 174]. The quenching process required AIMD within the DFT. We performed systematic heating, cooling, and equilibration of Se for 5000 MD time steps with 1 fs time interval under the NVT canonical ensemble (similar to Ge). The highest temperature considered (5000 K) was far above the melting point of Se. The final amorphous structure was obtained via DFT optimization of the room temperature AIMD simulated lowest energy (local minima) structure.

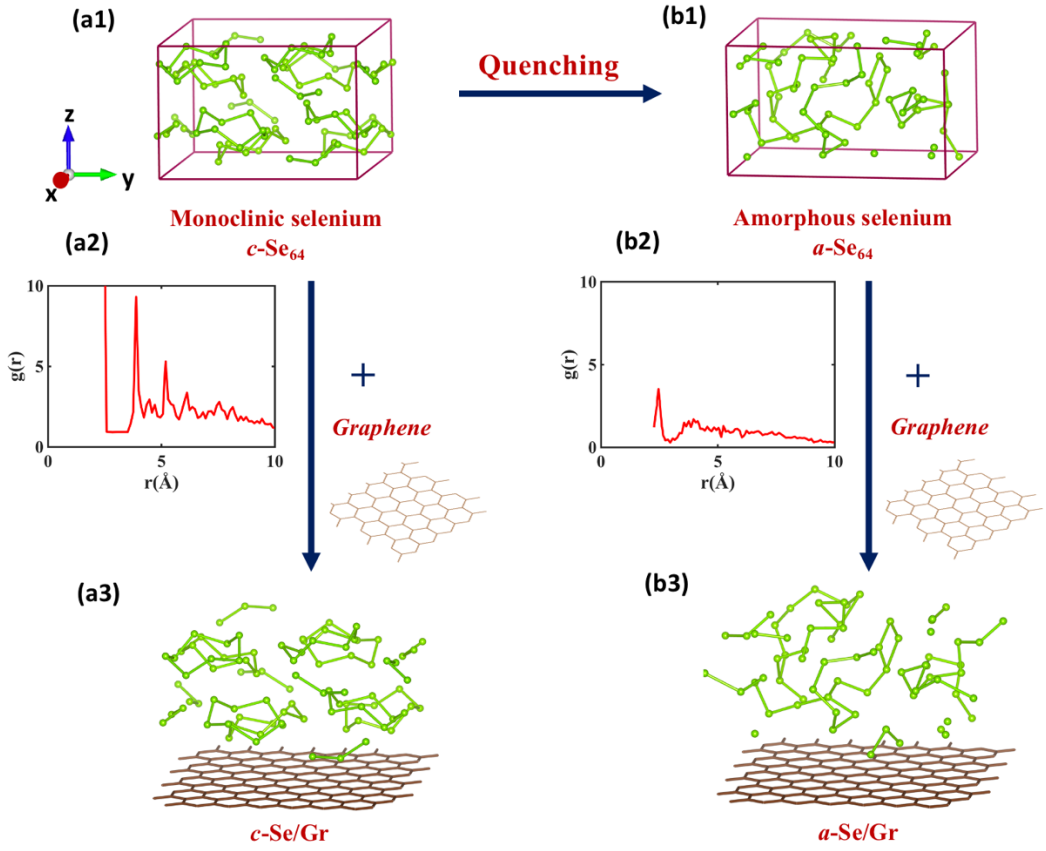

Figure 3.1 Schematic illustration of quenching process to generate initial Se structures. (a1) Optimized monoclinic Se (*c*-Se) having Se_8 rings. (b1) Optimized amorphous Se (*a*-Se) generated from a monoclinic crystalline Se (*c*-Se) with computational quenching. The structure is dominated by disintegrated forms of Se rings. (a2) Radial Distribution Function (RDF) plot for monoclinic Se (*c*-Se) with nearest neighboring distance of ~2.4Å. More than one prominent peak is symbolic of crystallinity. (b2) RDF plot for amorphous Se (*a*-Se) obtained after quenching of monoclinic Se. Nearest neighboring distance is ~2.38Å and only one prominent peak is noted with low intensity. RDF plots for *c*-Se and *a*-Se conform and differentiate the structures of optimized Se allotropes. (a3) Representation of initial structure of *c*-Se/graphene interface prior to the interface study. (b3) Representation of initial structure of *a*-Se/graphene interface.

3.3 Results and Discussion

3.3.1 Interface Strength Analysis

To evaluate the strength of Se-Gr interfaces, work of separation ($\mathbf{W_{sep}}$) for each interface system was computed. By definition, it is the energy per unit area required to separate the two materials completely in the direction normal to the interface. To accomplish this, slab models for (*a*-/*c*-) Se/Gr were created with vacuum in z-dimension to permit atomic relaxation and circumvent periodic influence, as shown in Figure 3.2. The standard description of $\mathbf{W_{sep}}$ is as follows

$$W_{sep} = \sigma_1 + \sigma_2 - \gamma_{12} = \frac{E_1 + E_2 - E_{12}}{A} \quad (3.1)$$

Here, $\boldsymbol{\sigma_1, \sigma_2}$ are surface energy of both the materials and $\boldsymbol{\gamma_{12}}$ is the interface energy. These are determined from total energies of slab 1, slab 2 and slab 3 as $\mathbf{E_1}$, $\mathbf{E_2}$ and $\mathbf{E_{12}}$, respectively. **A** is the area of contact at the interface. Besides Se/Gr, we also used similar slab models to calculate W_{sep} in *c*-Se/Al interface system. Details of slab energies and calculation of W_{sep} are present in the Table 3.1.

Table 3.1 Final Energies and Equilibrium Dimensions of Se Interfaces

S.no.	Interface system	DFT optimized energy (eV)			Area (Å^2)
		E_1	E_2	E_{12}	
(i)	*a*-Se/Gr	-870.177	-94.16146	-970.5632	285.1462
(ii)	*c*-Se/Gr	-870.17899	-106.32525	-969.91917	285.1632
(iii)	*c*-Se/Al	-249.09390	-106.3577	-371.6000	260.984

Note: For each interface system, $\mathbf{E_1}$ is energy of slab 1 of substrate, $\mathbf{E_2}$ is energy of slab 2 active electrode, $\mathbf{E_{12}}$ is the total energy of interface system as slab 3, and **A** is the area of contact at the interface.

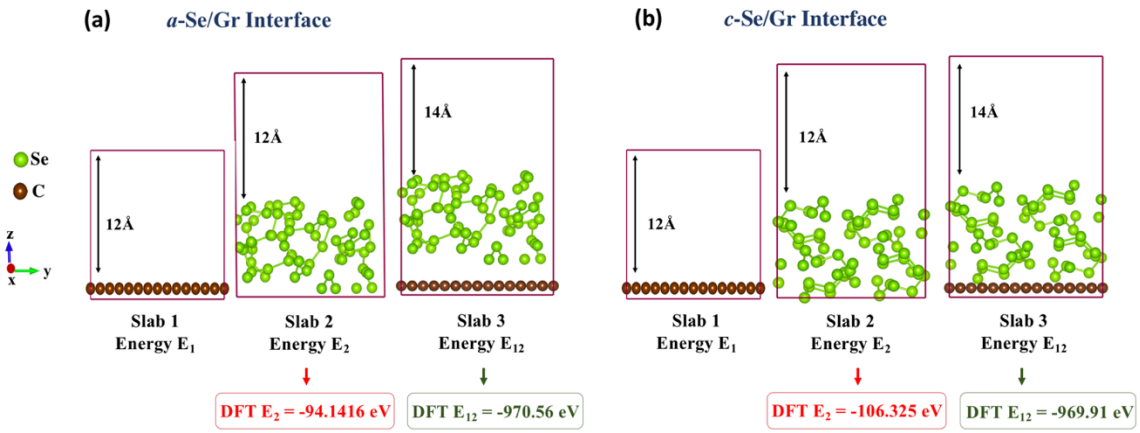

Figure 3.2 Vacuum interface models with three slabs taken for the work of separation calculations. (a) Three slabs taken for surface energy calculations of amorphous Se and Gr interface (*a*-Se/Gr). (b) Three slabs taken for surface energy calculations of monoclinic Se and Gr interface (*c*-Se/Gr). Vacuum of 12Å was added in z direction for slab 1 and 2, 14Å vacuum in z direction for slab 3 supercell containing the interface. E_2 for *a*-Se is higher than for *c*-Se denoting the lower thermodynamical stability of amorphous Se phase. The E_{12} of both the interface systems (*c*-Se/Gr and *a*-Se/Ge) is almost same.

Results of W_{sep} for different interfaces are summarized in Figure 3.3 and indicate that interface strength for Se-Gr systems (both *a*- and *c*-Se) is comparable to *a*-Si/Gr interface. Lower W_{sep} has been previously shown [32] to influence electrode performance positively by mitigating stresses in Si electrode during lithiation/delithiation cycle. These studies suggested that W_{sep} value of ~ 0.41 J/m^2 (green interface in Figure 3.3(c)) for amorphous Si over Gr (*a*-Si/Gr) permits a 'slippery' vdW interface where Si is loosely physiosorbed on Gr surface without any strong bonding. This allows these two materials to slip over one another in a frictionless manner without losing the mechanical contact. In present results, W_{sep} values for *a*-Se/Gr and *c*-Se/Gr are 0.34 J/m^2 and 0.43 J/m^2, respectively. The comparable interface strength of *c*-Se/Gr and *a*-Si/Gr propose long cycle

life of Se-Gr electrodes. This interface strength value between active electrode and graphene is expected to decrease with increasing concentration of Li in the electrode (presented in Appendix B). Likeliness between Si/Gr and Se/Gr interfaces suggests interface adhesion at Se electrode and Gr interface will decrease with increase in Li concentration.

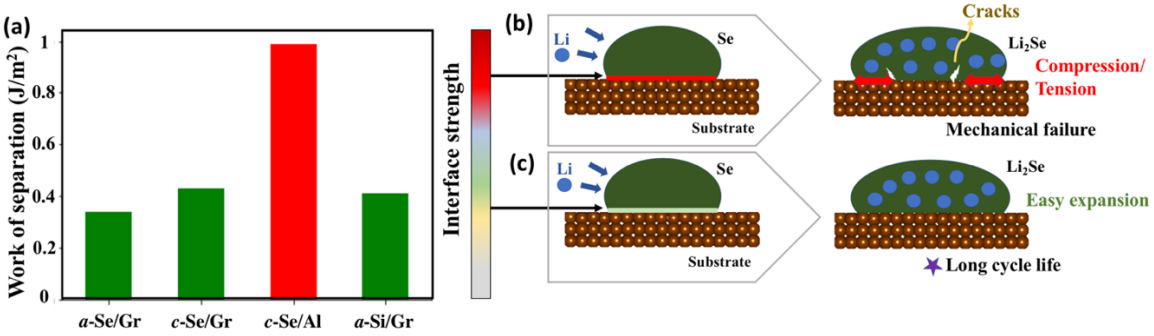

Figure 3.3 Interface strength quantified by work of separation (W_{sep}) results. (a) Interfacial work of separation for relaxed *a*-Se/Gr, *c*-Se/Gr, *c*-Se/Al and *a*-Si/Gr interfaces. (b)Schematic representation of an interface under 'high interface strength' condition denoted by red color, facing compressive stresses during Li incorporation in LIBs ultimately leading to crack propagation and mechanical failures. (c) Schematic representation of a contrasting 'low interface strength' condition as seen in the case of graphene interfaces and denoted by green/yellow here. Passive interface strength permits easy expansion and contraction to the active electrode material.

As alloying electrodes undergo continuous phase changes during battery cycle, Se will have an added advantage of similar interface strength during its phase transitions (*c*-Se ↔ *a*-Se) as compared to its complementary electrodes. W_{sep} of *a*-Se/Gr (0.34 J/m^2) is less only by 20% of *c*-Se/Gr (0.43 J/m^2), primarily due to the structural similarities between the two phases. *a*-Se derived by the quenching process was similar to *c*-Se in terms of first neighboring Se-Se distances (~2.4Å in Figure 3.1). The only critical difference between

the two allotropes of Se is that in *a*-Se, Se_8 rings break to form different-sized polymeric chains. The present structures of Se allotropes are in tune with previous studies where it is emphasized that structural parameters such as interatomic bond lengths, bond angles, and dihedral angles are comparable among Se crystalline allotropes [170]. Thus, *a*-Se structure derived from the quenching of *c*-Se are dominated by large chain molecules having each Se atom surrounded by two immediate neighbors, with interatomic distances similar to parent *c*-Se [170, 175]. The impact of structural variations on the interface strength of Se/Gr systems could be understood from Equation (3.1) where W_{sep} depends on the difference between E_{12} and the sum of energies of the individual materials ($E_1 + E_2$). The low interface energy ($\boldsymbol{\gamma_{12} = E_{12}/A}$) represents two materials are able to come together to form a stable interface. In our calculations, the interface energy ($\boldsymbol{\gamma_{12} = E_{12}/A}$) of both the interface systems (*c*-Se/Gr and *a*-Se/Ge) is almost same (Figure 3.2). However, the overall interface strength (W_{sep}) drops slightly in *a*-Se/Gr system (0.43 J/m^2 $\rightarrow$ 0.34 J/m^2) due to comparatively high surface slab energy (E_2 in Figure 3.2) and lower thermo-dynamical stability of *a*-Se phase. The disintegrated forms of Se rings dominate the *a*-Se/Ge structure, resulting in high E_2. On the other hand, monoclinic *c*-Se and Gr interface system is devoid of any lattice mismatch associated lattice distortions. The 8-membered rings of Se are mostly conserved in the stable interface system with Gr. Upon optimization, there is only a slight vertical condensation (shown in Appendix C) of Se crystal, resulting in minor distortions of dihedral angles and low interfacial gap (*d*), which works in favor of the interface in establishing a beneficial contact with Gr.

In addition to the cycle life and phase transition, lower interface strength between Se and Gr can be beneficial in designing the electrode morphology [169]. In contrast,

interface strength in *c*-Se/Al system was examined by evaluating W_{sep}. The replacement of 2D Gr by a 3D Al affected the interface strength with a two-fold increase (0.99 J/m^2 red interface in Figure 3.3). This high W_{sep} is associated with 'non-slippery' high adhesion conditions dominated by repeated compression and tension in the interfacial region (red interface in Figure 3.3(b)). Al is a conventional current collector used at cathode end in LIBs, and our results suggest that by reducing the surface contact between Se and Al, cycle life of Se electrode can be enhanced. This contrasting adhesion of Se with Gr and Al advocates the use of Se-Gr electrodes in battery applications.

3.3.2 Bonding at the Interface

The low interface strength and slippery surface of Gr pose an essential question - how long does the Se-Gr interface stay intact? Se is previously reported to peel off from SiO_2/Si surfaces by slight mechanical exertion due to a lack of mechanical interlocking and chemical interaction [176]. This condition was improved by inserting an inconsistent intermediate layer of Indium (In) between Se-SiO_2 interface. A non-metal like Se could then be held in place by forming a surface alloy of In_2Se_3. In the case of 2D materials such as Gr, even with Se-Gr interface strength being similar to Si-Gr interface, Se-Gr might still lack stability due to polarity and absence of dangling bonds as prevalent in the case of Si [177, 178]. Applicatory longevity of Se interfaces needs to be further investigated by utilizing a comprehensive analysis of bonding. In this section, we discuss the persistence of Se-Gr interfaces as the function of electron distribution across the interface.

Electron redistribution is a prominent reason for interface strength and can throw light on the bonding phenomenon at the interface. The overall electron exchange between

3D Se bulk and 2D Gr is studied in optimized interface supercells via Bader charge analysis using scripts by Henkelman group [179]. Bader charge analysis quantifies atomic charges based on the charge density in the bader volume of each atom in the relaxed structure and calculates net charge transfer across the interface (**Δq)**. In light of our used pseudopotential, all the C, Si, Se, and Al atoms in the system were taken to have 4, 4, 6, and 3 valence electrons, respectively. Charge distribution on Gr was computed by summing electronic charges on all the carbon atoms in the system ($\mathbf{q_c}$). Then the total charge transfer across the interface was calculated by

$$\Delta q = q_c - 4 \times c \tag{3.2}$$

where ***c*** is the number of carbon atoms in the system. The resultant values are presented in Table 3.2 for all considered Gr interface systems. The positive value of Δq indicates the number of electrons Gr gained when in contact with the bulk material, while a negative value represents the loss in electrons. The relation between the interface strength and the net charge transfer across the interface, $\mathbf{W_{sep} \propto |\Delta q|/ d^2}$, for Se interfaces compares well with some previous works on Pt-Gr and Si-C interfaces [126, 180]. In *a*-Se/Gr, *a*-Se gains net ~0.2556 electrons from Gr, leading to *p*-type doping in the latter. We observed that in *a*-Se structure, Se atoms broken from the chains, adsorb on Gr surface by gaining more electrons (illustrated in Figure 3.4(a)). This result is consistent with a previous work by Nakada et al.[181] which highlights while most atoms lose electrons to Gr surface, non-metals from Group 16 and 17 take up electrons from Gr. Therefore, Se atom gains about $0.01e^{-1}$ when adsorbed on Gr surface. Our results verify that in an amorphous state,

interfacial Se atoms exhibit individualism and adsorb on Gr surface with similar characteristics.

Direction of net charge transfer is reversed in the crystalline interface system (Figure 3.4(b)), where *c*-Se loses electrons to Gr (~$0.312e^{-1}$). Atoms on Se_8 in the interfacial regions have less electrons than the atoms in Se_8 farther from Gr. This tendency of Gr to gain electrons from interfacing 3D bulk is steady in *a*-Si/Gr system where net $0.4226e^{-1}$ is gained by Gr (summarized in Table 3.2). These Δq values at Gr interfaces emphasize that physisorption is the primary mode of bonding at Se/Si - Gr interfaces. Additionally, a very distinctive interface is noted between *c*-Se and Al in Figure 3.4(c), where Se_8 rings at the interface break into individual atoms to form strong covalent bonds with Al surface. There is a surface reaction between Al and Se surface atoms resulting in $\Delta q = 4.5\ e^{-1}$ between Se and Al substrate. This reaction between Se and Al will result in the loss of active Se for reaction with oncoming adatom in batteries (e.g., Li in Lithium batteries).

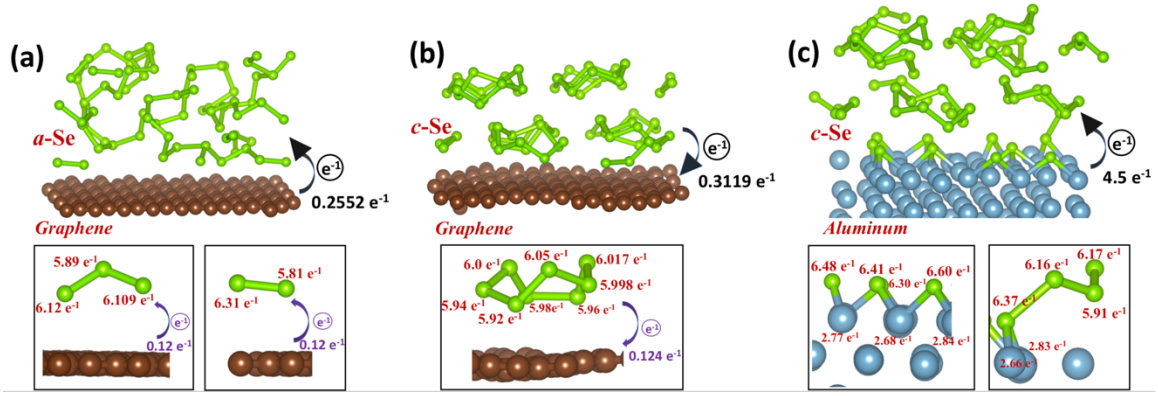

Figure 3.4 Distribution of electrons on Se atoms present at the graphene and aluminum interfaces. (a) Illustration of net charge transfer ($\Delta q = 0.2552\ e^{-1}$) from Gr surface to *a*-Se at *a*-Se/Gr interface. Se atoms detached from Se chains and attached to fewer than 2-3 Se atoms, adsorb on Gr surface by gaining more electrons (~0.12 e^{-1}). (b) The net charge transfer ($\Delta q = 0.3119\ e^{-1}$) at *c*-Se/Gr interface is directed towards Gr. Se atoms within Se_8 rings in the interfacial region have lower number of electrons than Se atoms farther from Gr surface. (c) Optimized view of *c*-Se/Al interface where Se_8 rings at the interface break into individual atoms to form covalent bonds with surface Al atoms. This surface reaction between Al and Se results in comparatively high net charge transfer ($\Delta q = 4.5\ e^{-1}$) between Se and Al substrate. All the charges were obtained via Bader charge analysis.

Table 3.2 Summary of Electron Distribution across Gr Interfaces with Bulk Se and Si

Systems	**W_{sep} (J/m^2)**	**$d\phi/dz$ (eV/Å)**	**Δq (e^{-1})**	***d* (Å)**
***a*-Se/Gr**	0.34	3.08	-0.2552	3.33
***c*-Se/Gr**	0.43	3.03	0.3119	2.87
***a*-Si/Gr**	0.41	2.18	0.4266	3.06

Note: For each interface system, the associated interface strength value is represented by **W_{sep}**. The potential energy gradient across the interface is denoted by **$d\phi/dz$,** net charge transferred across the interface is given by **Δq,** where positive value denote charge acquired by graphene while negative value denote the charge given by graphene to the bulk, and ***d*** is the distance between Gr and lowest **Se/Si** atom.

3.3.3 Ease of Electron Exchange Across the Interface

Net electron exchange (Δq) at Si-Gr interface is quantitatively more than Se-Gr interfaces in Table 3.2. This comparative ease of electron exchange at Si-Gr interface can be understood with the potential gradient and charge separation analysis presented in Figure

3.5. To bridge the electronic character across Se-Gr interface, we mapped the potential step (**ΔV**) between two materials and defined it as potential gradient (**dϕ/dz**) by dividing the difference in electrostatic potential at the interface with the interface gap (***d***). The computed electrostatic potential (**V**) on atoms was averaged in x-y plane for every unit z dimension (normal to Gr plane) [182]. Potential of Se and Gr at the interface were acquired by averaging $\mathbf{V_{Se/Gr}}$ in the z dimension [183]. Potential gradient across the interface was determined by

$$\frac{d\phi}{dz} = \frac{V_{Se} - V_{Gr}}{d} \tag{3.3}$$

where $\mathbf{V_{Se}}$-$\mathbf{V_{Gr}}$ is the difference of **V** between Se and Gr atoms at the interface. The interfacial gap (***d***) in the z dimension is denoted by the distance of lowest Se atom from the Gr surface in Figure 3.5(a1,b1,c1).

Lower potential gradient promises ease of interaction at the interface (dϕ/dz ~0 for same materials), while large potential step is indicative of incohesive interface with less scope for electron exchange and bonding. The dϕ/dz values for Se and Si interfaces with Gr are summarized in Table 3.2, along with their associated W_{sep} and electron exchange results. Figure 3.5(a1,b1) demonstrates the potential step that developed across the Se-Gr interfaces and the resultant gradients. The red curve is the averaged electrostatic potential in the x-y plane, and purple is the averaged V across the z dimension. The difference in average potential of *a*-Se and Gr in the interface system is the highest (Figure 3.5 (a1)). This results in a sizeable potential step and a steep value of dϕ/dz (3.081 eV/Å). A similar trend is noted in the case of *c*-Se/Gr interface in Figure 3.5(b1), where dϕ/dz value is 3.03

eV/Å and d = 2.86Å. This curtailed value of dϕ/dz and d indicate *c*-Se/Gr interface system might be slightly superior to its amorphous counterpart in terms of bonding ability. In comparison to Se-Gr interfaces, *a*-Si/Gr has reduced potential step across the interface and resulting dϕ/dz (2.18 eV/Å) is significantly lower (Figure 3.5(c1)). Hence, we observe higher electron exchange at *a*-Si/Gr interface than *c*-Se/Gr despite having comparative W_{sep} values. The dϕ/dz values indicate that Se is less likely to remain bonded with Gr as compared to the case of Si/Gr. Absence of interfacial bonds at Gr interfaces is further evident with distant potential wells near the interface.

Charge density in the interfacial region was visualized by charge separation analysis. Charge separation scheme at the interface was extracted by subtracting charge density of individual materials from that of the entire system, and difference is plotted with an isosurface of 0.00024 e $Å^{-3}$. The resultant plots in Figure 3.5(a2,b2,c2) provide the extent of interaction between the atomic systems and are consistent with our Δq and dϕ/dz results. Charge separation scheme for Se interfaces exhibits hardly any overlap of electron cloud between the two materials. Nevertheless, there is a presence of strong dipole at the interface due to accumulation of negative and positive charges, as indicated by red and green isosurfaces. Charge separation of *c*-Se/Gr (Figure 3.5(b2)) suggest the crystalline phase of Se is better than *a*-Se in forming a reliable interface with Gr as there is some overlap of positive and negative isosurfaces at the interface. Charge separation scheme of *a*-Si/Gr interface exhibits a better overlap of electron cloud between the two materials. These findings further imply that Se-Gr interfaces are not as amicable as Si-Gr, and Se alone can easily disintegrate from Gr surface upon external stimulation.

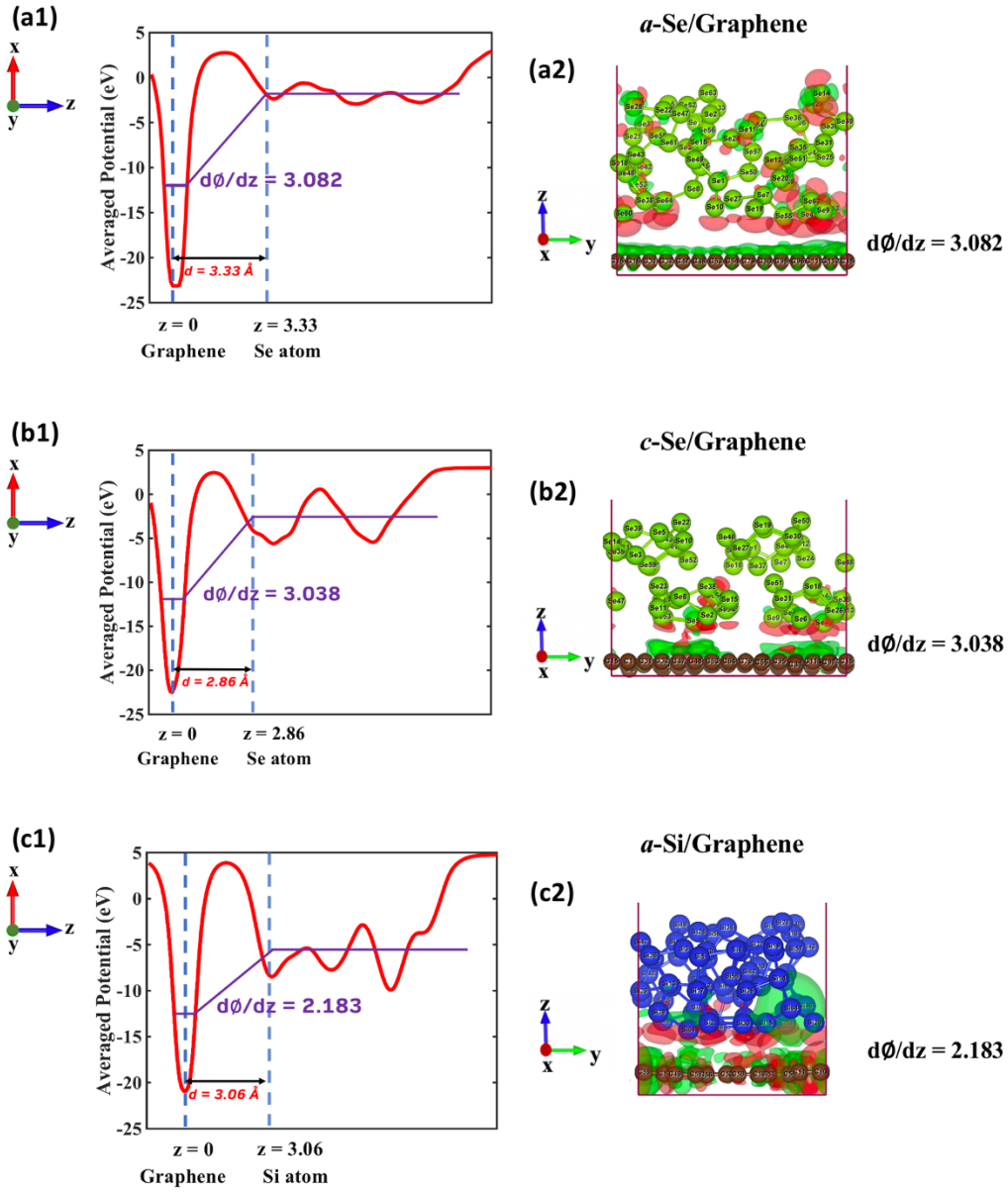

Figure 3.5 Comparison of potential gradient and charge separation at graphene interfaces. (a1, b1, c1) Planar average potential curves at graphene interfaces with amorphous Se, crystalline Se and amorphous Si. The red curve is the averaged electrostatic potential in the x-y plane and purple is the averaged potential across the z dimension. There is a potential step across all the interfaces which results in potential gradients (dϕ/dz). *d* denotes the distance of the nearest Se/Si atom with respect to Gr sheet. (a2, b2, c2) Charge separation schemes for Gr interface with amorphous Se, crystalline Se and amorphous Si. Charge accumulation and depletion are shown in red and green, respectively. In comparison to Se-Gr interfaces, *a*-Si/Gr has reduced potential step (dϕ/dz = 2.18 eV/Å) and significant overlap of electron clouds across the interface representing ease of interfacial interaction. Large potential gradient (dϕ/dz) at Se/Gr interfaces is indicative of incohesive interface with less scope for electron exchange and bonding.

3.4 Summary

In summary, we performed a comparative study of interfacial characteristics for Se-Gr interface and distinguished Si-Gr interface. By first principle calculations, we probed Gr interface with two different Se allotropes, namely monoclinic and amorphous, for strength, interaction and long term stability. Our work of separation results show that Se/Gr interfaces have interface strength (0.43 J/m^2 and 0.34 J/m^2) comparable to amorphous Si/Gr interface (0.41 J/m^2). Therefore Se/Gr interface systems will retain the benefits of Si/Gr interface in terms of mitigating interfacial stresses during ion battery cycles. There is only a small variation in interface strength when Se changes phase from monoclinic to amorphous. The structural analysis of the interfaces reveals the cause of this minimal variation in interface strength to be similarities in Se-Se bond lengths and polymeric chains among Se allotropes. This gives Se/Gr electrodes an advantage over their contemporaries, as it could be assured that interface strength will not undergo extreme transitions during phase changes. However, Se/Gr interfaces can unbind quite easily due to polarity (potential gradient $d\phi/dz = 3.03$ eV/Å) and lack of stable chemical interaction (net electron exchange $\Delta q = 0.3119\ e^{-1}$) between both the materials, if electrode morphologies are not carefully designed. The bader charge analysis of Gr interface with amorphous and crystalline Se denote *p*- and *n*- type doping of Gr, respectively.

CHAPTER 4

ELECTROCHEMICAL PERFORMANCE OF GRAPHENE SUPPORTED SELENIUM CATHODE FOR POTASSIUM ION BATTERY

4.1 Introduction

There is a looming danger of lithium (Li) supply being outrun with Li demand by next decade due to Li's scarcity [6, 7, 16]. In Section 1.3, we overview electrodes for NIB and KIB that are potential alternatives of LIBs. This Chapter focuses on exploring electrochemical potential of graphene enclosed selenium cathode that was modeled in Chapter 3 for KIBs.

Se-graphene combination has been a successful cathode for LIBs with high capacities and controlled shuttle effects [55-57]. The energy storage mechanism in KIB is similar to LIBs except for the ion carriers. Thus, the electrode intercalation mechanism in KIB systems can still result in unfamiliar reaction mechanism. This calls for careful tailoring of the structural design of electrodes for KIB [19].

Cathodes have been an area of challenge for KIBs due to large atomic radius of K atoms. Encouraged by the success of alloying cathodes in LIB [154-156, 162-164], Liu et al. were the first to report performance of Se cathode confined in carbonized polyacrylonitrile for KIB in 2017 [184]. Active Se in composite maintained a reversible capacity of 396 $mAhg^{-1}$ with K_2Se as a final discharged product. Se and S cathodes have shown a good promise for ion batteries, albeit concern of shuttle effects due to dissolution of reaction intermediates in the electrolyte [154-156, 162-164]. Being heavier and less reactive shuttle effects in Se-based cathodes can be better controlled with a confining C-based matrix. The role of matrix goes beyond polyselenide confinement to providing buffer

space for easy expansion and contraction of Se during battery cycles without losing electrical contact. To date, several Se-C composites have been electrochemically investigated as cathodes for KIBs with intricate nanostructures and compositions [185-190]. Limited reports exist where Se enclosed in a matrix of refined C lattice such as graphene has been investigated for KIBs [185, 191]. Conclusions in these studies were similar to the LIBs where electrochemical activity and cycle life of Se cathode improves when the morphology of C matrix is shifted towards carbon nanotubes and graphene [55-57, 168].

Despite this electrochemical stability of Se cathode with graphene-based matrix, there is a lack of studies that bring microstructural changes in graphene-supported Se to light when compared to the understanding already developed on microstructures in porous carbon encapsulated Se [192]. In this chapter, we bridge microstructural changes at graphene-Se interface upon deintercalation/intercalation of K with the electrochemical voltage of cathode using first principle calculations.

4.2 Computational Details

The exact chemical steps in the preparation of Se-C nanostructured electrodes can deviate based on targeted nanostructure and C matrix [19, 193, 194]. Se infusion process in graphene-based matrix typically involves high temperature conditions followed by condensation [195, 196]. This results in evenly distributed Se on the substrate surface [163]. In these set-ups, Se is mostly in amorphous form with long Se_n chains. Alternatively, Se_8 rings are converted to Se_n chains after the first cycle and remain for the rest of the battery life [197]. Structural parameters such as interatomic bond lengths, bond angles, and

dihedral angles are comparable among pristine Se allotropes [170, 175] ,yet here, graphene matrix surface directs the aligned distribution of Se. We modeled our a-Se/Gr cathode keeping experimentally synthesized structures in mind [195].

To generate 3D periodic configurations of a-K_xSe cathode supported over graphene substrate, we started with an optimized amorphous a-Se_{30} system (Figure 4.1(a)) and sequentially added 6 K atoms at a time until a-$K_{60}Se_{30}$ (a-K_2Se) is achieved (Figure 4.1(b)). After each potassium addition step, K atoms were allowed to diffuse in the cathode during an ab initio molecular dynamics simulation (AIMD) run and then relaxed with density functional theory (DFT) until energy-optimized a-K_xSe structures were obtained. Volume of the simulation cell was allowed to ease in all dimensions. Between initial Se and final a-$K_{60}Se_{30}$ (Figure 4.1(a) and (b)), 183.52% volume expansion was noted. The simulation cell's base also expanded during potassiation, and its x-y dimensions were used to determine graphene substrate's size. The final a-$K_{60}Se_{30}$ bulk configuration was placed on top of a periodic graphene lattice containing 96 sp^2 hybridized carbon atoms with the interfacial gap of ~2.8 Å to form the a-$K_{60}Se_{30}$/Gr interface (a-K_2Se/Gr). The surface area of graphene substrate was equivalent to the x - y surface of final a-$K_{60}Se_{30}$. We further let the atoms diffuse and re-adjust on the graphene lattice during an AIMD run followed by DFT optimization of structure. For graphene-supported K-Se cathode, optimized a-K_2Se/Gr configuration was considered the final discharged product (Figure 4.1(c)). Starting from this a-K_2Se/Gr structure, 6 K atoms were sequentially removed, followed by AIMD run for 300-500 iterations and complete energy optimization of structures obtained every 100 steps for each configuration, until a-Se_{30}/Gr was left (Figure 4.1(d)). Upon complete charging (depotassiation), the end structure resembles a-Se clusters distributed

on a periodic graphene mesh (Figure 4.2(a)). This computationally modeled configuration is close to experimentally synthesized nano architectures of active electrodes and graphene [195, 198-200]. Interlayer spacing between the graphene sheets in charged (depotassiated, Figure 4.2(a)) and discharged (potassiated, Figure 4.2(b)) a-Se/Gr cathode are 9 Å and 18.57 Å, respectively. These microporous confinement orders of Se between graphene sheets are also similar to the earlier Se confinement report [201].

All AIMD and DFT simulations were performed in VASP [142]. Inert core electrons were mimicked by Projector-augmented-wave (PAW) potentials and valance electrons were represented by plane-wave basis set with energy cut off at 550eV [143, 144]. The GGA-PBE exchange-correlation function was taken into the account for all calculations [119]. AIMD simulations were run with 1 fs time interval, temperature set at 300 K within NVT ensemble and 2 X 2 X 2 gamma centered k-meshes. For all DFT calculations, conjugate gradient method was employed for energy minimization with Hellmann-Feynman forces less than 0.02 eV/Å and convergence tolerance set to 1.0×10^{-4} eV. Gamma-centered 4 X 4 X 4 k-meshes were taken for good accuracy. Only for graphene supported cathodes, GGA functional was inclusive of vdW correction to incorporate the effect of weak long-range van der Waals (vdW) forces [171]. All calculations for graphene supported cathode were done with optPBE functional within vdW-DF-family [172, 173].

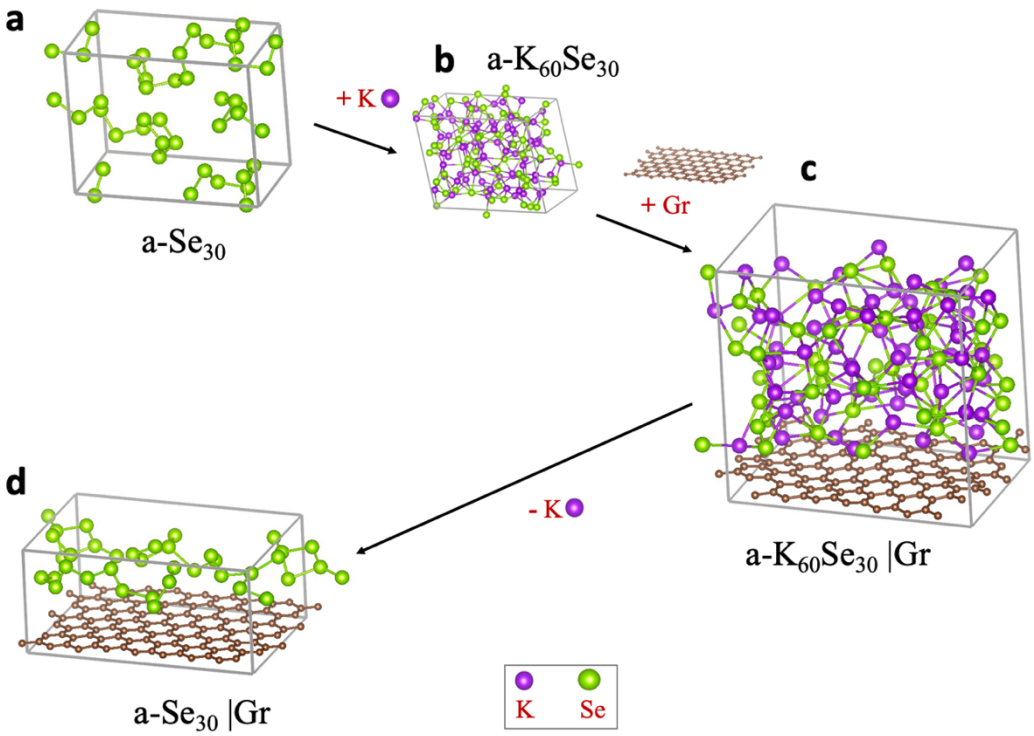

Figure 4.1 (a) Atomic representation of initial optimized amorphous Se (a-Se_{30}) generated from a crystalline Se with computational quenching. The structure is dominated by disintegrated forms of Se rings as chains with nearest neighboring distance of ~2.4Å. (b)Miniaturized view of a-$K_{60}Se_{30}$ (a-K_2Se) generated after complete potassiation (discharging). The volume is expanded by 183.52 %. (c) Atomic representation of a-$K_{60}Se_{30}$ /Gr (a-K_2Se/Gr) system. Graphene with surface area equivalent to the base of *a*-$K_{60}Se_{30}$ was added in z dimension. (d) Completely charged *a*-Se_{30}/Gr cathode post potassium removal. The structure once again forms Se chains that are slightly condensed towards graphene surface.

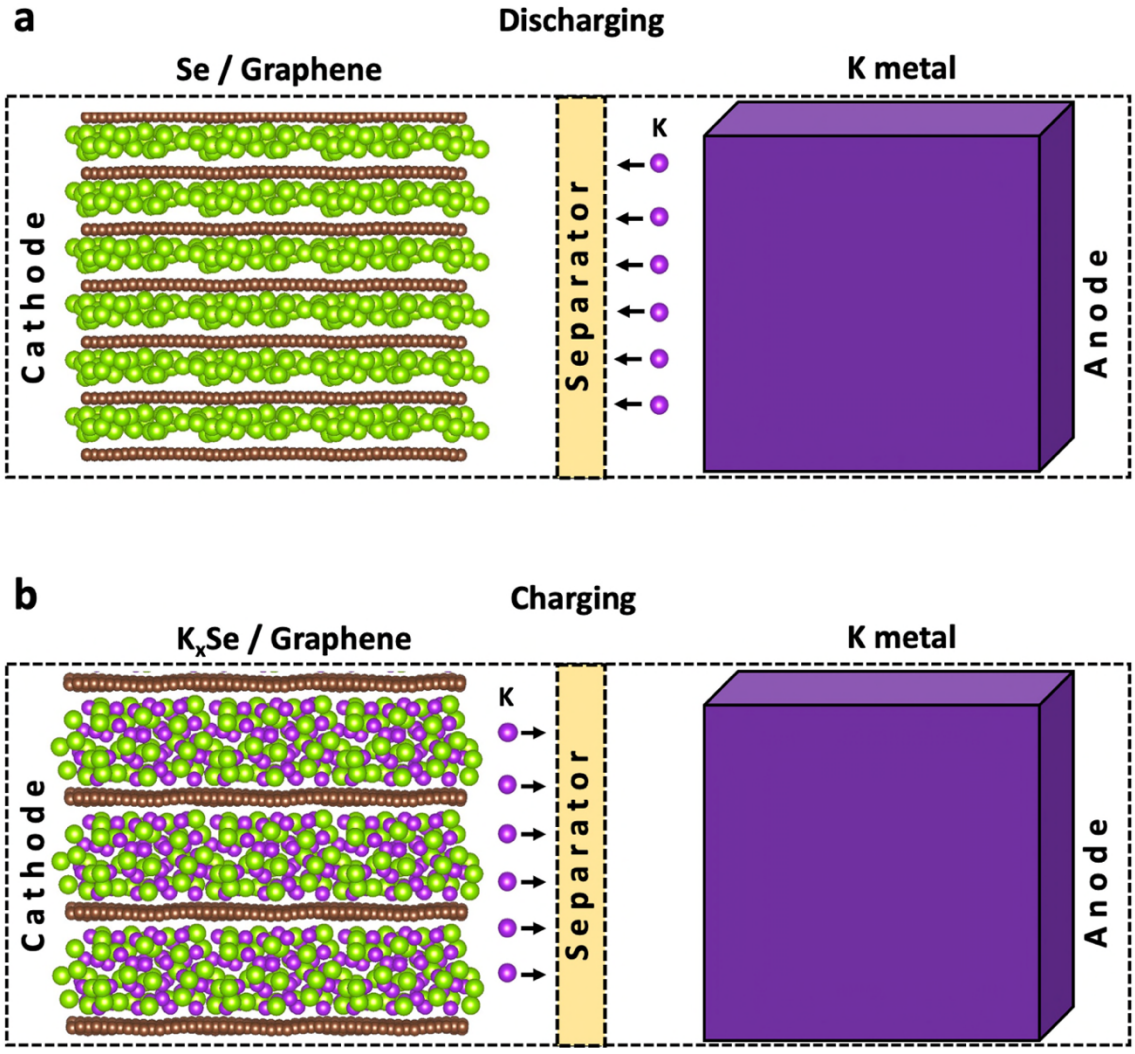

Figure 4.2 Schematic representation of a selenium-graphene heterostructure cathode half cell during (a) discharging and (b) charging process. Interlayer spaces between two graphene sheets represent pores for Se in graphene-based matrix and is approximately 9Å (depotassiated) and 18Å (potassiated).

4.3 Results and Discussion

4.3.1 Potassium Segregation at the Interface

The presence of graphene substrate is reportedly beneficial for the Se electrode to control dissolution of polyselenides in electrolytes and provide a supportive matrix to the volume fluctuating Se electrode [195, 199, 200]. However, graphene and pristine a-Se do not form a very reliable interface from a physicochemical perspective. On a positive note, low interface strength between Se and graphene means Se can easily expand/contract during the battery cycle and evade high mechanical stresses [125, 202]. But on the downside, the two materials are held by weak vdW forces and have a very high potential gradient at the interface [202]. This condition is subjected to change as K atoms enter Se bulk. Alkali earth metals such as K bind strongly to graphene surface than Se [203]. This opens possibilities of microstructural changes in a-K_xSe cathode that could differ in a graphene-supported cathode from its free counterpart. Figure 4.3 presents relaxed atomic structures of a-K_xSe cathodes with and without graphene substrate, together with the respective variations of atomic K/Se ratio along the z-dimension.

To determine the influence of graphene substrate on the distribution of K and Se atoms, the atomic K/Se ratio profile is traced in three high K cathode configurations: a-K_2Se, a-$K_{1.6}$Se, and a-KSe. Figure 4.3(a) demonstrates the K/Se ratio profiles in cathode configurations with graphene support while their graphene-free counterparts are analyzed in Figure 4.3(b). Simulation cells are divided into four bins (bin ID = 1, 2, 3, 4) along z-direction. In graphene supported structures, the bottom 3.4 Å is not included in the bins considering it to be the vdW radius of graphene and represents volume occupied by only graphene. The rest of the simulation cell (z - 3.4 Å) is divided into bins of width ranging

from 3.18 Å to 3.8 Å depending upon the a-K_xSe thickness. For graphene-free a-K_xSe, bin widths ranged between 3.6 Å to 4 Å. The atomic K/Se ratios in each bin are marked with red and connected by blue line to view the pattern. The average K/Se ratio in the entire bulk (x in a-K_xSe) is plotted as the dashed yellow line for comparison purposes.

In graphene supported a-K_xSe (Figure 4.3(a)), two prominent regions can be noted based on K/Se ratio analysis: K-rich and K-deficient. K/Se ratios in bins 1 and 4 (close to graphene surface) clearly demonstrate higher K concentration. In contrast, bin 2 (further from the graphene surface) has a low K concentration in all three cathode configurations (Figure 4.3(a)), i.e., K/Se = 2, 1.6, and 1. Combined K/Se ratio in bins 1 and 4 is continually above-average (yellow line) bulk K/Se ratio. On the other hand, K/Se ratios in bins 2 and 3 mostly fall lower than average (yellow line). These results indicate the affinity of K to graphene surface and the possibility of K segregation at the interface. A clear K concentration gradient is observed in sub-interfacial region (bin ID 1,4) and central region (bin ID 2,3). The balance of K concentration in electrode could be decided by observing bin-wise K/Se ratios (red) with respect to the average value (yellow line). The K concentration in completely discharged cathode a-K_2Se/Gr (Figure 4.3(a1)) appears to be balanced. It means, for bins 1 and 3, K/Se concentration is same as average value (*i.e.*, x = 2). However, for bins 2 and 4, the K concentration (x) is less and more than average (x=2), respectively. In contrast, for a-$K_{1.6}Se$/Gr (Figure 4.3(a2)) and a-KSe/Gr (Figure 4.3(a3)), K concentrations are higher than the average (x=1.6 and x=1, respectively) in three out of four bins (bin 1,3,4).

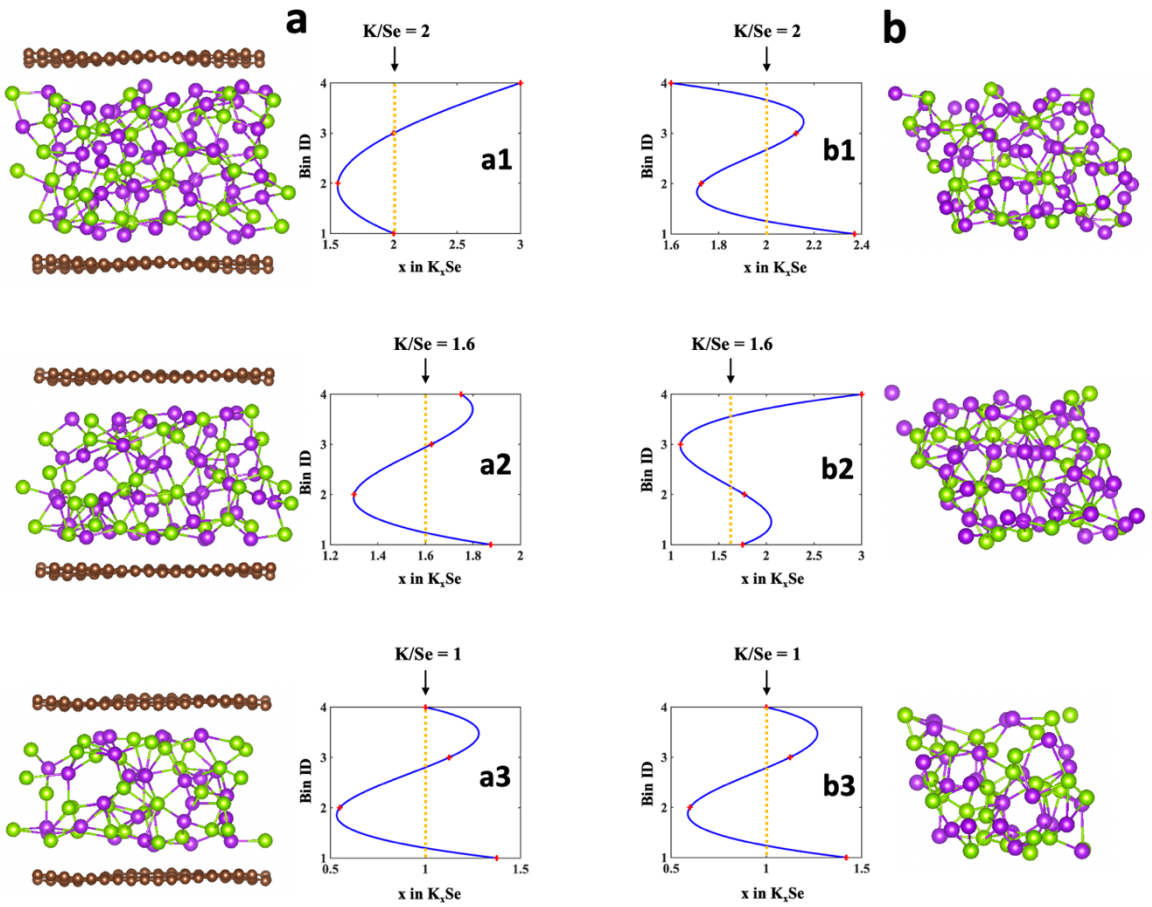

Figure 4.3 Degree of K segregation and K/Se ratio profile for (a) periodic a-K_xSe /Gr and (b) periodic a-K_xSe without any graphene support. Structures are divided into four bins along z dimension noted as Bin ID 1- 4. K/Se ratios in each bin are marked with red and connected by blue line to preview the pattern. Average K/Se ratio in the entire bulk is plotted as dashed yellow line for comparison purpose. Graphene supported cathodes with over-all high average K ratio(>1) demonstrate higher K concentrations closer to graphene surface (Bin ID 1 and 3). In periodic a-K_xSe cathodes without graphene substrate, K concentration peaked alternatively in bins. In cathodes with lower average K/Se ratio (<=1), distribution of K is nearly same irrespective of graphene presence.

The results in graphene-free a-K_xSe cathode configurations (Figure 4.3(b)) demonstrate K/Se ratios fluctuate in bins alternatively. Without graphene, a-K_xSe cathodes are continuous periodic bulks. Understandably, a bin with high K concentration is followed by bin with low K concentration. No distinct pattern of K distribution can be recognized

without a substrate. Moreover, K/Se ratio plot for low K concentration cathode in Figure 4.3(b3) (K/Se <=1) is similar to graphene supported ones (Figure 4.3(a3)) indicating at low K content, segregation effect of graphene is reduced. All the a-K_xSe structures remained amorphous for both graphene-supported and graphene-free cases (Figure 4.4). However, it is unclear whether the segregation of K atoms at the graphene interface results in forming any new phase or phase boundary. The model size considered in our study is too small to determine any phase transitions and phase boundaries. Nevertheless, the presence of graphene substrate creates a significant chemical gradient inside K-Se cathode intermediates and an imbalance in K concentration, which affects the site-specific energy of K atoms in the cathode and its stability [204].

4.3.2 Microstructural Analysis

Pristine graphene does not form any strong covalent bonds with active cathode due to its vdW slippery surface. Despite the non-reactive surface, graphene presence causes K concentration gradient in the active K_xSe cathode and possible variations in bond lengths along with cluster formations. We determined nearest neighboring distances between the atom pairs (Se-Se, Se-K, and K-K) in a-K_xSe cathodes by radial distribution function (RDF) analysis peaks (Figure 4.4). RDF (like PCF in Section 2.2) provides short-range and long-range structural information as the distances between the atomic pairs. Crystallinity is recognized by sharp singular distinct peaks in the plots, while broad peaks are characteristic of amorphous structure. RDF plots of a-K_2Se (x=2) and a-KSe (x=1) configurations in the graphene supported cases (Figures 4.4(a,d)) are compared with graphene-free cases (Figure 4.4(b, c, e, f)). The important peaks for neighboring distances between Se-Se, Se-K, K-K atomic pairs are listed in Table 4.1. RDF peaks for atomic pairs

in the amorphous cathode configurations (Figure 4.4(b,e)) are matched with RDF peaks of previously reported c-K_2Se and c-KSe crystals obtained from Materials Project database to identify any signs of short-range order [205].

In a-K_2Se without graphene (Figure 4.4(b)), a small peak at 2.5 Å indicates the presence of only a few Se-Se covalent bonds with the next neighboring distance between Se-Se starting from 4.9 Å. This does not match with c-K_2Se (Figure 4.4(c)), where no Se-Se covalent bonds are noted. In all a-K_2Se, the concentration of K is twice the Se and Se-K bonds are prominent observations with bond lengths of ~3.25Å and 3.35Å, respectively. While a broad red peak base at 2.9-3.4Å is noted for Se-K in a-K_2Se (Figure 4.4(b)), c-K_2Se (Figure 4.4(c)) has a very sharp crystalline peak. This difference clearly highlights the long-range amorphous characteristic of cathodes in the present study. K atoms form strong covalent bonds with Se and no K-K bond pairs are noticed in the atomic configurations of x=2 (K_2Se). The K-K values in Table 4.1 represent the neighboring distances and not bond lengths.

Graphene substrate-induced segregation of K at the interface in a-K_2Se/Gr does not impact the bond lengths in the structure but slightly reduces the neighboring distances causing a shift in peaks (Figure 4.4(a,d)). In Figure 4.4(a), a sharp black peak for Se-Se and reduced base of intense Se-K red peak at 3.2Å suggests a-K_2Se/Gr have some local atomic ordering much like c-K_2Se in Figure 4.4(c). Similar observations are made for the a-KSe configuration. Single-intense crystalline black peaks are noted for Se-Se at 2.5Å (Figure 4.4(d,e)), which match with crystal configuration (Figure 4.4(f)). Furthermore, the broad red peak at 3.2 Å in a-KSe (Figure 4.4(e)) disintegrates into multiple peaks in the presence of graphene (a-KSe/Gr in Figure 4.4(d)) resembling c-KSe (Figure 4.4(f)).

Overall, identical RDF peaks in graphene-supported amorphous cathode (Figures 4.4(a,d)) and their crystal counterparts (Figure 4.4(c,f)) suggest the presence of graphene-induced short-range crystallinity in otherwise disordered cathodes.

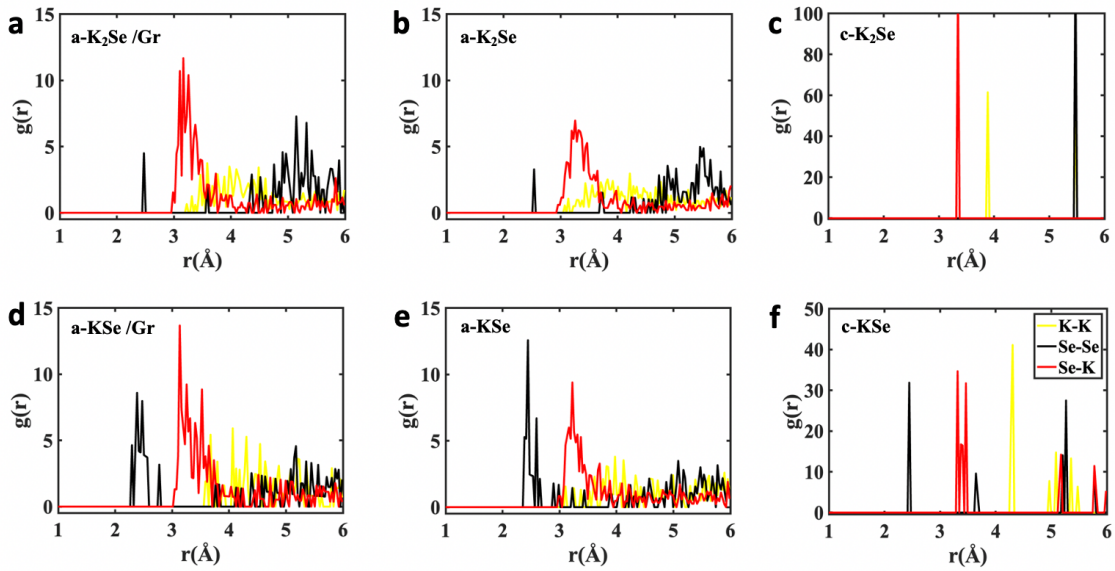

Figure 4.4 Radial distribution function (RDF) plots exhibiting nearest neighboring distances between atomic pairs in (a) a-K_2Se/Gr, (b) a-K_2Se, (c) c-K_2Se derived from Materials Project Database mp-8426, (d) a-KSe/Gr, (e) a-KSe, (f) c-KSe derived from Materials Project Database mp-9268. Distances between atomic pairs are plotted as Se-Se with black, Se-K with red and K-K with yellow.

Table 4.1 Nearest Neighboring Distances (Å) between Se-Se, Se-K and K-K in the K-Se Cathodes with and without Graphene Substrate

System	Se-Se	Se-K	K-K	Characteristic
a-K_2Se	2.5 Å, 4.9 Å, 5.5 Å	3.25 Å	>3 Å	Amorphous
a-K_2Se/Gr	2.4 Å, 4.4 Å, 5.2 Å	3.2 Å	>3.2Å	Amorphous
c-K_2Se	5.5 Å	3.35 Å	3.8 Å	Crystalline
a-KSe	2.5Å	3.2Å	>3.0Å	Amorphous
a-KSe/Gr	2.5 Å, 2.8 Å	3.2Å	>3.5Å	Amorphous
c-KSe	2.5Å, 3.7Å, 5.2Å	3.3Å, 3.5Å	4.3Å, 4.9Å, 5.4Å	Crystalline

One standalone difference between a-K_2Se (Figure 4.4(b)) and a-KSe (Figure 4.4(e)) configurations is the peak intensity at 2.5Å for Se-Se bonds. As earlier mentioned, a small peak at 2.5Å in a-K_2Se (x=2) indicates the presence of only a few Se-Se covalent bonds. This peak becomes very prominent in a-KSe (x=1) signifying Se-Se bonds are more profound. Two to three Se atom chains surrounded by K atoms are noticed in a-KSe/Gr (Figure 4.4(d)). These observations highlight the differences in Se-K clusters in a-K_2Se/Gr and a-KSe/Gr. In latter, the majority Se-Se bonds are intact, and interface contains potassium polyselenides with two to three Se atoms at the center surrounded by K atoms. At lower K concentration ($x < 1$ in K_xSe), Se chains become longer. Meanwhile, as K concentration increases, most Se-Se bonds break to accommodate K. The resulting interface contains Se-K clusters with one Se atom at the center bound by multiple K atoms. Inspired by these inferences, we analyzed the Se-K clusters at graphene interface in a-KSe/Gr and a-K_2Se/Gr to determine their adsorption energy $\boldsymbol{E_{ad}}$ over the graphene surface. Polyselenides in a-KSe (Figure 4.5(a)) are labeled as cluster-1 (Se-Se) and cluster-2 (Se-Se-Se). As earlier discussed, a-KSe/Gr was created after sequential depotassiation from a-K_2Se/Gr. Hence, Se-Se bonds in a-KSe/Gr are formed after K was removed (charging) and are not present due to the initial a-Se_{30} chain structure. There is a K saturation in a-K_2Se/Gr causing each Se atom to be surrounded by many K atoms (4 to 7). Typically, three Se-K clusters were present at the interface: Se_1K_5 labeled as cluster-3, Se_1K_6 labeled as cluster-4 and Se_1K_7 labeled as cluster-5 (Figure 4.5(b)). Only the Se atoms present near the graphene surface (bin ID 1) were bound to 6 or 7 K atoms, while Se in the central region (bin ID 2 and 3) were bound to 4 or 5 K atoms.

The surface adsorbed clusters were isolated from the bulk, and their adsorption energies ($\boldsymbol{E_{ad}}$) over graphene substrate were determined as follows

$$E_{ad} = E_{total} - E_{cluster} - E_{graphene} \quad (4.1)$$

Where $\boldsymbol{E_{total}}$ is the energy of cluster over graphene substrate determined by DFT, $\boldsymbol{E_{cluster}}$ and $\boldsymbol{E_{graphene}}$ are the energy of the isolated cluster and pristine graphene substrate. Negative $\boldsymbol{E_{ad}}$ denotes thermodynamically favored adsorption. We do not consider distinct translational or rotational configurations of Se-K clusters and limit our analysis to their existent orientation found in the parent bulk models (a-KSe/Gr and a-K_2Se/Gr). Stability of isolated clusters were realized from $\boldsymbol{E_{cluster}}$ values in the order cluster-2 > cluster-1 > cluster-3 > cluster-4 > cluster-5. Polyselenides (cluster-1 and 2) are naturally more stable than high-K clusters (cluster 4 and 5). Latter cannot exist independently outside the cathode bulk. Therefore, high-K clusters prefer to strongly bind to graphene surface with highest binding energies marked in red in Figure 4.5(c) (-3.137 eV for cluster-4 and -3.419 eV for cluster-5). The presence of more K atoms is one of the reasons for their strong binding with graphene.[203] Interaction strength of other three clusters (marked in blue in Figure 4.5(c)) with graphene is also reasonably high upon comparison with the literature [206]. These results strongly suggest that chances of shuttle effects in K_xSe/Gr cathode are highly reduced. Among interfacial clusters in a-KSe/Gr, cluster-2 (Se-Se-Se centered) is more stable and has stronger interaction with graphene substrate. This binding preference is a clear suggestion of controlled polyselenide dissolution in the presence of graphene. However, we observed an increase in binding energy with increase in Se content (Se-Se to

Se-Se-Se) suggesting that discharging may not be very favorable over graphene surface in low K cathode intermediates (with increased Se_n chains) [206, 207].

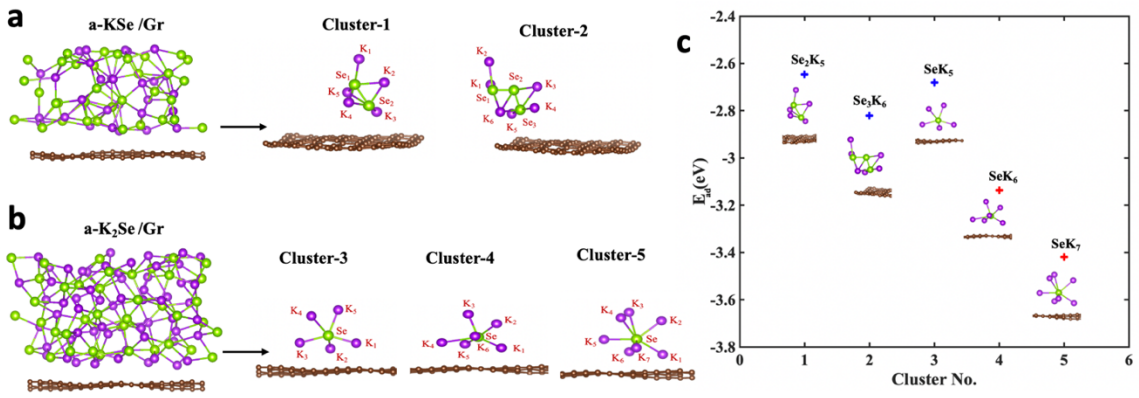

Figure 4.5 (a) Side view of relaxed a-KSe/Gr structure. Majority Se-Se bonds are intact, and interface contains potassium polyselenides with two to three Se atom chains at the center. These clusters are numbered as 1, 2. (b) Side view of relaxed a-K_2Se/Gr structure. Majority Se-Se bonds have broken to accommodate K and interface contains Se-K clusters with one Se atom at the center surrounded by K atoms. Clusters are numbered as 3,4 and 5. (c) Binding energies E_{ad} of different K-Se clusters noted at the interface with graphene substrate. E_{ad} of cluster 4 and 5 which are least stable in isolated state but bind strongly with graphene are marked in red.

4.3.3 Average Intercalation Potential

Operation of KIB is based on rocking-chair principle of LIBs, as K ions shuttle between anode and cathode through an electrolyte. To navigate this K ion shuttling, a chemical potential difference must exist between cathode ($\boldsymbol{\mu^{cathode}}$) and anode ($\boldsymbol{\mu^{anode}}$) which is referred to as open circuit voltage (***OCV***).

$$OCV = -\frac{\mu_K^{cathode} - \mu_K^{anode}}{zF} \tag{4.2}$$

Here, ***F*** is Faraday's constant, and z is the electronic charge transported by K in the electrolyte (z = 1 for K in non-conducting electrolyte). To theoretically calculate ***OCV*** for K_xSe cathode, K metal anode is considered with a constant chemical potential equivalent to K metal's Gibbs free energy (depicted in Figure 4.6(a)). Thus, electrical energy [117] gained in discharging between K_ySe and K_xSe (x > y) is given by difference in Gibbs free energy (***G***) of the two compounds as

$$E = -\left[G_{K_xSe} - G_{K_ySe} - (x-y)G_K\right] \tag{4.3}$$

$$E = -\Delta G \tag{4.4}$$

where G_K is the total Gibbs free energy of a single K atom in metallic K unit cell, and ***(x - y)*** represents K atoms intercalated in cathode during discharging. This leads us to calculate average intercalation voltage in cathode between two intercalation limits as

$$V = \frac{E}{(x-y)F} \tag{4.5}$$

Gibbs free energies calculated in our study are in electronvolts (eV). Therefore ***F*** is neglected in the above equation [208]. Average voltage profiles between final discharged cathode a-K_2Se and cathode intermediates (a-K_xSe with 0 <= x < 2) as a function of K content are shown in Figure 4.6(c). A sloping voltage curve in range 1.4 – 0.38 V (pink curve in Figure 4.6(c)) is the result of amorphous Se forming a solid solution with K in absence of any substrate. This voltage dip upon discharging is not a characteristic of a good cathode. Furthermore, capacity of pristine Se in KIB has been previously shown to drop to zero after first electrochemical cycle regardless of using carbonate-based electrolyte which

are best known to diminish shuttle effects caused by polyselenide formations [184]. Loss of active electrode to shuttle effects is a major drawback of using Se cathode in ion-based batteries, and high capacity potential of Se cathode can only be leveraged by combining Se with C-based matrix [209].

In comparison with porous C mesh, hexagonal C lattice-based matrix enclosing Se cathodes exhibit better performances for LIB [56, 199, 200, 210]. This is partially due to high conductivity of hexagonal C lattice and partly due to inability of Se to form covalent interactions with lattice surface that can cause loss of active Se electrode [202]. The blue plot in Figure 4.6(c) shows intercalation voltage profile of a-K_xSe cathode supported by hexagonal C lattice graphene. The discharge voltage for intercalation limit x = 0 and x = 2 is 1.55 V. Two high voltage peaks are noted at x = 0.8 and x=1.6. These peaks correspond to high energy structures ***ii*** and ***v***, as indicated in Figure 4.6(b). The energy of a-Se/Gr cathode dips during the process of discharging except near the intermediates ***ii*** and ***v*** where the sudden energy spikes are noted. These energy spikes are possibly due to several reasons. First, the rise in energy between intermediates ***i*** and ***ii*** is due to the stability of long Se chains on the graphene surface (Se-Se-Se vs Se-Se in Figure 4.5(c)) that causes an inconvenience in discharging. The increased binding energy between graphene and polyselenides with increased Se content (Se-Se to Se-Se-Se) could cause difficulty in Se chain breakage to store more K. Secondly, these two peaks in Figure 4.6(b) are similar to the earlier reports where electrode was recognized to constitute of two distinct phases [211, 212]. Based on this, we anticipate that these high energy structures are caused due to irregular distribution of small Se-K ordered phases indicated in the RDF analysis. The coordination analysis in a-K_xSe/Gr intermediates with Se-K bond length cutoff 3.35Å is

demonstrated in Figure 4.6(d). We see an unbalanced distribution of coordination polyhedron in ***ii*** and ***v*** in comparison to ***vi*** which is the final stable discharged product a-K_2Se/Gr.

From Figure 4.6(c), we can say that operating a-Se/Gr cathode at high voltage conditions (~2V) can lead to the formation of these cathode intermediates (***ii*** and ***v***) which represent thermodynamical energy barriers in the process of intercalation/deintercalation and could cause irreversible capacity losses. Moreover, parameters like K segregation at graphene interface and high binding energy of Se-K clusters (SeK_7 and SeK_6) with graphene can be factored into consideration for difficult K deintercalation in intermediate denoted as ***v*** ($K_{1.6}Se$).

If we observe the intercalation voltage profile in Figure 4.6(c) upon ignoring these thermodynamical barrier intermediates (dashed red plot), the voltage remains in 1.55 - 1.38 V range and exhibit a plateau-like profile. It is possible that K undergoes a single step reaction with Se to form K_2Se near 1.55 V much like in the case of Li-Se [213].

$$Se + 2K^+ + 2e^{-1} \rightarrow K_2Se \tag{4.6}$$

This single-step reaction between chain like Se_n cathode and K has also been reported for Se encapsulated in microporous C in an experimental study by Kang and coworkers [188]. In addition to this, the voltage range for the reaction is close to cathode voltage reported in a study with Se hosted by carbon nanotube anchored microporous C [185]. Our results feature strong dependence of electrochemistry on the graphene interface present in nanostructured electrodes

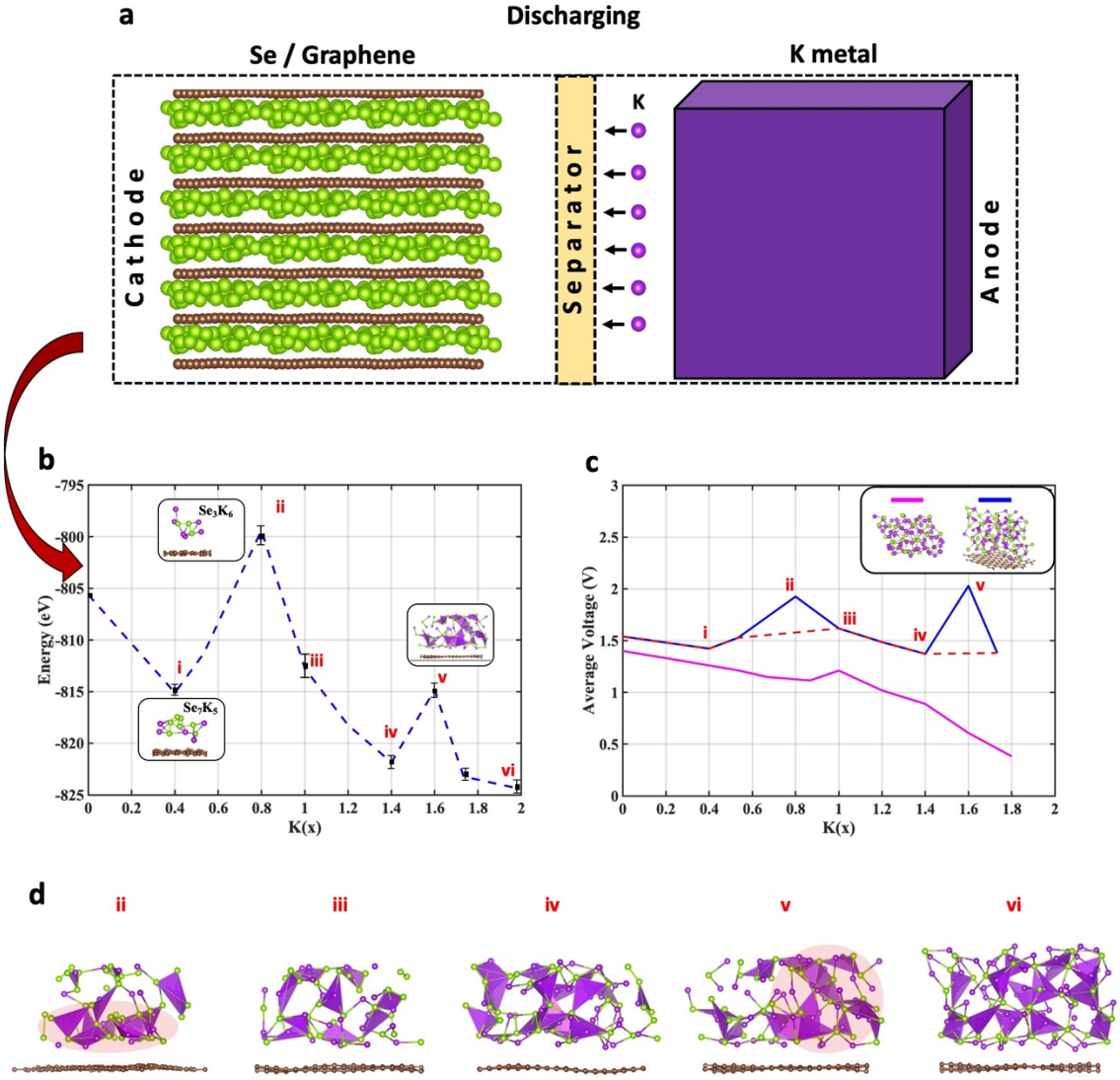

Figure 4.6 (a) Selenium-graphene heterostructure cathode half cell during discharging process in KIB. (b) Energy of relaxed graphene supported a-K_xSe cathode intermediates labelled *i* to *vi* including estimated error bars. Energies of relaxed cathode configurations are obtained by averaging energies of three to five structures obtained during AIMD simulation. Highest estimated errors were noted for intermediates *ii* and *iii* to be 2 eV. (c)Average discharge voltage of a-K_xSe cathode intermediates with K_2Se as final discharged product. The voltage profiles of Se-K alloying cathode with and without graphene substrate are plotted in blue and pink, respectively. (d) Se-K co-ordination analysis in reaction intermediates with Se-K bond length cutoff 3.35Å. The highlighted portions in intermediates labelled *ii* and *v* show irregular distribution of small Se-K ordered phases in otherwise disordered bulk.

4.4 Summary

In summary, we modeled graphene enclosed K_xSe cathode identical to experimentally designed electrodes and investigated the effect of graphene interface on K intercalation/deintercalation mechanism by AIMD and DFT. Our results suggest graphene substrate creates a substantial chemical gradient inside the K-Se cathode and nucleates small crystalline pockets in the otherwise disordered cathode bulk. Increased K density near interface causes the formation of Se-K clusters with a high K atom count (SeK_6, SeK_7). These clusters are not stable without substrate and interact strongly with graphene surface through binding energies (E_{ad}) as high as -3.137 eV for SeK_6 and -3.419 eV for SeK_7. These strong binding preferences between clusters and graphene are needed to avoid dissolution of selenides in electrolytes, but they can cause difficult deintercalation in several K_xSe intermediates. Moreover, the increase in binding energy with an increase in Se_n chain (E_{ad} = -2.646 eV for n=2 and E_{ad} = -2.82 eV for n=3) indicates that discharging is not favorable over graphene surface in low K cathode intermediates. These inferences appeared true when we calculated the intercalation voltage of K_xSe cathode intermediates with and without graphene support. We show that between K and Se cathode, there is a single step reaction near 1.55 V with K_2Se as discharged product. To avoid capacity losses due to difficult K intercalation/deintercalation, graphene-supported Se cathode should operate in the voltage range of 1.55V to 1.38V. High voltage can cause the formation of cathode intermediates with thermodynamically challenging K insertion and extraction.

CHAPTER 5

INTERFACE STRENGTH OF SILICON WITH SURFACE ENGINEERED MXENES

5.1 Introduction

2D transition metal carbides/nitrides (MXenes), which were discovered by Gogotsi and coworkers in 2011[61], have been recently mixed with Si anode by diverse synthetic procedures [63, 64, 214-216]. They hold the potential to have their surface engineered by modulating the functional groups (-OH, -O, and -F) by the choice of exfoliating agent during the synthesis process [217], and promise excellent performance as electrodes and supercapacitors for Li ion batteries [218-222]. Experimental reports have shown that Si/MXene composite excels in performance over its parent Si anode in capacity retention and cycle stability [64, 215, 216]. Conductive MXene functions as more than a binder in the electrode system by providing additional diffusive pathways, enhancing electron transport, and acting as a current collector [221, 223]. Above all, it is the stability of Si and MXene's interface, which is the foundation for the Si/MXenes system's aforementioned abilities. Interface adhesion of Si with substrate MXene needs to be critically tailored for optimum performance in batteries.

MXene surface terminations have a compelling role in altering the surface properties [224-226]. The impact of surface functional groups on MXene's performance in LIB battery systems has been studies by computational techniques. Diffusion studies of different ions in the interlayer spaces of functionalized MXenes have indicated that the OH and F groups tend to form clusters with Li and provide steric hindrance during the diffusion process [227]. In contrast, O-functionalized MXenes have manifested improved

electrochemical performance and larger LIB capacities[219]. Recently, some extrinsic functional groups were successfully incorporated on MXenes to enlarge the interlayer spaces for enhanced charge-discharge kinetics and improved energy storage[222, 228-230]. All attempts have been targeted to alleviate the role of MXenes as an electrode, with no attention being given to exploring characteristics of the functional group-driven interface of MXenes with Si.

As researchers advance towards utilizing surface terminations to influence electrode performance, it is necessity to establish their impact on the interface adhesion strength between MXene and the bulk material such as Si. First principle calculations have indicated a linear correlation between adsorption energies of single transition metal atoms on Ti_3C_2 and chemical attributes, such as charge distribution, bond length, and d-electron center of metal [231]. Interface adhesion analysis between an MXene and a 3D bulk go up to a recent experimentally measured value of 0.90 J/m^2 between SiO_2 and $Ti_3C_2T_x$ [232]. The study reports variation in interface adhesion between the two materials as atomic thickness of MXene monolayer is changed. In their experimental work, $Ti_3C_2T_x$ has higher adhesion with SiO_2 (0.9 J/m^2), which drops to 0.4 J/m^2 for Ti_2CT_x. By far, no focus has been laid on the specificity of MXene surface functional groups (T_x). In this chapter, the interface strength between 3D Si bulk and $Ti_3C_2T_x$ MXene with differing surface functionalities is investigated by the means of first principle calculations. This work has been published in *Physical Chemistry Chemical Physics* in 2021 as '*Variation in the Interface strength of silicon with surface engineered Ti_3C_2 MXenes'*.

5.2 Computational Details

Three $Ti_3C_2T_x$ MXenes with different surface functional groups (T_x) were modeled prior to the interface analysis. $Ti_3C_2T_x$ were derived from a stable and experimentally recognized atomic model of free-standing Ti_3C_2, where three Ti atomic layers are inter-cleaved with two C layers to result in five atomic thick Ti_3C_2 monolayer. Functional groups were attached to the surface under-coordinated Ti atoms, above the hollow site between three neighboring C atoms. Among all possible configurations of functional groups, this has been validated as thermodynamically most stable [233, 234]. The three $Ti_3C_2T_x$ configurations considered for the study are: ***(i)*** hydroxylated MXene $Ti_3C_2(OH)_2$, where surface is saturated with -OH functional group; ***(ii)*** mixed functionalized MXene $Ti_3C_2(OH/O)_2$, where ~38% surface -OH groups are randomly replaced by -O; and ***(iii)*** fluorinated MXene $Ti_3C_2F_2$, having -F as the only surface functional group. The three starting models were used for further analysis after complete optimization using DFT within VASP [142]. The top view of three MXene configurations can be seen in Figure 5.1.

Investigation of interface strength required surface energies of three MXene models, amorphous Si (*a*-Si) bulk, and the interface energy of *a*-Si/$Ti_3C_2T_x$ systems. Amorphous Si bulk having 64 Si atoms has been derived from a crystalline Si_{64} (Diamond FCC) using the computational quenching process [32]. Slabs of three MXenes and optimized *a*-Si were subjected to DFT relaxation with an added vacuum of 20 Å in z dimension to calculate the surface energies. It was critical for *a*-Si's free surface in the vacuum slab model to have the same surface area as its substrate MXene. Since the surface area of three Ti_3C_2 MXene models differs slightly due to different surface functionalization, we used three different vacuum models for *a*-Si surface energy calculation, each

corresponding to individual MXene configuration. For the interface models, three optimized MXenes were individually interfaced (as depicted in Figure 5.1) with a relaxed structure of *a*-Si bulk at an initial interfacial gap (***d***) of ~2.3Å. The interfacial gap *d* throughout the study is considered to be the vertical distance between lowest Si atom and top surface atoms of the MXene substrate. This consideration of initial *d* for the interface strength calculation is based on two assumptions. The distance of 2-2.5 Å between current two material surfaces should be ideal to encourage bonding. Moreover, as the interface's interaction is sensitive to an interfacial gap, huge variation in interfacial gap among the three interface systems might not provide us actual impact of the surface chemistry on the interface for comparison. Next, the interface energies were calculated using a vacuum interface model[126] with an added vacuum of 20 Å in z-dimensions (normal to the free surface) to permit complete ionic relaxation and circumvent periodic images' influence.

All optimizations were done using DFT within the VASP [142]. Projector-augmented-wave (PAW) potentials were used to mimic the inert core electrons, and valence electrons were represented by plane-wave basis set with the energy cutoff of 650 eV [143, 144]. Conjugate gradient method was employed for energy minimization with Hellmann-Feynman forces less than 0.02 eV/Å and convergence tolerance set at 1.0×10^{-6} eV. The GGA with the PBE exchange-correlation function was taken into account [119]. For all DFT calculations, gamma-centered 4 X 4 X 1 k-meshes were taken, and GGA functional was inclusive of vdW correction to incorporate the effect of weak long-range van der Waals (vdW) forces [171].

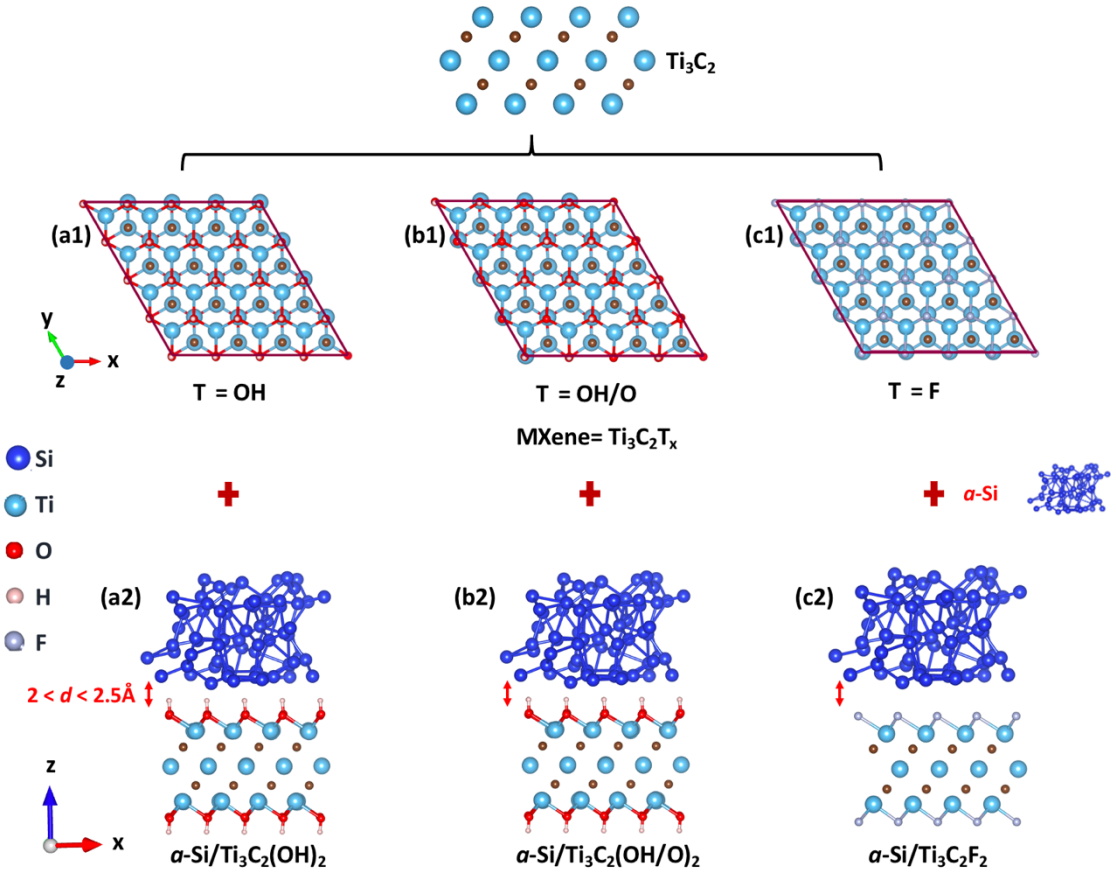

Figure 5.1 Atomic representation of three $Ti_3C_2T_x$ MXenes and their initial Si/MXene interfaces. (a1,b1,c1) Top view of surface functionalized $Ti_3C_2T_x$ MXene monolayers after DFT optimization. The surface functional groups (T_x) are changed from OH, to a combination surface of OH and O groups, and lastly, F. (a2,b2,c2) Side view of initial *a*-Si/MXene interface systems. The optimized MXenes are interfaced with a relaxed amorphous Si (*a*-Si) at an interfacial gap *d* ranging from 2-2.5 Å for the interface energy calculations. The interfacial gap *d* is the vertical distance between lowest Si atom and top surface atoms of the MXene substrate.

5.3 Results and Discussion

MXenes are derived from bulk MAX phases via chemical exfoliation using hydrogen fluoride (HF). During experimental synthesis, prominent surface terminations are -OH and -F depending upon aqueous HF concentration used in the exfoliation process. Post chemical treatment, MXene is dried to remove the excess water, which can sometimes lead

to cleaving of H from -OH surface terminations, resulting in H_2 release. This process leaves behind -O surface terminations. For the conversion of -OH termination to -O, additional energy of about 1.6 eV is required, and therefore, -O surface terminations are usually fewer in count [235, 236]. In most experimental synthesis, the MXene surface comprises of a mix of -OH, -O, and -F groups. Still, surface functional groups can be carefully tailored by optimizing HF concentration and drying temperature during synthesis procedures. These devised surface groups can drastically change MXenes surface properties and interfere in interface attributes. Thus, in the following sections, we discuss the influence of changing functional groups on the strength of the interface between Ti_3C_2 MXenes and *a*-Si.

5.3.1 Interface Strength Analysis

In order to obtain the interface strength of functionalized $Ti_3C_2T_x$ MXenes with Si, we created vacuum slab models for all three interface systems, as represented in Figure 5.2(a). Here, slab 1 consists of *a*-Si, slab 2 consists of functionalized $Ti_3C_2T_x$ MXene, and slab 3 has the interface system of *a*-Si over the respective MXene. These structures are periodic in x-y dimensions with a vacuum of 20 Å in z dimension. Final energy outputs from the DFT simulations of slab models are listed in Table 5.1 and were used to calculate work of separation ($\mathbf{W_{sep}}$) as per Equation (3.1).

Table 5.1 summarizes the slab energies E_1, E_2, E_{12} , and surface area A (x-y plane) for all the three interface systems post optimization. To draw out distinctiveness in the interfacial interaction between *a*-Si and $Ti_3C_2T_x$ as T_x is varied, it was important to maintain uniformity in the interfacial gap between *a*-Si and MXenes (*d*). During optimization of interface systems, Si atoms of amorphous bulk dispersed to their lowest

energy positions resulting in a variable interfacial gap *d* between MXene and *a*-Si. Yet, final *d* remained between 2- 2.5Å as briefed in Table 5.1.

The interface strength result via W_{sep} are presented in Figure 5.2(b) and explicitly show that interface strength between *a*-Si and $Ti_3C_2T_x$ MXene change as the functional groups on MXene surface (T_x) are altered. The interface strength of *a*-Si/$Ti_3C_2(OH)_2$ is calculated to be 0.606 J/m^2 in W_{sep} calculations. This presently derived interface strength is comparable in magnitude to the recent experimental results of $SiO_2/Ti_3C_2T_x$ (0.9 J/m^2) and SiO_2/Ti_2CT_x (0.4 J/m^2) interfaces [232]. However, surface chemistry's role on adhesion interactions at the interface becomes more prominent as variation in the interface strength is seen even with the slightest change of surface functional groups on MXenes. The value of W_{sep} dropped to 0.142 J/m^2 as fewer -OH groups are replaced by -O in the second interface system. Only 38% variation of the surface functional group (-OH to -O) significantly weakened the interface. With complete surface fluorination of Ti_3C_2, W_{sep} value further dropped to 0.115 J/m^2.

The interface strength of *a*-Si with $Ti_3C_2T_x$ MXenes is below 0.6 J/m^2, alike the interface strength results presented by Basu et al. [32] between *a*-Si and graphene (0.41 J/m^2) using the same methodology. This justifies why MXenes are increasingly being used along with Si in the battery systems. Interface adhesion of similar magnitude between active electrode particle and substrate benefits cycle life of a battery by mitigating stresses during lithiation/delithiation associated volume changes [32]. MXenes have proven to act as a promising substrate for active electrode particles such as Si by effectively accommodating volume expansions and imparting system with flexibility for the generation of flexible stable electronics[64, 216]. Low interface strength between the

system components is desired for liberal twisting and bending of MXenes, and to prevent brittle failures associated with strong interfacial bonding.

As much as we advocate low interfacial strength for the smooth long-lasting working of Si/MXene electrodes, we strongly recommend interfacial strength to remain above a threshold value to prevent complete loss of electronic contact between the two materials. Studies on the interface properties of 2D materials with 3D bulk are still in their infancy. Thus, quantitative determination of threshold value of interface adhesion for the continued electronic contact will require more detailed analysis with application-specific experimental validation. Since this lies beyond this study's purpose, we assume the negative values for W_{sep} will be universally derogatory for all the interface systems. Thermodynamically, interface strength is sensitive to the energy of interface system E_{12}. In Equation (3.1), W_{sep} depends on the difference between E_{12} and the sum of energies of the individual materials ($E_1 + E_2$). If E_{12} is lower than $E_1 + E_2$, both materials can come together to form a stable interface with a positive W_{sep}, as is the case for the three interface systems presented in Table 5.1. In contrast, the high system energy of the interface E_{12} indicates either lack of chemical interaction or the presence of interfacial strains due to local charge redistribution. Both these conditions are the ancillary outcome of interfacial gap *d*. If *d* between the two materials is too high, there is a possibility of a lack of chemical interaction. Conversely, if *d* is too low, atoms in the interface might be strained due to lattice misfit or stearic repulsions caused by the concentration of charges. Several earlier works on 2D material such as graphene [237, 238] throw light on the interface strength variation with the interfacial gap *d.* These computational studies summarize that the adhesion of 3D bulk materials on graphene substrate first increases and then decreases as

the two materials are brought closer. The similar relation has been realized between Si and MXenes in Appendix D.

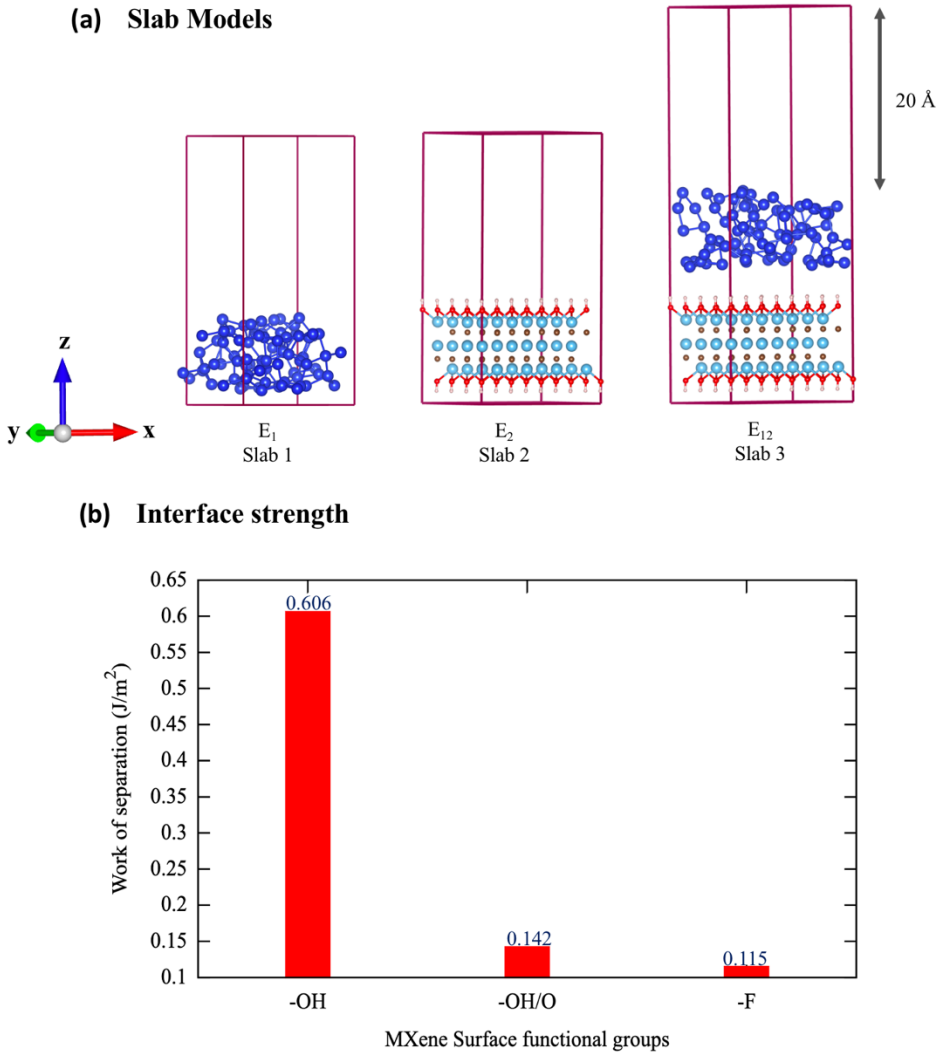

Figure 5.2 Vacuum slab model for energy calculations and interface strength results. (a)Representation of slab model used for the calculation of work of separation (W_{sep}) between *a*-Si bulk and MXenes. Slab 1 consists of amorphous Si, slab 2 consists of functionalized $Ti_3C_2T_x$ MXene monolayer, and slab 3 has interface system of *a*-Si over the respective MXene. (b) Interface strength between *a*-Si bulk and $Ti_3C_2T_x$ MXenes with changing surface functional groups (T_x), as calculated by W_{sep}.

Table 5.1 Final DFT Energies and Equilibrium Dimensions of *a*-Si/$Ti_3C_2T_x$ Interfaces

Functional Group	***d* (Å)**	**DFT optimized energy (eV)**			**Box Dimensions after optimization**		
		E_1	**E_2**	**E_{12}**	**x (Å)**	**y (Å)**	**Area ($Å^2$)**
T = OH	2.34	-223.515	-921.225	-1149.701	12.333	12.344	131.65
T = OH/O	2.26	-223.481	-887.087	-1111.724	12.293	12.297	130.60
T = F	2.14	-223.457	-724.417	-948.817	12.286	12.272	130.81

Note: For each interface system, $\mathbf{E_1}$ is energy of slab 1, $\mathbf{E_2}$ is energy of slab 2 , $\mathbf{E_{12}}$ is the total energy of interface system in slab 3, and **A** is the area of contact at the interface. Interfacial gap *d* is the vertical distance noted between lowest Si atom and top surface atoms of MXene substrate, in the optimized structure.

5.3.2 Electron Distribution Across the Interface

To comprehend the root cause of variation in the interface strength, a complete understanding of local charge redistribution across the interface is necessary as it depends critically on the material pair. Here, we throw more light on the electron redistribution at *a*-Si/ $Ti_3C_2T_x$ interfaces as the functional groups on MXenes are varied. For this, Bader charge analysis is performed on the optimized interface systems using scripts by Henkelman group [179]. Based on our used pseudopotential, Si atoms in the system have four valence electrons. Therefore, total electron transfer between the two materials (*a*-Si and $Ti_3C_2T_x$) is determined by summing electronic charges on all the Si atoms in the system. In all three interface systems, electrons were transferred from bulk *a*-Si to MXene (illustrated in Figure 5.3) and are mentioned in Table 5.2, where the net charge transfer across the interface is quantified as **Δq**.

The net electron exchange (Δq) at the interface is important for two reasons: first, it is symbolic of comparative ease of electronic interaction between the two surfaces; and second, it throws light on the existing bonding phenomenon. Charge transfer across the

interface systems increases as functional groups (T_x) change from -OH to -F in MXenes (Table 5.2, *i-iii*)**.** This quantitative evaluation could be explained by physicochemical property of work function, which is the energy required to remove an electron from the surface. Yu et al. [222] earlier reported the work function of the surface functionalized MXenes as follows: -OH terminated MXene has the lowest work function of 0.44 eV, while -O and -F terminated MXenes have high work functions (6.10 eV and 4.92 eV, respectively). Consequently, $Ti_3C_2(OH)_2$ surface will have the lowest electron affinity, which will increase proportionately to the change in surface functional groups (-O and -F). Moreover, O and F atoms are highly electronegative (EN) in comparison to Si atoms (EN_O = 3.44, EN_F = 3.98, and EN_{Si} = 1.90), and therefore, possess ability to withdraw more electrons from the latter. Thus herein, $Ti_3C_2(OH)_2$ acquire only 0.054 e^{-1} from Si bulk while $Ti_3C_2F_2$ acquired the highest e^{-1} count from the latter.

Conventionally, interface strength has a linear relationship with Δq, which impedes as the bonding distance increases [126, 180]. Therefore, we expected $\mathbf{W_{sep}}$ to have a linear relationship with **Δq** and $\mathbf{1/d^2}$, as emphasized by former Si-C interface study [126]. Conversely, for the case of Si-MXene interfaces, a downward trend is noted between the two quantities, as illustrated in Figure 5.3(d). Mere 0.054 e^{-1} are exchanged at the *a*-Si/ $Ti_3C_2(OH)_2$ interface, which has the highest interface strength among the three interface systems. On the contrary, highest Δq (2.32 e^{-1}) is noted for *a*-Si/ $Ti_3C_2F_2$ interface having the weakest interface strength. Thus, in the case of three *a*-Si/MXene interfaces considered, interface strength cannot be assessed correctly from the quantification of Δq alone. Evaluation of bonding phenomenon and stearic effects at the interface is imperative for a thorough understanding of interface strength.

Table 5.2 Summary of Net Electrons Exchanged (**Δq**) Across the Interfaces and Associated Interface Strength Values

S. no.	Functional Group	Interface strength (W_{sep})	Electrons exchanged (Δq)	*d*
(i)	T = OH	0.606 J/m^2	0.054 e^{-1}	2.34 Å
(ii)	T = OH/O	0.142 J/m^2	0.37 e^{-1}	2.26 Å
(iii)	T = F	0.115 J/m^2	2.32 e^{-1}	2.14 Å

Note: Interfacial gap *d* here is the distance between MXene and the lowest Si atom.

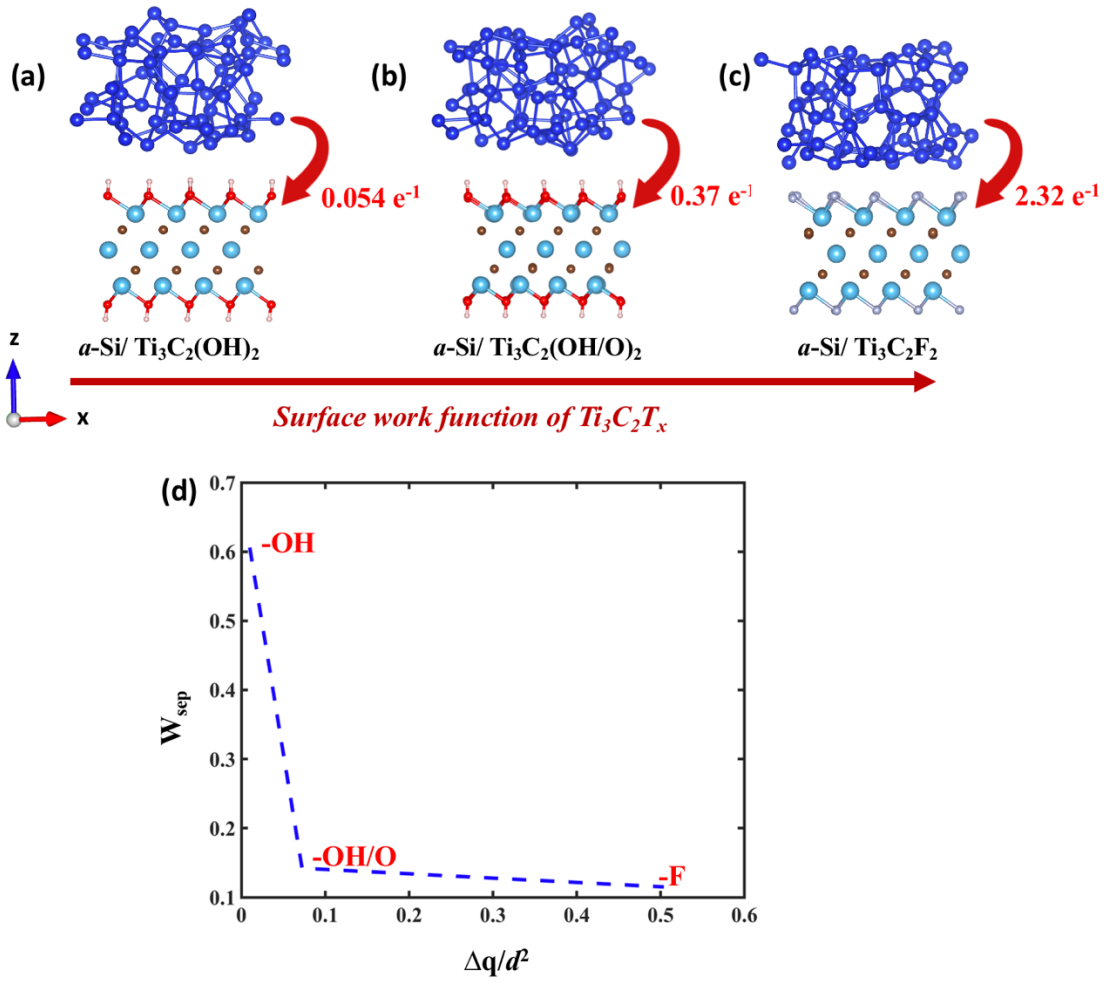

Figure 5.3 Relationship between interface strength, interfacial electron exchange and surface chemistry of Mxenes. (a,b,c) Atomic representation of *a*-Si/MXene interfaces depicting net charge transfer (Δq) from Si to MXene in three interface models having different surface functional groups (T_x). (d) Down trend between the calculated interface strength and the total electrons exchanged across the interfacial gap (q/d^2) at *a*-Si and MXene interface with different MXene substrates.

5.3.3 Charge Separation and Electron Distribution at the Interface

To understand the influence of surface functional groups on the charge redistribution at the atomic scale, we further zoom into atoms' charge distribution present at the interface. Charge density in the interfacial region of *a*-Si and $Ti_3C_2T_x$ MXenes is visualized by charge separation analysis and shown in Figure 5.4. Charge separation scheme at the interface was extracted by subtracting charge density of individual materials from that of the entire system, and the difference is plotted with an isosurface of 0.0007 e $Å^{-3}$. Accumulation and depletion of charges are depicted by red and green color in Figure 5.4. We have used this analysis to throw light on the influence of interfacial gap *d* on the electron distribution and charge density customized to the atom type present at the interface. Figure 5.5 focuses on the total electrons on individual atoms (denoted by $\boldsymbol{q}$, derived by Bader charge analysis) at the interface as the interfacial conditions change (*d* and T_x) within a system. The sum electrons on the surface atoms of MXenes at the Si interface and the free surface are also summarized in Table 5.3.

Loosely bounded Si atoms in *a*-Si bulk are distributed over MXene surfaces non-uniformly. While some surface Si atoms adsorb closely on the MXene surface, the majority are at a distance > 3Å, forming weak vdW interactions with the substrate. The charge separation scheme in Figure 5.4(a) indicates physisorption as the primary bonding mechanism in the system, which results in an intermittent amount of interface strength (0.60 J/m^2). This is also favored by the lack of atomic strains on the interfacial atoms. In Figure 5.4 (a) and (b), loss of electrons on the oxygen-bound hydrogen in OH groups causes polarity in the interfacial region. In the case of T= OH , highly electronegative O extracts electrons from H and Ti atoms. This leads to the existence of nearly free electron (NFE)

states parallel to the surface in the interfacial region with the highest positive charges. NFE states enable electron transmission in the interfacial channel without nuclear scattering [239-241]. This makes $Ti_3C_2(OH)_2$ an ideal substrate for Si electrode particles with facilitated electron transfer. Figure 5.5 (a1,a2) presents electron distribution on the interfacial atoms at *a*-Si/ $Ti_3C_2(OH)_2$ interface. Electron deprived H atoms can extract a small charge from a closely adsorbed Si atom (when d = 2.34 Å in Figure 5.5(a1)), in contrast to the high interfacial gap condition within the system when Si atom is present at the distance d > 3.2 Å from the MXene surface (Figure 5.5(a2)). In the latter condition, H and Si loose covalent contact, and no electron exchange occurs between the two. We note in Table 5.3, the surface H atoms in the interfacial region have a slightly higher sum of total electrons (15.2054 e^{-1}) than the H atoms present on the free surface with no intimate contact with Si (14.5529 e^{-1}). Hence, charge depletion on H atoms directs very little electrons from the Si at the interface.

Upon replacing a few -OH groups by -O on the surface of MXene, Si atoms are noted to move away from the surface -O groups and become more localized near -OH groups. Figure 5.4(b) depicts the red isosurfaces on Si atoms closer to MXene, predominantly in the region with -OH groups. There is hardly any Si atom within the bonding range of surface -O groups. These two conditions are further detailed in Figure 5.5 (b1,b2). The minimum distance between Si and surface O atoms in the current system is 3.2 Å, which is not positive for forming a covalent bond between Si and O. For the possibility of Si-O bond, bonding distance should be less than 1 Å (observed in Appendix D). Consequently, the surface -O groups tend to extract more electrons from Ti atoms to stabilize (Figure 5.5(b2)). As covalency between Ti-O increases, the ability of -O to bind

with Si decreases, resulting in a dip of interface strength between *a*-Si and $Ti_3C_2(OH/O)_2$. Weak vdW bonds between fewer surface -OH groups and Si atoms are the only contribution to the interface adhesion. We anticipate interface strength of such interfaces can be customized by varying the ratio of surface -OH and -O groups on MXenes. It is also noted from Table 5.3, the O atoms present in the interfacial region and on the free lower surface have barely any difference in the total electron count, further indicating the lack of interaction between surface -O and Si. Surface -O groups are free from Si adsorption and thus promise to enhance the electrode capacity by providing additional storage sites for Li/Na in Ion batteries [219].

At the interface of *a*-Si/ $Ti_3C_2F_2$, prominent charge density is seen around F atoms while the surrounding regions are deficient of charges (Figure 5.4(c)). The interfacial gap between the two materials is lower than the previous systems (d = 2.14 Å), and Si atoms are seen to be more uniformly present at the interface. When the interfacial gap d is as low as 2.2Å (Figure 5.5(c1)), higher electron exchange occurs between Si and F, committing to the high net electron exchange between the two materials (Table 5.2-*iii,* Δq=2.32 e^{-1}). These values indicate Si atoms are partially chemisorbed on the MXene surface. Interestingly, enhanced interaction between *a*-Si/ $Ti_3C_2F_2$ should indicate higher interface strength. However, due to close proximity of amorphous Si surface, there is a slight strain on F-Ti bonds due to steric hindrance. When d > 3Å in the same interface system (Figure 5.5(c2)), the covalent communication between Si and F is negligent, and Ti atoms become the primary donors to F. Similar to -OH group, F takes ~ $1e^{-1}$ from Ti atoms. Overall, the surface of -F terminated MXene becomes saturated with charges. As the consequence of high concentration of charges in the interfacial region, stearic effects between the two

materials reduce the interface strength. The interface strength of *a*-Si/$Ti_3C_2F_2$ improved significantly when the interfacial gap *d* was expanded to 3.28Å. The vdW forces hold the resultant interface with no atomic strains and W_{sep} = 0.335 J/m^2 as detailed in next section.

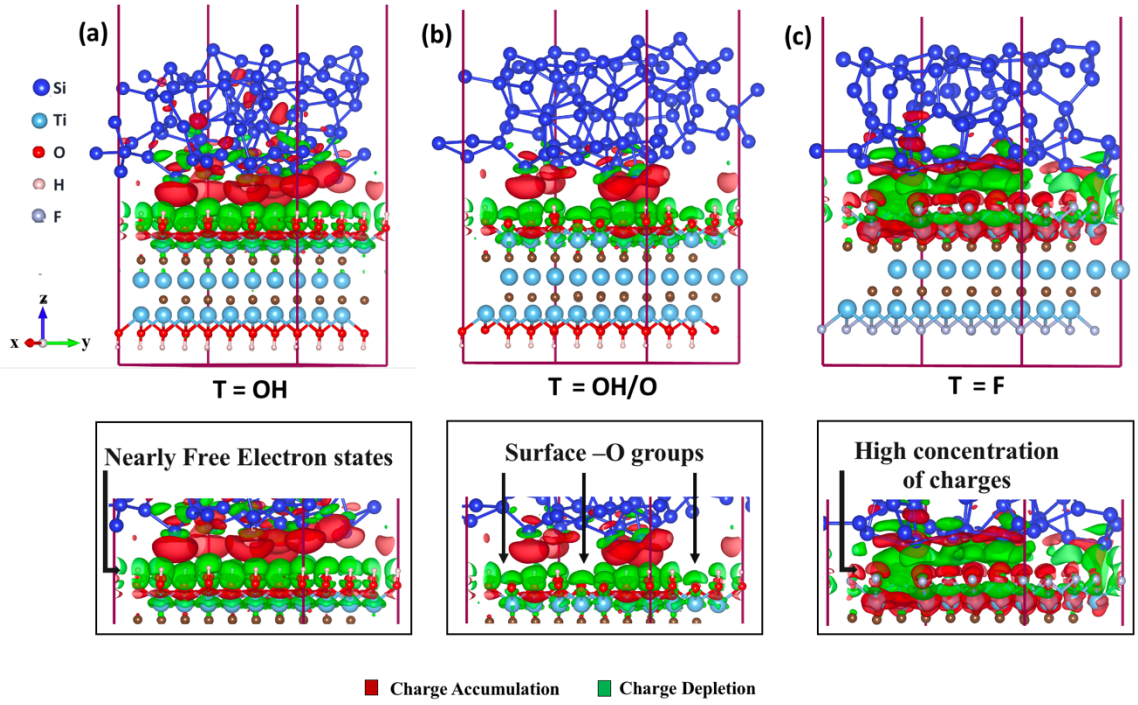

Figure 5.4 Charge separation scheme at *a*-Si/MXene interfaces. Charge separation scheme across (a) *a*-Si/ $Ti_3C_2(OH)_2$ interface, (b) *a*-Si/ $Ti_3C_2(OH/O)_2$ interface and (c) *a*-Si/ $Ti_3C_2F_2$ interface. Accumulation and depletion of charges are depicted by red and green color.

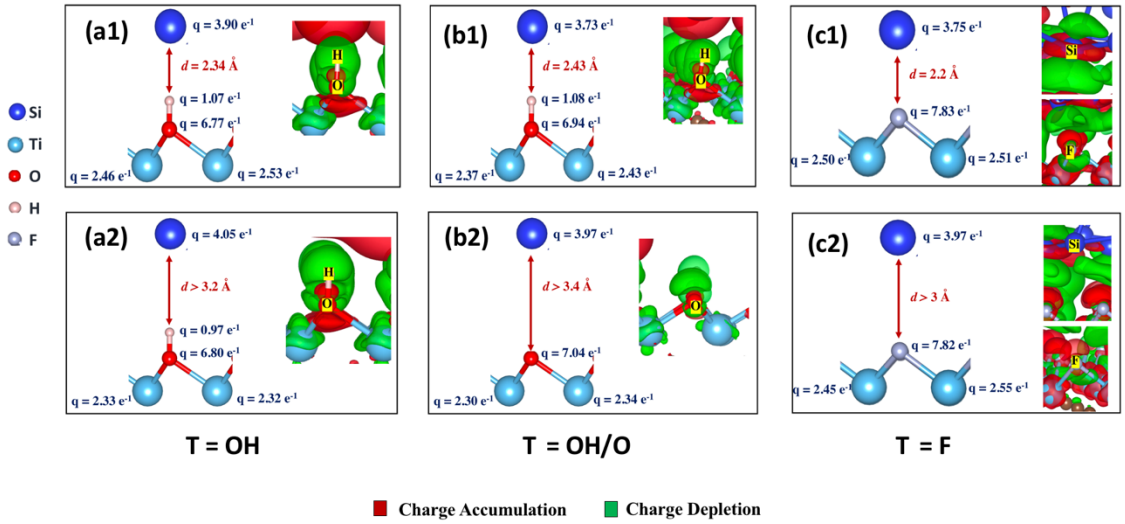

Figure 5.5 Electron distribution (q) on atoms as the interfacial conditions (d and T_x) change within a system. Electrons on interfacial atoms at a-Si/ $Ti_3C_2(OH)_2$ interface in regions with (a1) $d < 2.5$Å and (a2) $d > 3$Å. Electrons on interfacial atoms at a-Si/ $Ti_3C_2(OH/O)_2$ interface in regions with (b1) $d < 2.5$Å and -OH group, (b2) $d > 3$Å and surface -O group. Electrons on interfacial atoms at a-Si/ $Ti_3C_2F_2$ interface in regions with (c1) $d < 2.5$Å and (c2) $d > 3$Å. Figure insets depict accumulation and depletion of charges around respective atoms.

Table 5.3 Sum of Total Charges (q) on the MXene Surface Atoms at Both Surface

Functional Group	Surface atom	Total electrons on the surface atoms in interfacial region	Total electrons on the surface atoms on lower side
T = OH	H	15.2054 e^{-1}	14.5529 e^{-1}
T = OH/O	H	8.4297 e^{-1}	7.8734 e^{-1}
T = OH/O	O	111.4490 e^{-1}	111.1261 e^{-1}
T = F	F	125.4535 e^{-1}	124.53 e^{-1}

5.3.4 Modified Interface Strength of a-Si/ $Ti_3C_2F_2$ Interface

Interface system a-Si/ $Ti_3C_2F_2$ has the lowest interface strength (0.115 J/m^2) and highest interfacial net electron exchange (Δq) when the interfacial gap d is 2.14Å. This low

interface strength is primarily on account of high concentration of charges and strained Ti-F bonds in the interfacial region, as demonstrated in Figure 5.6 (a1-a3). The interface strength of *a*-Si/ $Ti_3C_2F_2$ improved significantly when the interfacial gap *d* was expanded to 3.28Å. The W_{sep} value is calculated to be 0.335 J/m^2. The electron exchange (Δq) at the interface (determined by bader charge analysis) is very low. It suggests that the resultant interface is held by very weak vdW forces, as shown in Figure 5.6 (b1-b3). The interface also appears to be free of atomic strains. Table 5.4 compares both the interface systems. Physisorption appears as a primary bonding mechanism in the second interface (Table 5.4, *ii*), similar to *a*-Si/ $Ti_3C_2(OH)_2$ interface. Yet, the *a*-Si/ $Ti_3C_2(OH)_2$ interface has the highest interface strength (0.606 J/m^2) in the present study. The analysis highlights the dependence of interface strength on the interfacial gap and bonding mechanism at two materials' interface.

Table 5.4 Comparison of *a*-Si/ $Ti_3C_2F_2$ Interface Strength with Varied Interfacial Gap

S. no.	Functional Group	Interface strength (W_{sep})	Electrons exchanged (Δq)	*d*
(i)	T = F	0.115 J/m^2	2.32 e^{-1}	2.14Å
(ii)	T = F	0.335 J/m^2	0.38 e^{-1}	3.28 Å

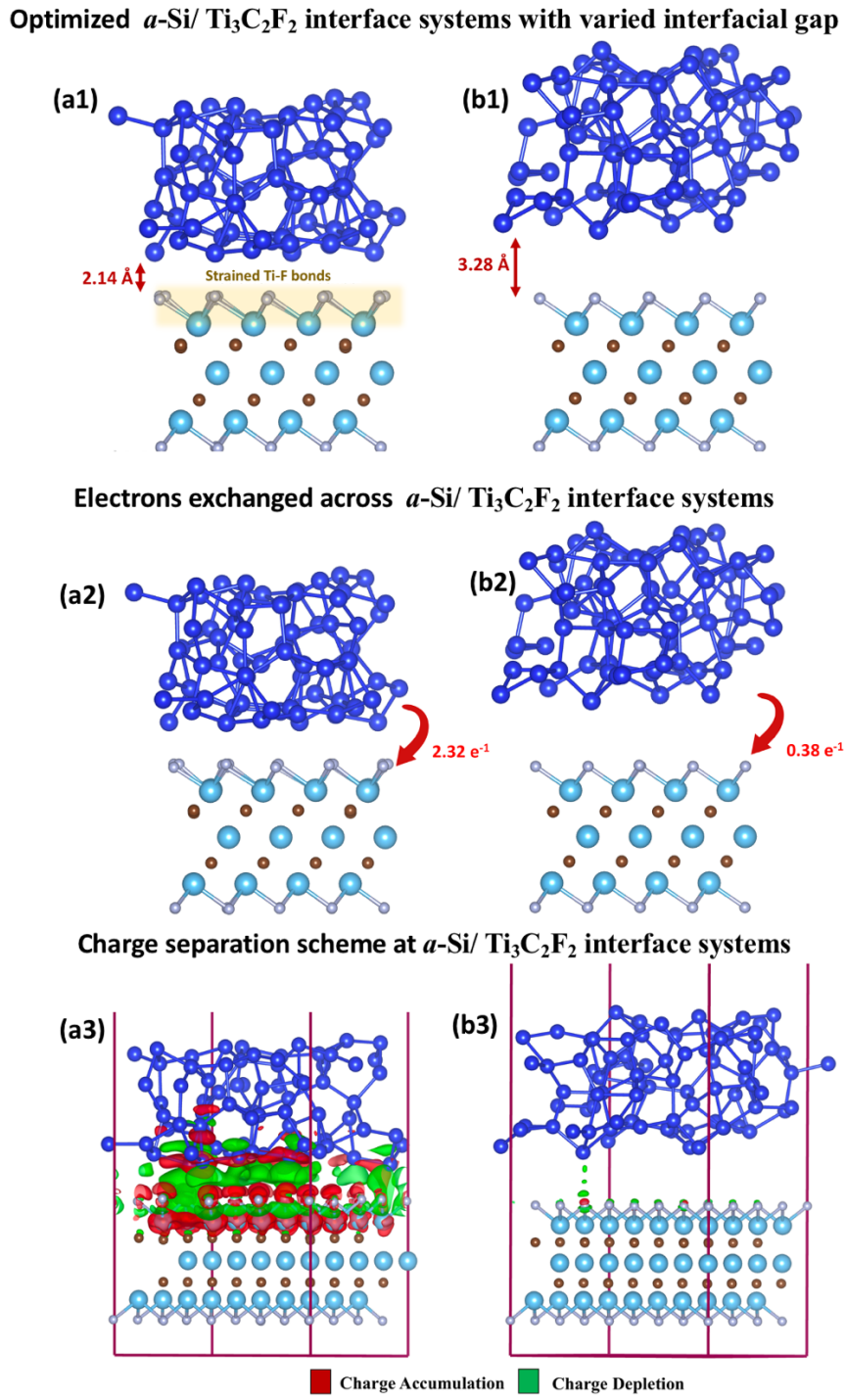

Figure 5.6 Comparison of *a*-Si/ $Ti_3C_2F_2$ interface systems with varied interfacial gap d. (a1-b1) Atomic representation of optimized *a*-Si/ $Ti_3C_2F_2$ interface systems with interfacial gap 2.14 Å and 3.28Å. (a2-b2) Atomic representation of *a*-Si/ $Ti_3C_2F_2$ systems depicting net electron transfer across the interface. (a3-b3) Charge separation scheme across the *a*-Si/ $Ti_3C_2F_2$ interface systems with red depicting charge accumulation and green representing charge depletion.

5.4 Summary

In summary, we have carried out DFT calculations to quantify the variation in interface strength between 3D amorphous Si bulk and surface terminated $Ti_3C_2T_x$ MXenes. Our results show that -OH functionalized MXene binds most strongly to amorphous Si with work of separation of 0.606 J/m^2 in comparison to -OH/O mixed and -F functionalized MXenes. These values of interface adhesion ranged from intermittent to low and are favorable for battery applications to permit easy expansion/contraction. Next, the overall net electron exchange at the interface has little to say about the interface strength. The interface strength noted for the three interface systems is not linear to charge transferred across the interface as per the popular observation. Electron distribution across the interface is driven by physico-chemical surface properties such as work function and electronegativity of the functional groups. Detailed analyses of interfacial gap and bonding mechanism reveal that physisorbed interfaces have better interface strength, as noted for *a*-Si/ $Ti_3C_2(OH)_2$ and *a*-Si/ $Ti_3C_2F_2$. The presence of a high concentration of charges in the interfacial region of partially chemisorbed materials resulted in steric effects. It was ultimately responsible for low interface strength, as in the case of -F terminated $Ti_3C_2T_x$ MXene and Si. Our results provide more in-depth insight into the atomic-level interfacial phenomena of surface terminated MXene with Si.

CHAPTER 6

ENERGY PREDICTION OF INTERFACES WITH DEEP LEARNING

6.1 Introduction

Computational modeling of interfaces remains less explored due to high computational cost involved in ab initio methods such as density functional theory (DFT) and lack of accurate empirical force fields for molecular dynamics (MD) simulations. Recent years have seen emergence of machine learning (ML) based potential energy surface (PES) that can describe complex systems at low computational cost, with close to first principles accuracy. These methods rely on large amount of DFT data (structures, energies, and forces) to efficiently explore chemical space with respect to the target properties during training. Considering extensive usage of graphene 2D/3D heterostructures in energy storage systems, deficient computational studies on such interfaces are noted in literature due to lack of accurate empirical force fields. The standard DFT analysis of these multiphasic-multicomponent systems which include possibility of variety of surface imperfections is computationally too expensive (see Table 6.1).

Table 6.1 Computation Details of DFT of Graphene Based Interfaces using XSEDE CPU

Interface	Total time with 72 CPU cores
c-Se/Gr	406.33 hrs
a-Se/Gr	843.3 hrs

In development of ML-based PES, structures are represented by appropriate descriptors and fed to neural network(NN) algorithms to generate PES that are invariant to translational, rotational, and permutation of homonuclear atoms [242, 243]. These PES are independent of any physical parameters and approximations unlike empirical force fields. Hence PES are more accurate if atomic local environments are well described by descriptors. Several ML techniques have been employed for PES development: linear regression [244, 245], gaussian approximation [246, 247], high-dimensional neural networks (HDNN)[248] and graph neural networks(GNN)[249, 250]. Of particular interest are HDNN using atom-centered symmetry functions(ACSF) as input descriptors [242] that have been successful for a wide range of materials due to their generality [251-254].

In this chapter, we first elaborate primary concepts in ML and HDNN methods devised by Behler and Parrinello [248]. Next, we discuss our attempts on developing accurate ML-based PES for graphene-based 2D/3D interface systems that can be extrapolated and transferable to configurations outside training dataset. ML-based PES are developed for a model interface system of 3D Tin (Sn) bulk over 2D graphene.

6.2 Introduction to Deep Learning

While the chapter title indicates Deep Learning of interfaces, we have only yet mentioned Machine Learning. This section differentiates the two components, namely machine learning and deep learning. Both these techniques fall under the broader umbrella of Artificial Intelligence (AI), as shown in Figure 6.1. Artificial Intelligence term was first coined in 1956 and has gained wide popularity ever since due to its ability to make it possible for machines to learn from input data, recognize pattern in them and provide

output accordingly. In this analogy, input data can be considered as the learning experience. Machine Learning (ML) is a subset of AI which utilizes statistical methods to efficiently learn large dataset. Meanwhile, Deep Learning (DL) is no different from ML, except here nested hierarchal neural networks are utilized to learn patterns in complex data, much like brain neurons.

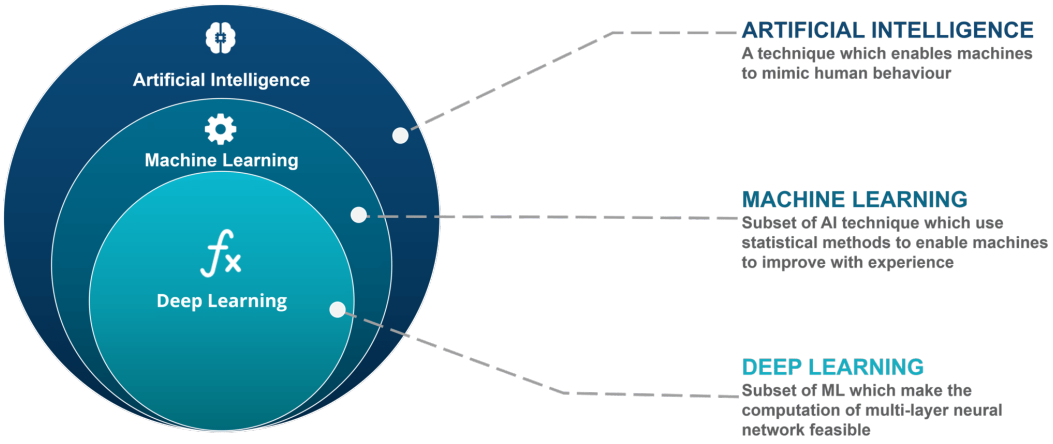

Figure 6.1 Description and scope of Artificial Intelligence, Machine Learning and Deep Learning.
Source: https://www.edureka.co/blog/ai-vs-machine-learning-vs-deep-learning/, retrieved on September 22, 2021.

6.3 Behler and Parrinello Methodology

6.3.1 Feed Forward Neural Networks (NN)

Biologically inspired, feed forward neural networks (NN) are mathematical algorithms for representation of arbitrary functions. NN typically consists of node layers, which contain an input layer, one or more hidden layers, and an output layer (depicted in Figure 6.2). Each node is a computational representation of brain neurons and is connected to the nodes

of next layer with weights (***w***). Thus, each node in NN gets its input from the previous layer. The result is shifted by a bias weight(***b***) and then adjusted by an activation function(***f***) to permit non-linear fitting of the function. During the training process, parameters of NN (*w, b, f, nodes*) are iteratively optimized such that input data is reproduced. Once trained, NN function is then used to evaluate another data. Mathematical expression for a NN with 2 hidden layers and one output layer is represented by Equation (6.1).

$$E = f_a^3\left[b_{01}^3 + \sum_{j=1}^{4} w_{j1}^3 f_a^2\left(b_{0j}^2 + \sum_{u=1}^{5} w_{uj}^2 f_a^1\left(b_{0u}^1 + \sum_{k=1}^{4} w_{uk}^1 G_i\right)\right)\right] \quad \textbf{(6.1)}$$

In order to represent PES, DFT calculations are generally used to provide the training data (structures and energies). Once trained, NN can predict energy of a structure from atomic coordinates analytically [248]. However, NN have found success for only small atomic systems and encounter issue of limited degrees of freedom (nodes) when seeking application in condensed phase material systems [242].

Limitations of NN in modeling materials:

- For systems with a larger number of atoms, the size of NN (nodes) increases accordingly, making it less efficient.
- Once trained, the size of NN is fixed. Therefore, it is only applicable to a system of fixed number of atoms.
- Invariance of final output cannot be achieved. Invariance is the ability of algorithm to output system energy despite exchange of positions of two similar atoms within the structure.

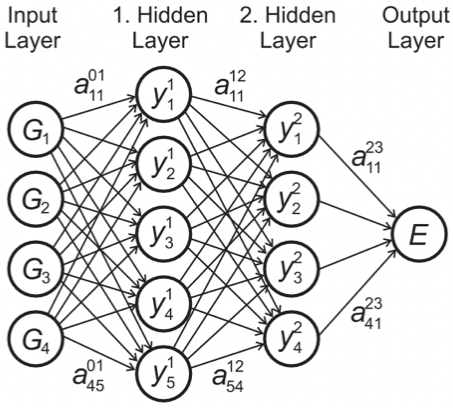

Figure 6.2 Structure of feed forward neural network having one input layer, two hidden layers, and one output layer.
Source: [242]

Therefore, utility of NN in materials is limited and led to the introduction of high dimensional neural networks (HDNN) by Behler and Parrinello [248], as described in next section.

6.3.2 High Dimensional Neural Networks (HDNN)

The complex problem of predicting energy of large atomic systems using deep learning is simplified by disseminating the total energy of the system ($\mathbf{E_{total}}$ in Equation (6.2) and $\mathbf{E_s}$ in Figure 6.4) with N atoms into the atomic energy contributions ($\mathbf{E_i}$) based on the local chemical environment of each atom as

$$E_{total} = \sum_{i=1}^{N} E_i \tag{6.2}$$

Here, chemical environment of each atom within a specific cutoff radius ($\mathbf{R_c}$) is defined by certain functional that depicts the structural information of neighboring atoms of the central atom shown in Figure 6.3. The model learns to assign atomic energies to individual atoms based on the set of reference energies (derived from DFT). Since electronic simulations such as DFT do not provide actual energy per atom, energy per atom is deduced by dividing total energy with the number of atoms.

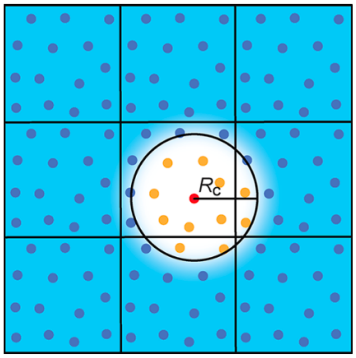

Figure 6.3 Environment of each atom within cutoff radius (R_c) described as a fingerprint function called descriptor rather than cartesian coordinates.
Source: [255]

Schematic in Figure 6.4 shows a high dimensional neural network (HDNN) that constitute a number of NN referred to as atomic NN, each contributing atomic energy to the total energy. These atomic NNs are fed symmetry function (SF) vectors that describe chemical space of each atom. Thus, workflow is as follows: Cartesian coordinates ($\mathbf{R_i}$) of all atoms are converted to a set of inputs suitable for NNs. These inputs are called symmetry functions ($\mathbf{G_i}$). G_i are then used as input features for each atomic NN, which has atomic energy for its output. All the atomic energy contributions are ultimately added to obtain

the total energy of the system. The most crucial step in this workflow is the conversion of cartesian coordinates to SF which is described in detail in the next section.

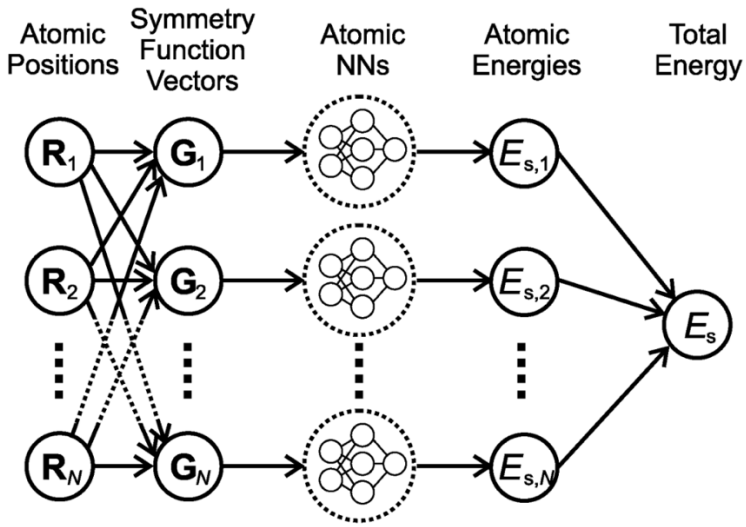

Figure 6.4 Structure of high dimensional neural network based on decomposition of total energy into atomic energies outputted by atomic NNs [242].

6.3.3 Atom-Centered Symmetry Functions (ACSF or SF)

There have been several attempts to use cartesian coordinates as structural inputs for ML-based PES [256, 257], but it has been recognized as not a good choice. Cartesian co-ordinates are not independent of molecular translation and rotation. Since NN are mathematical fitting methods, the output is sensitive to absolute values of input features. To overcome these limitations in describing complex chemical structures to NNs, Behler and Parrinello [248] introduced Atom-centered symmetry functions (ACSF) that describe the chemical neighborhood of each atom with the help of radial and angular symmetry functions. There are two types of ACSF commonly used that define radial($\mathbf{G^2}$) and

angular($\mathbf{G^4}$) information of neighboring atoms within the cutoff radius ($\mathbf{R_c}$). The cutoff function for all the neighboring atoms within $\mathbf{R_c}$ is defined as

$$f_c(R_{ij}) = 0.5 \times \left[\cos\left(\frac{\pi R_{ij}}{R_c}\right) + 1\right] \tag{6.3}$$

Where $\mathbf{R_{ij}}$ is the distance between central atom ***i*** and its neighboring atom ***j***. $\boldsymbol{f_c(R_{ij})}$ is a continuous and differentiable function whose value turns 0 when $R_{ij} > R_c$. The radial and angular SF for central atom *i* are defined with the help of cutoff function as two body and three body sums.

$$G_i^2 = \sum_j e^{-\eta\left(R_{ij}-R_s\right)^2} . f_c\left(R_{ij}\right) \tag{6.4}$$

$$G_i^4 = 2^{1-\zeta} \sum_{j,k\neq i}^{all} \left(1 + \lambda\cos\theta_{ijk}\right)^{\zeta} . e^{-\eta\left(R_{ij}^2+R_{ik}^2+R_{jk}^2\right)} . f_c\left(R_{ij}\right). f_c(R_{ik}). f_c\left(R_{jk}\right) \tag{6.5}$$

Here, $\mathbf{G_i^2}$ is a sum of Gaussians multiplied by cutoff function, where the width of the Gaussian and the center of the Gaussian can be defined by parameters $\boldsymbol{\eta}$ and $\mathbf{R_s}$. A non-zero R_s value can shift the center of Gaussian away from reference atom, therefore, it is preferably set to 0. The parameter $\boldsymbol{\eta}$ is a Gaussian exponent responsible for indicating reduced interaction strength with increasing distance between the two atoms (Figure 6.5(a)). Parameters $\boldsymbol{\zeta}$ and $\boldsymbol{\lambda}$ in the function $\mathbf{G_i^4}$ controls the angular resolution and cosine

function, respectively. λ usually takes value either +1 or -1 for inverting the cosine function maxima from $\theta_{ijk} = 0°$ to $\theta_{ijk} = 180°$ [242]. The most preferred value for ζ is 1 as it provides sufficient coverage centered at 0° (when λ = 1). Higher values can increase angular resolution close to the center at the cost of reduced coverage, as shown in Figure 6.5(b) [258]. Multiple SF set for each type need to be used to cover different portions of chemical environment. Values of these parameters define the high dimensional input vector representing the local environment of each atom in the material system. It is advisable that 100-150 $\mathbf{G_i}$ be used for bicomponent system such as interface systems in the present work.

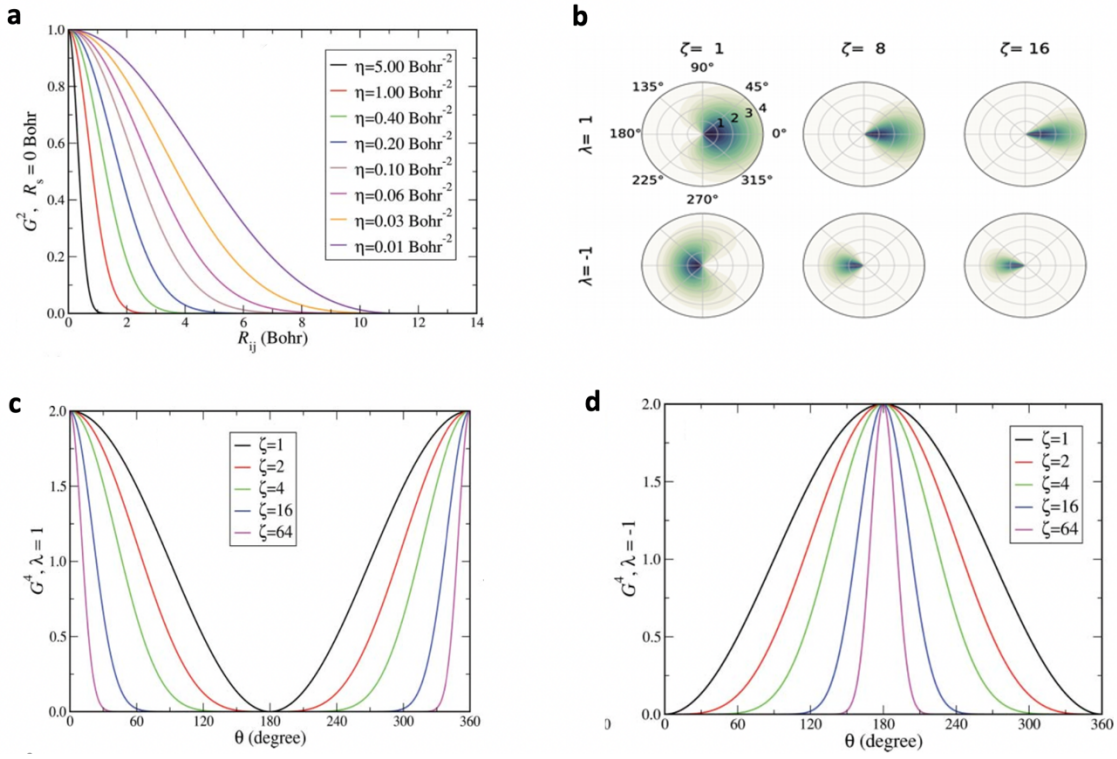

Figure 6.5 (a) G_i^2 with variable width of the Gaussian defined by parameters η and R_s = 0. (b) Angular resolution by parameters ζ and λ in the function G_i^4. Angular contributions of ACSF with variable ζ are demonstrated in (c) for λ = 1 and (d) λ = -1.
Source: [242]

6.4 Computational Details

A complete summary of workflow has been presented in Figure 6.6 and each step will be detailed in the following sub-sections. Sn is known for its several allotropes. Two prominent Sn allotropes used in training data are alpha (α-Sn) and beta (β-Sn). Unequilibrated Sn and Gr interface structures are DFT optimized. The training dataset consists of five Gr|Sn interface structures: crystalline α-$Sn_{(32,64)}$, β-$Sn_{(12,16)}$, and amorphous Sn_{64} interfaced with Gr where amorphous Sn_{64} phase is obtained with the process of computational quenching of α-Sn_{64}.

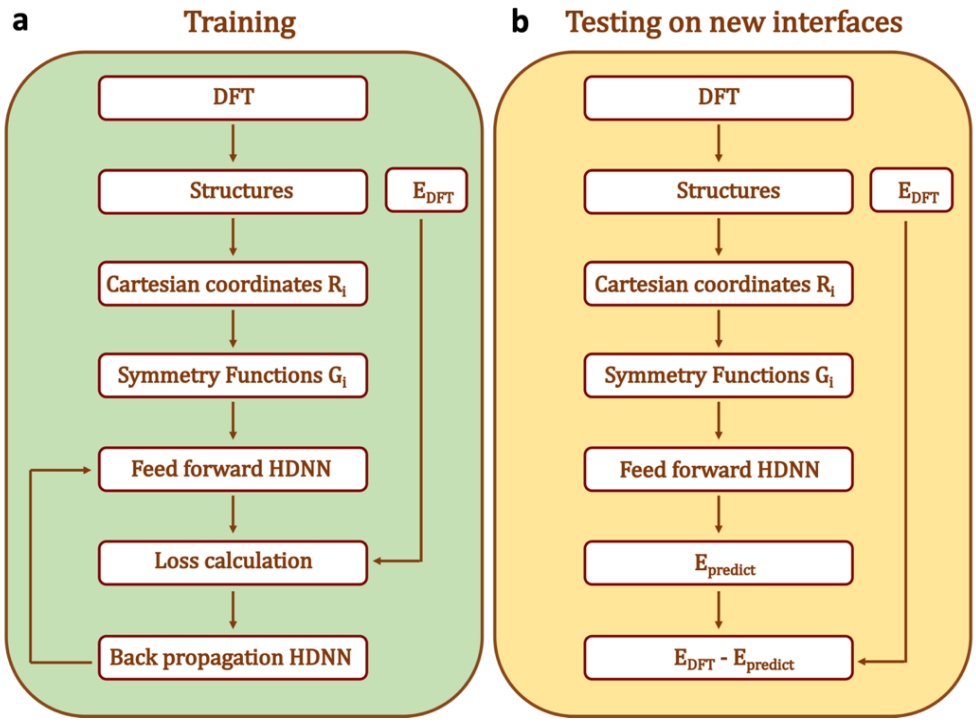

Figure 6.6 Steps in construction and testing of machine learning potentials for Gr|Sn interface structures.

6.4.1 DFT Calculations

Coherent interface models were created between ordered single layer Gr and Sn allotropes with an optimum interfacial gap of 3.5 Å. Gr contains 60 sp^2 hybridized carbon atoms in all the interface structures and size of Sn bulk varies from atom size of 12 to 64. The interfaces are set in periodic x-y plane and across Sn (100) miller indices. These interface structures were modeled with a vacuum of 15Å in z dimensions to circumvent the periodic influences, and then DFT optimized to obtained relaxed strain-free interface configurations. All crystalline Sn bulks were derived from materials project database[205], while amorphous Sn was created with computational quenching of α-Sn_{64} by heating it to 2000 K followed by rapid cooling. All materials were DFT optimized individually before interfacing them. All DFT calculations in the study are done using VASP [142]. Projector-augmented-wave (PAW) potentials are used to mimic inert core electrons, while the valence electrons are represented by plane-wave basis set [143, 144]. Plane wave energy cut-off and convergence tolerance for all relaxations are 550 eV and 10^{-6} eV, respectively. The GGA with the PBE exchange-correlation function are taken into account [119] with inclusivity of vdW correction to incorporate the effect of weak long-range van der Waals (vdW) forces [171]. The energy minimizations are done by conjugate gradient method with Hellmann-Feynman forces less than 0.02 eV/Å. Considering the vacuum slab structure of all interfaces, gamma centered k-meshes 4 X 4 X 1 are used for good convergence.

6.4.2 Training Data and Testing Data

A training dataset is built from convergence iterations of DFT simulations which covered the trajectory of minima search for interface structures starting from the initial non-

equilibrated structure as shown in Figure 6.7 for Gr|α-Sn_{64}. This scheme ensured that non-equilibrated and intermittent structures were as much part of learning process as the relaxed structures. Training dataset contains intermediate DFT iterations of five Gr|Sn interface structures, as mentioned earlier. These interface structures accounted for total of 5789 structures with their reference energies for the training dataset.

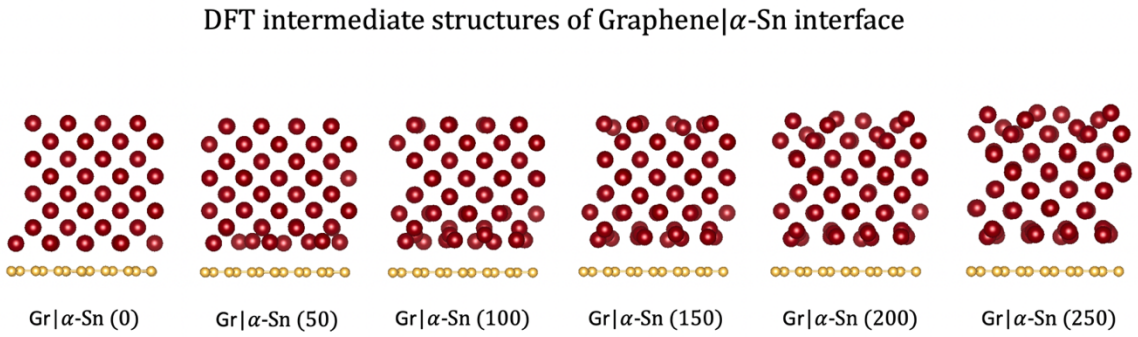

Figure 6.7 Intermediate Graphene|α-Sn_{64} interface structures between initial and equilibrium interface configurations. Structural configuration in first 250 DFT iterations are presented depicting quick structural transformations in early DFT stages. Simulation took approximately 1100 iterations to completely optimize. No major structural rearrangements were noted in the later iterations.

Trained model weights are used to predict energies of alien Gr|Sn interface systems and compared with their respective DFT energies. To access the performance of our model and test transferability of PES in a sequential order of unfamiliarity, we use four carefully contemplated test interface structures. The first test structure (T1) is the very Gr|β-Sn_{12} interface used in training datasets, except that here the orientation of Sn bulk is slightly shifted over Gr surface. It is an example of known interface structure, unknown orientation. The second test structure (T2) is again a familiar interface with increased Sn bulk size

($Gr|\beta\text{-}Sn_{16} \rightarrow Gr|\beta\text{-}Sn_{32}$). The objective of T2 is to test the system size extrapolation capabilities of the PES.

In contrast to T1 and T2, third test structure (T3) is completely unfamiliar interface. A new Sn bulk (mp-949028) is interfaced with Gr. The fourth and final test interface (T4) is derived from T3 by creating divacancy defects in the interfacing Gr. This change adds complexities of defects, adsorption, and diffusion at the interface, which are not noted in the earlier test interfaces. Differences in test structures from the training dataset are summarized in Table 6.2. The initial test interface structures were created like reference interfaces and subjected to DFT optimizations. Since current machine learning scheme does not include automated equilibration, the ability of PES to predict energies of intermediate configurations as structures search for global minima is assessed by testing on the DFT intermediates of test interfaces between initial and final configurations. The variations in the test interfaces during DFT optimization can be noted in the iteration snapshots presented in Figure 6.8. While minimal Sn alignment changes are observed in initial - final T2 and T3 structures, major phase transformative and surface defects are seen in T1 and T4, respectively.

Table 6.2 Notable Differences in Test Structures from Training Dataset

Notable features of test structures	**T1**	**T2**	**T3**	**T4**
Familiar interface	O	O	×	×
Familiar interface orientation	×	O	×	×
Similar Sn bulk size	O	×	×	×
Familiar Sn allotrope bulk	O	O	×	×
Familiar Gr substrate	O	O	O	×

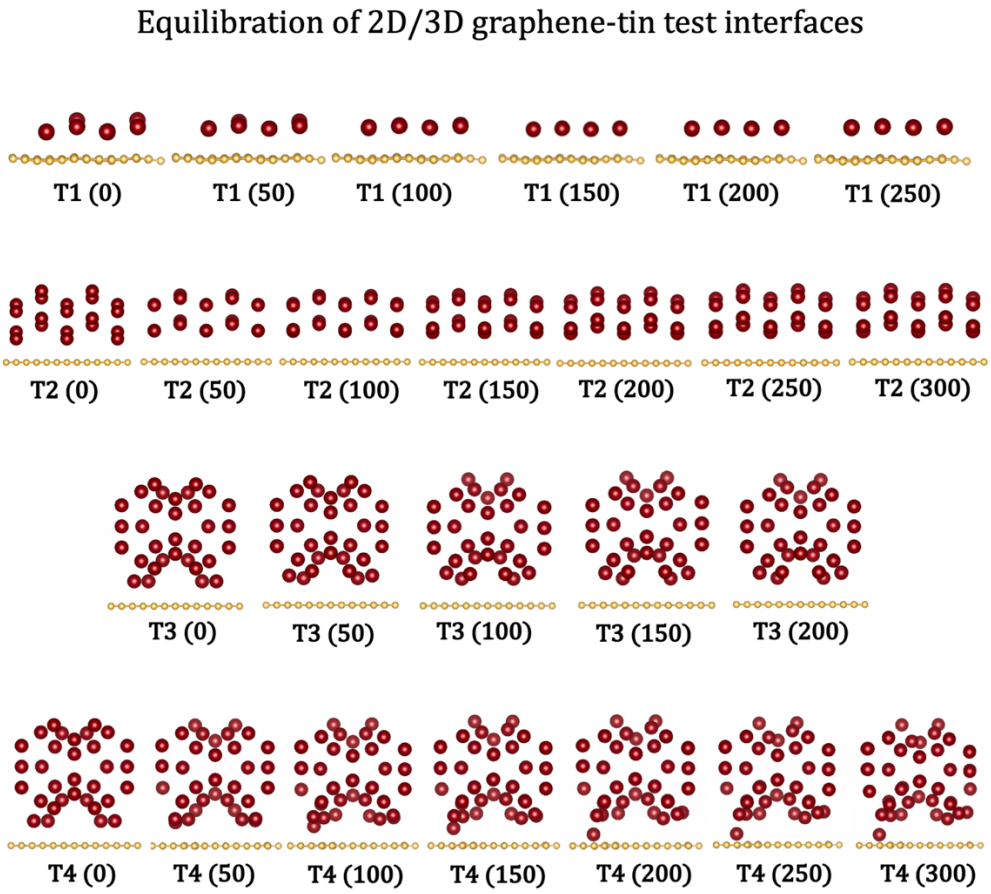

Figure 6.8 DFT optimization snapshots at different iterations of four test Gr|Sn interface structures.

6.4.3 Structural Descriptors

For representation of local environment of atomic coordinates, we use atom-centered symmetry functions (SF) introduced by Behler and Parrinello [242, 248], details of which are given in Sub section 6.3.3. SF were calculated for all reference structures with the help of DScribe package in Python, and the parameter set used is defined in Table 6.3 [259].

Table 6.3 Parameters Used to Compute the ACSF in the Study

Descriptors	Parameters	Values
G^2	R_c (Å)	8.9
	R_s (Å)	0
	η ($Å^{-1}$)	0.003214, 0.035711, 0.071421, 0.124987, 0.214264, 0.357106, 0.714213, 1.428426
G^4	R_c (Å)	8.9
	λ (Å)	-1,1
	ζ	1, 2, 4
	η ($Å^{-1}$)	0.003214, 0.035711, 0.071421, 0.124987, 0.214264, 0.357106, 0.714213, 1.428426

Note: Several values of R_c were tested and the value of 8.9Å was found to give optimum results for presented 2D|3D interface systems.

A non-zero R_s value can shift the center of Gaussian away from reference atom. Therefore, it is set to 0. We use a range of η values, which captures full dimensionality of the structures. The presented parameter set is chosen based on the benchmarking studies on descriptors for bicomponent bulk systems having elemental makeup similar to our structures [251, 260, 261]. λ usually takes value either +1 or -1 for inverting the cosine function. Hence both values +1 and -1 corresponding to both centers are used in the present SF set. To attain high angular resolution as well as complete coverage for intended interface systems, we use higher values for ζ in addition to 1 (ζ = 1, 2, 4). These SF set yielded best results in our comparative evaluation and served as foundation for further assessment of our model. R_c defines the extent of local environment of any atom to be represented as its input vector. Mostly large R_c in the range 6-12Å is preferred. For the presented interface structures, R_c = 8.9Å is found to be sufficient for optimum coverage of atom's local

environment (validation presented in Section 6.5.3). Moreover, SF inputs are independent of actual number of neighboring atoms within a set cut off radius R_c [252].

Using the SF set in Table 6.3, chemical environment of each atom was represented by 162 input features. It is important to note here that DScribe package used for conversion of cartesian coordinates to SF considers atomic number (Z) of chemical species in the environment of central atom by appending the value to SF (G^2 and G^4). However, it does not consider atomic number of central species in any way. To overcome this drawback, an additional input feature was added to the SF input feature for each atom which was its own atomic number. As such, each atom was represented by 163 input features in our study.

6.4.4 Training Models

Deep learning algorithm used in the present study is second generation high-dimensional neural network (HDNN) [255] described in Sub section 6.3.2. Cartesian coordinates of the system are converted to SF and used as input feature to a feed-forward neural network for each atom to express atomic energies. Since electronic simulations do not provide actual energy per atom, energy per atom is deduced based on total energy. Earlier works determine atomic energies by dividing total energy by the number of atoms which gives equivalent atomic energies for all the atoms in a system, as shown in Figure 6.9. This approximation is suitable for single component condensed systems where atoms are present in a single phase. However, we observe Gr|Sn interface structures to have multiple phases with strained interfacial Sn atoms. Thus, we assume interfacial Sn atoms will have higher atomic energies than sub-interfacial Sn atoms. Therefore, training distinct atomic chemical

environments in interface systems on uniform atomic energies is not considered a suitable approach.

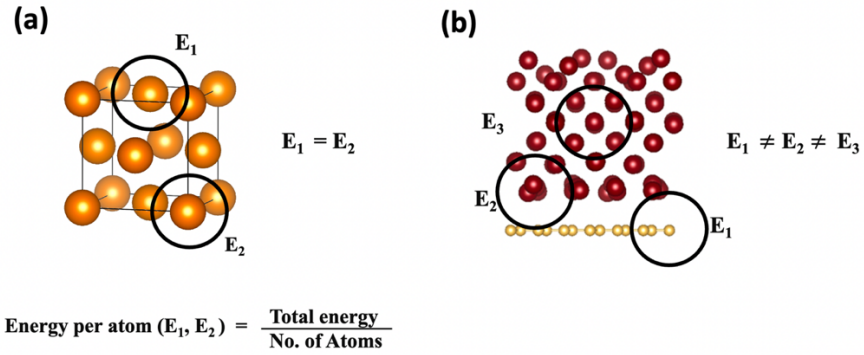

Figure 6.9 Atomic energies are deduced from total energy of the system by dividing later with total number of atoms in the system. (a) Schematic shows similar chemical environment of all atoms within the system ($E_1 = E_2$). (b) Side view of Gr|Sn interface structure containing 2D graphene, 3D Sn bulk having two distinct phases within a single system. Consequently, energies of individual atoms cannot be considered equivalent.

To validate this assumption, we used two different training approaches: Loss calculation with atomic energies and loss calculation with total energies. Atomic energies were derived from total energies per atom, as in earlier studies. Each atomic NN (*ann*) consists of 3 hidden layers having 100-50-10 nodes. The number of input features is 163. Here, hyperbolic tangent (tanH) activation function is used in the hidden layers while the output layer giving atomic energy contribution is linear (*ann*: 163-100-50-10-1). Weights and biases are optimized through supervised learning process using Adam optimizer[262] and learning rate 0.00001. Loss function after each epoch was determined by mean squared error of atomic energies from reference DFT data.

$$\boldsymbol{Loss} = \frac{\mathbf{1}}{\boldsymbol{Size}}\left(\boldsymbol{E_{DFT}} - \boldsymbol{E_{predict}}\right)^{\mathbf{2}} \quad \textbf{(6.6)}$$

Batch size for the training is kept 10 (*Size*) and accuracy of the energy prediction after each epoch is measured in terms of root mean square error (RMSE). Models are trained until accuracy metrics RMSE of at least 0.002 eV/Atom has been achieved. This amounted to 5000 epochs. The performance of trained model was validated (validation split = 10%), then tested on test structures T1 and T2.

In the second training approach, loss function was calculated from total energies of the system. This allowed model to assign atomic energies based on chemical space of each atom. Figure 6.10 presents an overview of the HDNN architecture utilized in the current work, code for which has been developed independently but is influenced by the ground concept of high-dimensional neural networks given by Behler and Parrinello(BPNN) in 2007 [248]. Herein, several neural networks referred to as atomic NN (*ann*) corresponding to each atom of the system are trained in parallel. Since atomic energy contributions are not available in reference DFT simulations, consequently atomic energies are summed to reproduce correct total energies. Collectively, output of all *ann* are added in the last layer and contribute towards the total energy of a system. The whole model is referred to as molecular neural network (*mnn*).

The present study of HDNN model is analytically different from original BPNN as per its treatment of atomic species in bicomponent systems and is contrasted in Figure 6.10 (a) and (b). For a system of six atoms, three Sn and three C, the first step in BPNN approach is converting cartesian coordinates to SF descriptors. SF of each atom *i* depend on the position of all atoms in the system. In the next step, atomic input features (G_i) are fed to

ann and 2 sets of *ann* weights are fitted corresponding to each chemical species in the system. In Figure 6.10(a), weights corresponding to Sn atoms (*red-ann*) are identical, and same is the case for weights corresponding to C atoms (*yellow-ann*). This ensures the invariance of total energy against interchanging of two identical atoms within set-a and set-b. In addition, this permits easy size extrapolation of the model. If another atom is added to the system, additional *ann* corresponding to the species can be appended to the architecture and added to the total energy expression. While BPNN has found wide success for a range of bicomponent systems[263], we realized it brought sensitivity to the ordering of atoms in the input file containing cartesian coordinates (poscar here) during the training process.

In the present study of HDNN model, first modification is made in featurization step in BPNN approach by specifying atom species along with SF. In the next step, weights of all *ann* (set-k in Figure 6.10(b)) were trained to be identical for our system of Sn-C. This was possible by shuffling G_i for each system during each epoch. Since G_i is a one-dimensional array, which already encodes information about the central atom species and its local chemical environment, permutations at this stage do not change either the atomic energy or combined total energy. All neural network architectures and weights are identically trained for a bicomponent system of Sn-C rather than individual species. Currently, *mnn* is functional for atom size 300 (*ann* = 300), but it can be extrapolated further as weights and architecture of trained *ann* are uniform.

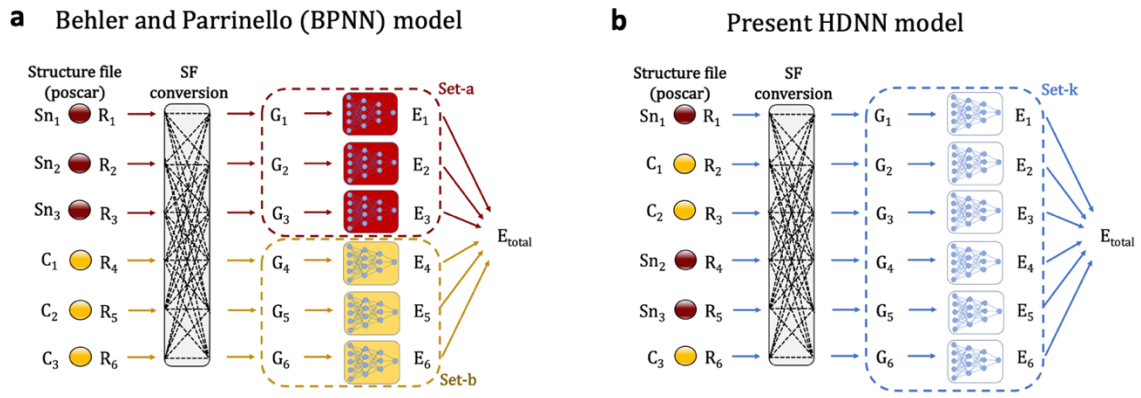

Figure 6.10 Comparative schematics of high dimensional neural networks for bicomponent (Sn|C) system. (a) High-dimensional neural networks given by Behler and Parrinello (BPNN) for bicomponent systems. Weights and architecture of atomic neural networks (*ann*) are same for single chemical species and therefore, positions of same atoms can be interchanged without changing the total energy of the system. Red-*ann* in set-a correspond to Sn atoms and yellow-*ann* in set-b correspond to C atoms. (b) High-dimensional neural networks (HDNN) utilized in current study of bicomponent systems. Weights and architecture of all atomic neural networks (*ann*) are same and correspond to the Sn|C system rather than single species.

For bicomponent system of C and Sn, nested *ann* with three hidden layers having 100-50-10 nodes is used. Hyperparameters of *ann* (*nodes, activation function*) remain the same as described before. Atomic energy E_i are added in the last layer to yield total energy E_{total}. Weights and biases were optimized through supervised learning process using Adam optimizer and learning rate 0.00001. Loss function after each epoch was determined by mean squared error of predicted total energies from reference DFT energies. Batch size for the training was kept one. Accuracy of the energy prediction after each epoch was measured in terms of root mean square error (RMSE), and the model is trained until total energy RMSE of at least 0.2 eV is achieved.

6.5 Results and Discussion

6.5.1 Phase Changes at Graphene|Sn Interface

The atomic specifications of Gr|Sn interface in DFT relaxed structures are discussed, which predominantly set apart these interfaces from Gr-based interfaces studied in earlier Chapters. Discussion of interface phenomenon is important to pave way for designing interfaces and controlling heterostructure properties in applied technologies. Coherent interface models were created between ordered single layer Gr and Sn allotropes with an optimum interfacial gap of 3.5 Å. Then, these systems were optimized by DFT to obtain relaxed strain-free interface configurations. Final interfacial configurations of Gr|Sn are depicted in Figure 6.11 for two prominent Sn allotropes, α-Sn and β-Sn, respectively. α-Sn is a diamond cubic crystal, and β-Sn is a body-centered tetragonal crystal (Figure 6.11(b)), which are two solid allotropes of Sn commonly used in technologies. At temperatures below room temperature (286 K), α-Sn is the stable phase, which transitions to its β configurations rather quickly as temperature rises [264]. Sensitivity of temperature conditions symbolizes the significance of solid Sn α↔β transitions for practical applications. This sensitivity elevates in the interfacial conditions with large lattice mismatch.

Differences of materials and lattice constants imply strained conditions in the buffer layer of Sn at the Gr|Sn interface, which conditions the Sn bulk towards a phase change. Consequently, lattice constants of interfacial Sn (c = 4.5Å) is different from the rest of the α-Sn bulk (c = 4.7Å) in Figure 6.11(a). This indicates a phase transformation from α-Sn to β-Sn in the buffer layer at Gr|α-Sn interface. However, these structural transformations of Sn are at a few layers limit at the surfaces and do not proliferate to central regions of the

bulk where α conformations are retained. Surface relaxation of α-Sn slab did not show any distortions, which eradicates the possibility of this structural reconstruction at Gr|α-Sn interface to be mere surface defects. The transformation of α-Sn to β-Sn happens rather quickly at the Gr interface during the DFT relaxation at 0 K. Intermediate Gr|α-Sn interface structures are depicted in Figure 6.7 between initial and equilibrium state which indicate rapid transformation first in the interfacial region (n=100), followed by the top Sn surface during early DFT iterations (n=250 iteration of total 1100 iterations). We repeated the simulation with increased vacuum in z dimensions to ensure transformation in the top layer is not due to periodic influence, but surface hardening of α-Sn to β-Sn, nucleated due to Gr interface. It is expected that at high temperatures, α-Sn to β-Sn transition can occur in entire Sn bulk and not be limited to surfaces as in the present 0 K conditions. In contrast to Gr|α-Sn interface, no transformations are noted in the relaxed Gr|β-Sn in Figure 6.11(c), indicating preference of Gr interface towards β-Sn. Structural changes in Sn at Gr interface are also significantly impacted by Sn bulk size. Figure 6.11 (d) and (e) exhibit Gr|Sn interfaces with smaller α-Sn and β-Sn bulks. Complete transformation of α-Sn_{32} bulk is noted in Figure 6.11(d) with a modified lattice constant of 4.52Å. Likewise, β-Sn_{16} rearranged over Gr surface as a single atomic layer in Figure 6.11(e) with near-atomic distances of 3.15Å. Drop in the Sn bulk size causes a reduction in dimensions of Sn bulk and brings all the Sn atoms to the surface, much like Gr.

Conventionally, well defined interfaces are obtained during epitaxial growth of Gr on substrates. However, interfaces presented here could be thought of as post growth modification rather than direct epitaxial growth. Relative differences in the material surfaces and charge analysis of Gr|Sn interfaces strongly indicates the weak van der Waals

forces to be the foundation of the formed interfaces. Charge analysis was performed in the said interfaces using Bader charge scripts by Henkelman group [179]. The net electron exchange across the Gr|Sn interface is less than $1e^{-1}$ for all interfaces denoting negligible covalent interaction.

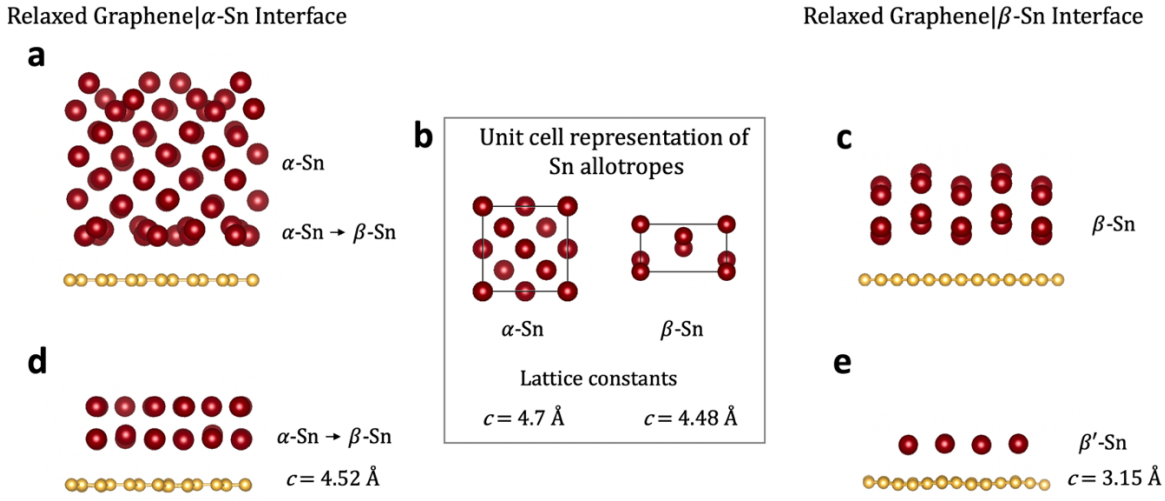

Figure 6.11 DFT relaxed Graphene|Sn interface systems. (a) Side view of relaxed Graphene|α-Sn_{64} interface system. Phase transformations of α-Sn to β-Sn noted in the Sn surface layers due to presence of graphene substrate. (b) Unit cell representations of α-Sn and β-Sn with lattice constants 4.7Å and 4.48Å, derived from materials project database (mp-117 and mp-84) and used for construction of Sn bulks. (c) Side view of relaxed Graphene|β-Sn_{32} interface system. (d) Side view of relaxed Graphene|α-Sn_{32} interface system. Phase transformation of α-Sn to β-Sn noted in the entire Sn bulk with modified lattice constant of 4.52Å. (e) Side view of relaxed Graphene|β-Sn_{16} interface with Sn rearranged over Gr surface as a single atomic layer of modified β'-Sn.

Sn is a well-known high-capacity anode for LIB and NIB with prominent shortcomings brought by phase transitions (β↔α) and volumetric strains. Presence of Gr substrate for Sn anode provenly scales down the volume expansion associated mechanical failures, and our analysis suggests it can also minimize frequented phase transitions from

β↔α due to its preference for β-Sn. Despite experimental studies, computational studies such as present are a necessity to closely understand the swift structural transformations. Tracing the equilibration of Gr|Sn interfaces with dominant possibility of Sn phase transformations is computationally expensive. It took approximately 7000 hrs with 72 CPU cores to finish complete relaxation of presented Gr|α-Sn interface system. As for molecular dynamics simulations, only a few classical force fields exist for C and Sn elements, which are again limited in their application in describing the polymorphing Gr|Sn interface. For these reasons, we attempted to utilize AI in developing PES for Gr|Sn interfaces to facilitate future studies.

6.5.2 Model Performance by Loss calculation with Atomic Energies

Atomic NN are trained by calculating loss function from atomic energies deduced from total energies of the system as described in Sub section 6.4.4. The performance of trained model is determined by predicting atomic energies of 10% validation split, which results in 0.0042 eV/Atom. This result is comparable to some earlier reported deep learning studies on condensed phase systems [265, 266]. This concludes that this strategy is effective to develop PES for interfaces as well if target interfaces are similar to the training data. Next, trained neural network weights were further used to predict atomic energies of test structures T1 and T2. The results have been summarized in Table 6.4. While model performed well on validation split, which is the test data randomly separated out of training data, its performance for new interfaces has been poor, indicating overfitting. This proved our assumption regarding inadequacy of using atomic energies for training.

Table 6.4 Performance of PES on Validation Set and Test Interface Structures

Performance	RMSE in eV/atom
Validation set	0.0042
T1	0.2235
T2	0.9496

6.5.3 Model performance by Loss calculation with Total Energies

HDNN model depicted in Figure 6.10(b) is trained on 5789 Gr|Sn interface structures with corresponding DFT-derived system energies. The model is trained until total energy RMSE of at least 0.2 eV is achieved. Once trained, model weights are used to predict energies of test structures obtained from T1 (familiar interface, different orientation). Between unequilibrated and equilibrated T1 structures, there are approximately 260 structural configurations. All of which were used as test data. Figure 6.12 compared system energies of T1 structures obtained from DFT (E_{DFT}) with energies predicted by trained model ($E_{predict}$). Both system energies match closely with RMSE value 0.0901eV. Slight error is noted for non-equilibrated structures (below 50 DFT iterative structures), which further reduces as the structure stabilizes. Because HDNN are fitted to the total energies of the structure, we note that $E_{predict}$ is bordering on E_{DFT} values but is not equivalent to the exact values even though T1 interface is very close to trained structural configuration.

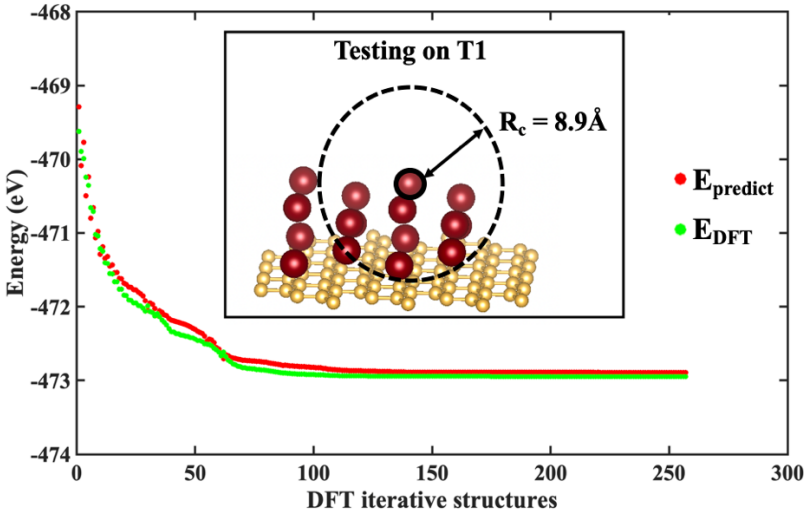

Figure 6.12 Total energies of the test structures T1 predicted by trained HDNN model. $E_{predict}$ and E_{DFT} are total energies predicted by HDNN and DFT, respectively.

We used a wide range of SF parameters to describe the complete chemical space of each atom, as detailed in Section 6.4.3. The performance of model was highly sensitive to R_c value considered. Figure 6.13 compared performance of HDNN model when R_c value was varied between 6Å and 11Å for Gr|Sn interface systems. Best results have been obtained with R_c = 8.9Å, and accordingly, we used this R_c value for all analyses in the present work described in this chapter.

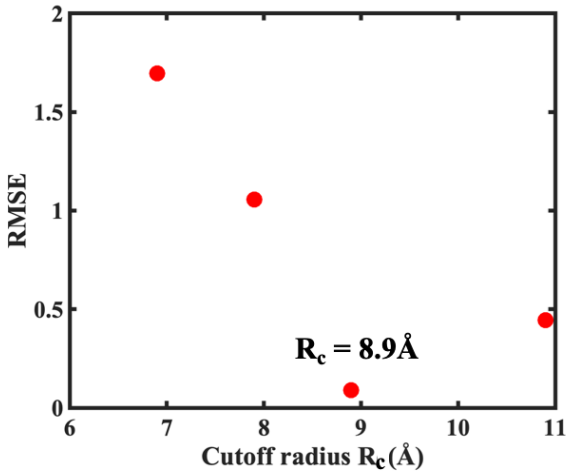

Figure 6.13 SF cutoff radius (R_c) validation with SF parameter set presented in Table 6.3. Root mean squared error (RMSE) in eV for total energy prediction of test structures T1 with HDNN model.

6.5.4 Testing on New Interfaces

The primary objective of the targeted potentials (PES) is the ability to predict close to DFT energies of new Gr|Sn interfaces and avail least computation necessary during the development. The HDNN model trained on structures from 5 Gr|Sn interfaces has been tested on new interfaces T1-T4 described in Section 6.4.2. The results are summarized in Table 6.5 and Figure 6.14. Between unequilibrated and equilibrated system configurations, there are approximately 260-400 structural configurations for each test structures, each of which was used for testing. Energies predicted by HDNN weights of new interfaces have smaller RMSE values (eV/Atom). RMSE values for T1 and T2 in Table 6.5 are significantly lower than RMSE values noted in Table 6.4. This clearly indicates that deep neural network model designed for such multiphasic interfaces should train across total energies rather than atomic energies to gather complete system information. The difference noted in energies of completely unfamiliar interfaces T3 and T4 is also relatively small. In

absence of accurate MD potentials in literature, the developed PES demonstrates acceptable performance for new Gr|Sn interfaces constituting of phase transitions, interfacial diffusion and defects.

Table 6.5 Performance of Trained HDNN Weights on Unfamiliar Test Interfaces

Test interface	RMSE eV/atom
T1	0.016
T2	0.222
T3	0.360
T4	0.458

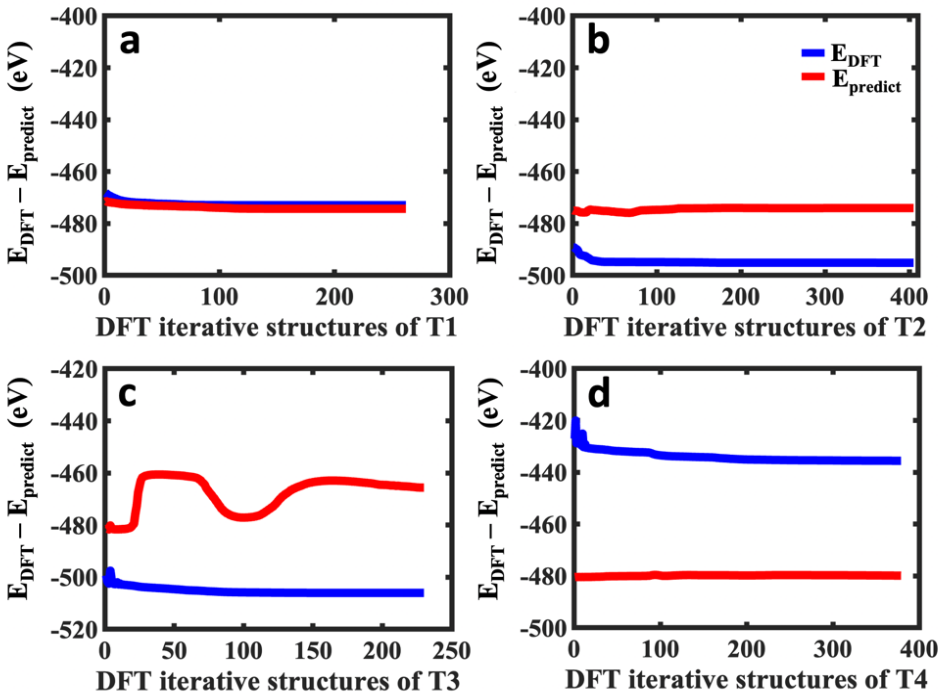

Figure 6.14 Total energies of the test structures T1-T4 predicted by trained HDNN model. $E_{predict}$ and E_{DFT} are total energies predicted by HDNN and DFT, respectively.

6.6 Scope and Summary

The work presented in the Chapter attempts to develop ML-based PES to predict energies of complex graphene-based 2D/3D interface systems that could be automated and used to replace expensive DFT in the future studies. Graphene and tin interface system has been used as a model system. Applicability of high dimensional neural networks developed by Behler and Parrinello that utilize atom-centered symmetry functions as structural descriptors has been shown. The initial approach to calculate loss function on atomic energies showed good performance on validation split but failed to predict energies of new interface systems. To overcome this, slight modifications are made in HDNN model that enable it to be trained on total energies of the system. The second approach significantly improves the performance of PES in predicting the total energies of new interface systems. Primary reason for this enhanced performance is the freedom model gained to assign atomic energies based on atomic chemical environment. Thus, in further work, correct atomic energies and forces can be derived from the model, allowing scope for automated equilibration.

CHAPTER 7

CONCLUSIONS

As this study comes to an end, let us distill some main ideas regarding battery interfaces met during this journey. We have used first principles and data-driven techniques to characterize interfaces between two-dimensional (2D) materials and three-dimensional (3D) bulk electrodes for metal ion batteries that are renewable as well as cheaper. The coalition between the chemistry, mechanical strength, and electrochemistry has been established for these heterostructure electrodes that hold future potential to commercialize cheaper sodium and potassium ion batteries. Let us summarize important conclusions:

Considering shortage of Li metal, we can look forward to replacing LIBs with NIBs once we have overcome the lack of appropriate anode for NIB. We investigated sodiation kinetics in amorphous Ge anode for NIB and established its similarities to Li-Si system. The volume expansion of Na-Ge alloy electrode has been found to be approximately 149.51% in the fully sodiated state (NaGe) which is lesser than other alloying anode candidates. The Na intercalation was not feasible in crystalline Ge. Thus only amorphous Ge can be used to accommodate Na. Yet, despite starting and final stable amorphous phases, system undergoes minute phase transitions to crystallinity for smaller Na concentrations (Na < 20%). Post 50% sodiation, system was amorphous throughout. Moreover, we calculated diffusivity of single Na in a-Ge_{64} to be 4.876×10^{-9} cm^2/s at 300 K, which is greater than previously reported diffusivities of Na in other group 14 and 15 elements.

Alloying electrodes such as Ge can be combined with 2D materials such as graphene for mechanical stability and long battery cycle life. This approach has found tremendous success for Si-Li anodes in LIBs. However, the interface between electrode and 2D additive needs to be characterized and studied for lattice distortions, mechanical strength, chemical reactivity, and overall stability before proceeding to design bicomponent nanoelectrodes. Since Ge remains amorphous throughout the battery cycle, we used a different alloying electrode for interfacial study. Se is a high-capacity cathode that can overcome capacity limitations of cathodes in LIB, NIB as well as KIBs. Yet again, Se reaction with Li/Na/K is accompanied by dissolution in electrolyte and significant volume expansions causing chemo-mechanical degradation. This condition is controlled by adding a graphene additive, which constricts selenides from dissolution and provides buffer space for volume expansion. We performed a comparative study of interfacial characteristics for Se-Gr interface for two different Se allotropes, namely monoclinic and amorphous. Our interface strength results show that Se/Gr interfaces have interface strength (0.43 J/m^2 and 0.34 J/m^2) comparable to amorphous Si/Gr interface (0.41 J/m^2). Therefore Se/Gr interface systems will retain the benefits of Si/Gr interface in terms of mitigating interfacial stresses during ion battery cycles. There is only a small variation in interface strength when Se changes phase from monoclinic to amorphous. However, Se/Gr interfaces can unbind quite easily due to polarity (potential gradient $d\phi/dz = 3.03$ eV/Å) and lack of stable chemical interaction (net electron exchange $\Delta q = 0.3119\ e^{-1}$) between both the materials if electrode morphologies are not carefully designed.

We further investigated interfacial characteristics in Se-Gr cathode for KIB and correlated it to the state of charge. We observed that graphene substrate creates a substantial

chemical gradient inside the K-Se cathode and nucleates small crystalline pockets in the otherwise disordered cathode bulk. The Se-K clusters formed in the cathode interact strongly with graphene surface through binding energies (E_{ad}) as high as -3.137 eV for SeK_6 and -3.419 eV for SeK_7. These strong binding preferences between clusters and graphene are needed to avoid dissolution of selenides in electrolytes, but they can cause difficult deintercalation in several K_xSe intermediates. Between K and Se, there is a single step reaction near 1.55 V with K_2Se as discharged product. To avoid capacity losses due to difficult K intercalation/deintercalation, graphene-supported Se cathode should operate in the voltage range of 1.55V to 1.38V. These studies emphasized the electrochemical changes brought in by addition of graphene in bulk electrodes.

Recent years have seen emergence of new 2D materials that are similar to graphene in terms of mechanical and electronic properties but differ in structural arrangement. While carbons in graphene are arranged in in-plane lattice, 2D materials like MXenes have out-of-plane surface functional groups. Upon mixing with Si, experimental reports have shown that Si/MXene composite excels in performance over its parent Si anode in capacity retention and cycle stability. We performed DFT simulations to quantify the variation in interface strength between 3D amorphous Si bulk and surface terminated $Ti_3C_2T_x$ MXenes with different functional groups. According to results, -OH functionalized MXene binds most strongly to amorphous Si with interface strength of 0.606 J/m^2 in comparison to -OH/O mixed and -F functionalized MXenes. Since functional groups are vertically aligned on the MXene surface, chemisorption of Si bulk on MXene surface results in high concentration of charges in the interfacial region, causing steric hindrance and low interface stability. Thus, physisorbed interfaces have better interface strength.

First principle techniques like DFT proved efficient in providing an accurate account of thermodynamic stability of these 2D/3D interfaces. Conversely, these computational insights come at huge computation cost and time. We next developed deep learning-based methodology that can be used to predict energies of 2D/3D interface structure with close to first principles accuracy. The key point of our methodology has been that it required less training data than the conventional methods. High dimensional neural networks are used to train training data derived from 5 graphene-based Sn interfaces and loss function is calculated from the total energies of the system. This approach is shown to significantly improve the performance of trained weights in predicting the total energies of new interface systems. Primary reason for this enhanced performance is the freedom model gained to assign atomic energies based on each atom's chemical environment.

In conclusion, all these findings are the first step in developing an understanding of the role of heterostructure interfaces in performance of battery electrodes and extending the computational tools to study them from existent atomic methods to data-driven methods. There is still a lot that can be unearthed in this arena of science. We hope these results can serve as the foundation for the future development of multicomponent electrodes.

CHAPTER 8

FUTURE DIRECTION

Heterostructure Electrodes for Future Batteries. Study of interfaces between materials and their impact on applicative performance is only catching up after discovery of 2D graphene and advancements in tools to study interactions at atomic scale. Heterostructure electrodes are designed when a singular material cannot efficiently store charge and require assistance from an additive to uphold mechanical integrity and electrochemical performance altogether [41, 45]. Heterostructures based on 2D-2D and 2D-3D materials have been actively studied for LIBs [267, 268]. Throughout this Dissertation, we discuss example studies where process of lithiation, conversion reaction, interfacial diffusion kinetics and state of charge have been explored in these heterostructures. When compared to LIBs, scope of 2D-3D heterostructures in alternative batteries like NIB and KIBs is still less explored. Smart heterostructure electrodes need to be designed to combat volume expansion upon ion intercalation. More computational studies are required that can throw light on the effect of lattice mismatch upon ion storage or the changing interface chemistry [269]. Furthermore, conversion reactions and potential for reversible formation of crystalline structures upon deintercalation has not been covered in any works.

As our computational results provide a deeper insight into the interface between different allotropes of bulk electrodes with pristine graphene, there is further scope for the analysis to be extended for variations in graphene morphologies such as wrinkles, point defects, doping, and multiple layers. The present results of interface strength by DFT are sensitive to atomic size of the bulk considered and can deviate from the values realized in

any macroscopic model. On the macroscopic scale, electrode-additive interfaces could take numerous forms like core-shell, mesh enclosed nanoparticles, and substrate-hosted nanorods, to name a few. Atomic size of the systems during the interface DFT calculations is as small as 100-150 atoms and are based on the assumption that 150 atoms interface is a nano-interface that integrates to form large interface analogous to macroscopic ones, without taking macroscopic surface modulations into consideration.

Liquid-Solid Interfaces. Solid-liquid interfaces in batteries have always been under-represented in theoretical studies, primarily due to large size of atomic aqueous system for computation. While electrolyte and electrode interfaces have been studied using molecular dynamics (MD)[129], it is not an ideal tool to study thermodynamic sensitive subjects like diffusion barrier, adsorption energy and interface energy due to dependence of MD on empirical potentials. Despite the limited scope of DFT and MD, there are a lot of burning problems regarding electrode-electrolyte interfaces in batteries that need to be addressed [270].

The idea of confining fluids in the interfaces of stacked 2D materials is novel and driven with to increase interlayer spacing to direct faster atomic diffusion within [271, 272]. However, the presence of fluid in the interface of 2D materials greatly changes the interface dynamics, as the result, might affect the overall connectivity and conductivity in structure. The complete effect of fluid content on the intercalating ion in 2D material based heterostructures is still not well-established.

Artificial Intelligence Driven Studies. In the light of shortcomings posed by atomistic simulations, artificial intelligence-based methodologies can be counted upon not just to explore the subject of interest, but also to develop new alternative workflows. Information obtained from DFT and MD is dependent upon physical parameters. In the absence of adequate physical parameters, we can rely on concept of 'learning' to predict battery stability. ML can be used to develop effective autonomous methods to find a stable material combination. ML-based models have already proven to be effective means to discover new battery materials [131-138]. Yet, they have not been sufficiently utilized to study interface systems. Unique complexities of the interface pose a challenge in complete chemical representation and prediction of interfacial systems. Most importantly, there is a lack of availability of data on interface structures in databases which makes ML training dependent on ab-initio and MD simulations. The ML-based techniques discussed in our study focused on developing reliable ML models in the absence of extensive data for unique interfaces. The workflow can be automated to replace atomic stimulations in future.

APPENDIX A

MODELING AMORPHOUS GERMANIUM FROM CRYSTAL

In order to model *a*-Ge_{64}, we started from *c*-Ge_{64} (Face Centered Crystal) and generated *a*-Ge_{64} via computational quenching process. The quenching process is a combined AIMD and DFT relaxations involving heating, cooling and equilibration for significant amount of time steps (in this case 5000MD time steps with 1 fs time interval). In our study, the highest and lowest temperatures for the AIMD run were 5000K and 298 K (room temperature). Temperature 5000K was chosen because it was sufficiently high enough to create Ge melt. Finally, *a*-Ge_{64} was obtained via further DFT optimization of the room temperature AIMD simulated lowest energy (local minima) Ge_{64} structure. Amorphous phase of the generated structure was confirmed by taking PCF. The first neighboring distance was found to be at ~2.6 Å in generated structure which was close enough to previously reported first neighboring distance in *a*-Ge (2.55Å) in literature [148]. While *c*-Ge is known to exhibit first neighboring distance at 2.4Å [148] and prominent second and third peaks, no such trend is noticed in PCF analysis of *a*-Ge. *a*-Ge is characterized by a single prominent peak at ~2.6 Å in our study.

In order to evaluate variations in amorphous structures upon changing melting temperatures, quenching process was repeated following above mentioned steps at 3000K and 7000K, respectively. All these temperatures were well above the melting temperature of Ge (1200K). It was noticed that final quenched and relaxed amorphous structures were not much different from each other. It can be seen in Figure A.1 that *c*-Ge turned

completely amorphous at all three temperatures and their PCF graph shows similar trend of a single prominent peak at ~2.6Å.

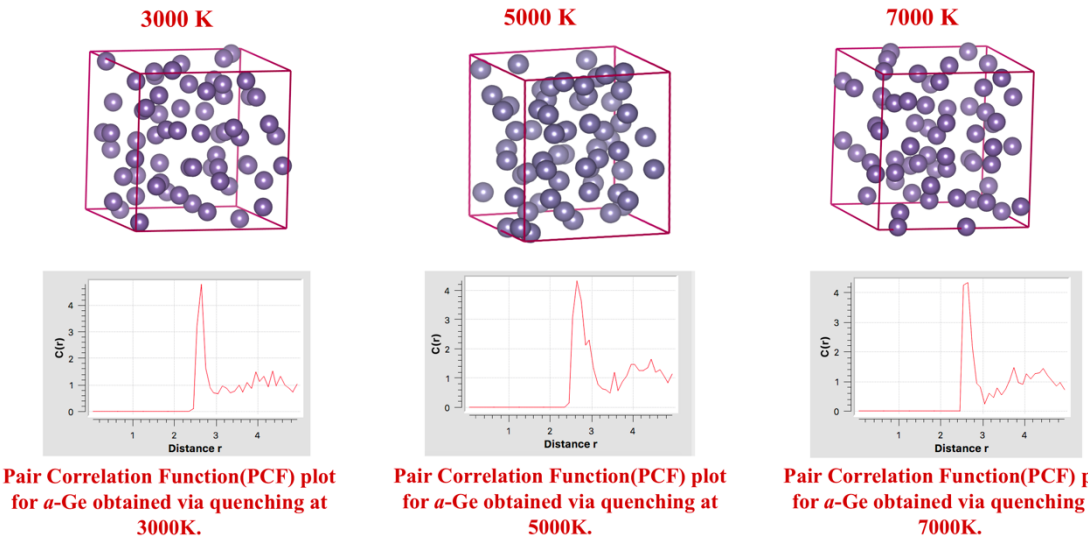

Figure A.1 Comparison of amorphous Ge structures generated via process of quenching at different high temperatures: 3000K, 5000K and 7000K. First neighboring distance obtained in PCF analysis did not show much variation if we increased quenching temperature from 3000K to 7000K and remained in range of 2.6Å.

APPENDIX B

VARIATION IN GRAPHENE INTERFACE STRENGTH AS LI CONCENTRATION VARIES

The interface strength value between active electrode and graphene is expected to decrease with increasing concentration of Li in the electrode. To validate this, interface strength between lithiated Si electrode and graphene substrate was calculated as described in Sub section 3.3.1 and compared with Si/Gr interface strength determined earlier. For creation of $Li_{0.5}Si$/Gr system, 32 Li atoms were sequentially inserted into *a*-Si_{64}/Gr as system was allowed to relax using ab-initio molecular dynamics (AIMD) simulations within the DFT framework of VASP. AIMD simulation permitted atoms to mix sufficiently. The simulation was run with 1 fs time interval at room temperature within NVT ensemble and 2 X 2 X 1 gamma centered k-meshes were taken into account. Post this, 3 material slabs were created of Gr, $Li_{0.5}Si$ and $Li_{0.5}Si$/Gr interface with an added vacuum of 14 Å in z dimensions. The structures were optimized using DFT in VASP with configurations as described in the main manuscript. Figure B.1 shows interface strength for *a*-Si/Gr electrode to reduce as Li concentration increased. The interface strength of $Li_{0.5}Si$/Gr interface was calculated to be 0.38 J/m^2 using Equation (3.1) of work of separation (W_{sep}). Likeliness between Si/Gr and Se/Gr interfaces suggests interface adhesion at Se electrode and Gr interface will also decrease with increase in Li concentration.

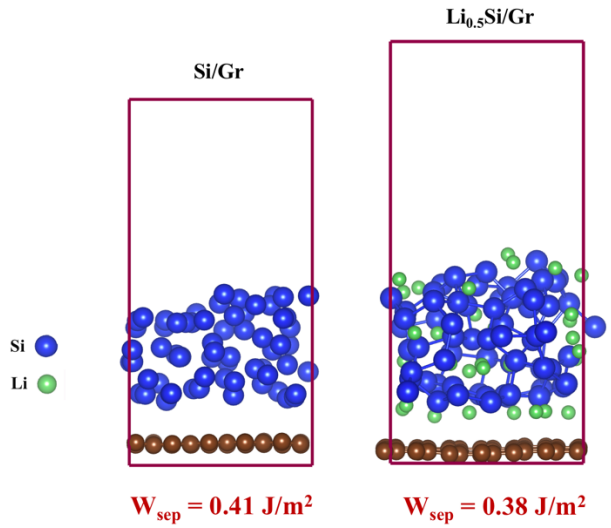

Figure B.1 Drop in interface strength of graphene (Gr) with amorphous Si electrode as Li concentration increased in the system. Interface strength is determined as work of separation (W_{sep}) for Si/Gr interface to be 0.41 J/m^2 and $Li_{0.5}Si$/Gr to be 0.38 J/m^2.

APPENDIX C

DISTORTIONS IN SE CRYSTAL IN SE/GR INTERFACE

Lattice distortions are common occurrence when two distinct crystal lattice are put together. Figure C.1 demonstrates slight distortions observed in monoclinic Se rings when it was interfaced with a graphene lattice and DFT optimized.

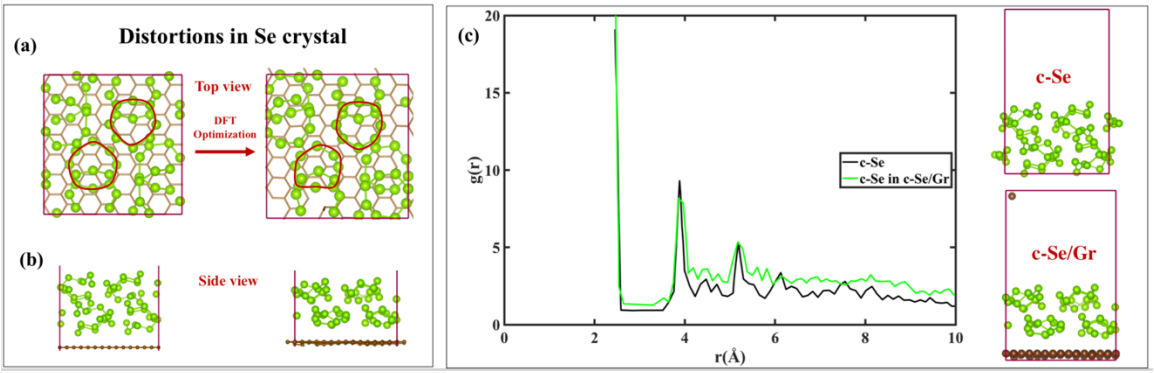

Figure C.1 (a-b) Top and side view initial to final DFT optimized structure of *c*-Se_{64} over graphene substrate. Se atom rings of 8 were maintained with slight change in vertical orientations. The crystal structure condensed towards graphene causing changes in dihedral angles. (c) Comparative RDF plot of c-Se independently and *c*-Se optimized over graphene surface. No significant change in near neighboring distances or position of crystal peaks is noted in latter. Only intensity of intermittent small peaks increases slightly with peak broadening.

APPENDIX D

VARIATIONS IN SILICON-MXENE INTERFACE ENERGY

Thermodynamically, interface strength is sensitive to the energy of interface system E_{12}. Interface strength depends on the difference between E_{12} and the sum of energies of the individual materials ($E_1 + E_2$). If E_{12} is lower than $E_1 + E_2$, both materials can come together to form a stable interface with a positive interface strength. In contrast, the high system energy of the interface E_{12} indicates either lack of chemical interaction or the presence of interfacial strains due to local charge redistribution. Both these conditions are the ancillary outcome of interfacial gap *d*. If *d* between the two materials is too high, there is a possibility of a lack of chemical interaction. Conversely, if *d* is too low, atoms in the interface might be strained due to lattice misfit or stearic repulsions caused by the concentration of charges.

We performed AIMD simulations within the DFT framework to trace the changes in interface system energy E_{12} as the interfacial gap *d* varies due to diffusion of Si atoms in the interfacial region. We employed relaxed structures of three different *a*-Si/ $Ti_3C_2T_x$ interface systems (each having different MXene surface functionalization, initial $d \sim 1.5$ Å, and vacuum of 20 Å in z dimension) and observed the changing interfacial gap for 1000 AIMD steps. Snapshots of the starting three configurations are shown in the insets of Figure D.1. The two materials are very close ($d < 2$ Å) in the start, which causes strain on the surface functional groups, as depicted by O-H bonds' alignment in the snapshots. During the AIMD run, system energies E_{12} fluctuate as the interfacial gap *d* is altered due to movement of loosely bound interfacial Si atoms. These changes occurred during different time frames for the three interface systems. Since our primary focus lay in observing the

correlation between the interfacial gap and the system's stability, we plot only the system energy E_{12} for the individual interfaces corresponding to the *d* at that specific AIMD frame.

The three plots clearly demonstrate a drop in the system energy E_{12} with an initial increase in interfacial gap *d*, followed by a rise of E_{12} as *d* further increases. The trend is clearly in accordance with the previous graphene-based works [237] and indicates the formation of a potential well between 2 - 2.5 Å interfacial gap for all three interface systems. This drop of energy E_{12} indicates stability and agrees with our assumption that the distance of 2 - 2.5 Å between the current material surfaces should facilitate interface formation. While the value of *d* for potential wells are not absolute, they represent a close range where system stability could be achieved. It is apparent in Figure D.1(a) and (b) that *a*-Si/MXene interface is most stable at the interfacial gap ~2Å when MXene surface is functionalized with -OH and -O groups. In the case of fluorinated MXene, the potential well shifts slightly towards higher *d*. Determination of absolute *d* for potential well required very precise measurements of the distance between the two surfaces. This was not possible for our current configurations, where one material is amorphous, consisting of loosely bound and non-uniformly distributed surface Si atoms. Another important observation that can be made from the presented plot is regarding the system energy at $d < 2$Å. Upon comparing the three interface systems, the system energy at $d < 2$Å was very high for completely hydroxylated and fluorinated MXene interfaces. In contrast, interface system with -OH/O mixed surface functionalization appears comparatively stable at *d* as low as 1Å. This is plausible due to bond formation between interfacial Si atoms and reactive -O groups on the MXene surface, also visible in the snapshot of the initial configuration in Figure D.1(b). H and F atoms on the surface of hydroxylated and fluorinated MXenes are

well-coordinated and not free to form covalent bonds with Si atoms. Thus, close vicinity of Si surface causes strain on H-O, O-Ti, and F-Ti bonds, resulting in very high system energies. On the other hand, in second interface system, very close proximity of Si surface does cause certain strain to H-O bonds, but some loosely bound Si atoms diffuse closer to the surface to form Si-O bonds with the surface -O groups.

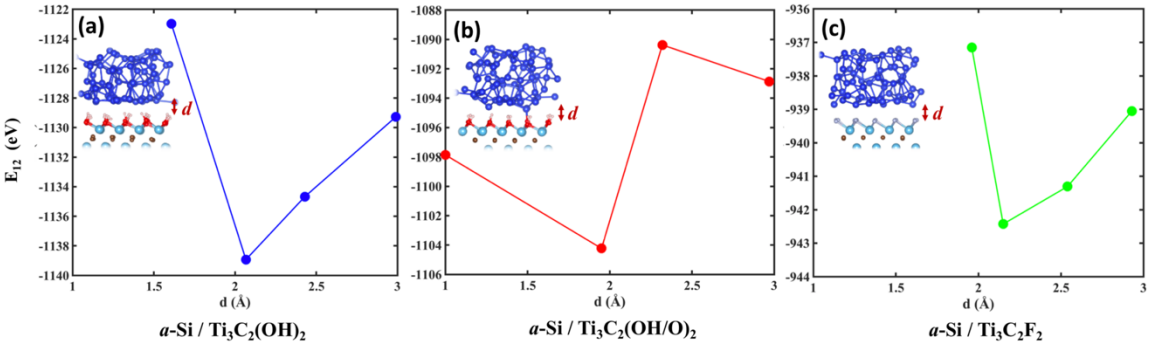

Figure D.1 Variation of interface system energy E_{12} with interfacial gap *d*. Energy profiles of interface systems as distance between the two materials change during AIMD simulation. The insets depict side view of initial *a*-Si/MXene interface structures with *d* ~1.5Å. (a) *a*-Si/$Ti_3C_2(OH)_2$ interface, (b) *a*-Si/$Ti_3C_2(OH/O)_2$ interface, and (c) *a*-Si/$Ti_3C_2F_2$ interface.

APPENDIX E

SURFACE ENERGIES OF SELENIUM STRUCTURES

Surface energies of Se structures were determine as:

$$\frac{1}{A}\left(E_{slab} - nE_{bulk}\right) \quad \text{(E.1)}$$

Here, E_{slab} is the energy of Se vacuum slab, E_{bulk} is the energy of periodic Se bulk, n is the number of surfaces in slab and A is surface area of slab. The surface energies of selenium models are presented in Table E.1. Surface energy of crystalline *c*-Se_{64} is noted to be close to the experimental measure[273] of solid Se surface energy. With particle size, surface energy changes by ~0.02 J/m^2 as noted for *c*-Se_{64} and *c*-Se_{32} in Table E.1.

Table E.1 Surface Energies of Selenium Models

Selenium model	Surface Energy (J/m^2)
c-Se_{32}	0.224
c-Se_{64}	0.248
a-Se_{64}	0.375

REFERENCES

[1] M.S. Whittingham, Electrical energy storage and intercalation chemistry, Science 192(4244) (1976) 1126-1127.

[2] M.S. Whittingham, A.H. Thompson, Intercalation and lattice expansion in titanium disulfide, The Journal of Chemical Physics 62(4) (1975) 1588-1588.

[3] J.-M. Tarascon, M. Armand, Issues and challenges facing rechargeable lithium batteries, materials for sustainable energy: A Collection of Peer-Reviewed Research and Review Articles from Nature Publishing Group, World Scientific,2011, pp. 171-179.

[4] K. Mizushima, P. Jones, P. Wiseman, J.B. Goodenough, LixCoO2 (0< x<-1): A new cathode material for batteries of high energy density, Materials Research Bulletin 15(6) (1980) 783-789.

[5] Z. Shu, R. McMillan, J. Murray, Electrochemical intercalation of lithium into graphite, Journal of The Electrochemical Society 140(4) (1993) 922.

[6] M. Armand, J.-M. Tarascon, Building better batteries, Nature 451(7179) (2008) 652-657.

[7] F.-Z. Teng, W.F. McDonough, R. Rudnick, C. Dalpé, P. Tomascak, B.W. Chappell, S. Gao, Lithium isotopic composition and concentration of the upper continental crust, Geochimica et Cosmochimica Acta 68(20) (2004) 4167-4178.

[8] D.W.I.R.M. Hahn, Techniques for raman analysis of lithium-ion batteries, Spectroscopy (2015), 30, 1-3.

[9] K. Zaghib, C. Julien, J. Prakash, New trends in intercalation compounds for energy storage and conversion: Proceedings of the International Symposium, The Electrochemical Society, 2003.

[10] A. Du Pasquier, I. Plitz, S. Menocal, G. Amatucci, A comparative study of Li-ion battery, supercapacitor and nonaqueous asymmetric hybrid devices for automotive applications, Journal of Power Sources 115(1) (2003) 171-178.

[11] J. Tollefson, Charging up the future, Nature 456(7221) (2008) 436.

[12] M. Obrovac, O. Mao, J. Dahn, Structure and electrochemistry of LiMO 2 (M= Ti, Mn, Fe, Co, Ni) prepared by mechanochemical synthesis, Solid State Ionics 112(1) (1998) 9-19.

[13] A. Shukla, T. Prem Kumar, Materials for next-generation lithium batteries, Current Science 94(3) (2008) 314-331.

[14] X.H. Liu, L. Zhong, S. Huang, S.X. Mao, T. Zhu, J.Y. Huang, Size-dependent fracture of silicon nanoparticles during lithiation, ACS Nano 6(2) (2012) 1522-1531.

[15] E. De La Llave, V. Borgel, K.-J. Park, J.-Y. Hwang, Y.-K. Sun, P. Hartmann, F.-F. Chesneau, D. Aurbach, Comparison between Na-ion and Li-ion cells: understanding the critical role of the cathodes stability and the anodes pretreatment on the cells behavior, ACS Applied Materials & Interfaces 8(3) (2016) 1867-1875.

[16] V. Palomares, P. Serras, I. Villaluenga, K.B. Hueso, J. Carretero-González, T. Rojo, Na-ion batteries, recent advances and present challenges to become low cost energy storage systems, Energy & Environmental Science 5(3) (2012) 5884-5901.

[17] A. Eftekhari, Potassium secondary cell based on Prussian blue cathode, Journal of Power Sources 126(1-2) (2004) 221-228.

[18] S. Komaba, T. Itabashi, T. Kimura, H. Groult, N. Kumagai, Opposite influences of K+ versus Na+ ions as electrolyte additives on graphite electrode performance, Journal of Power Sources 146(1-2) (2005) 166-170.

[19] W. Zhang, Y. Liu, Z. Guo, Approaching high-performance potassium-ion batteries via advanced design strategies and engineering, Science Advances 5(5) (2019) eaav7412.

[20] V.B. Mohan, K.-t. Lau, D. Hui, D. Bhattacharyya, Graphene-based materials and their composites: A review on production, applications and product limitations, Composites Part B: Engineering 142 (2018) 200-220.

[21] D. Datta, J. Li, N. Koratkar, V.B. Shenoy, Enhanced lithiation in defective graphene, Carbon 80 (2014) 305-310.

[22] A. Buldum, G. Tetiker, First-principles study of graphene-lithium structures for battery applications, Journal of Applied Physics 113(15) (2013) 154312.

[23] S.-L. Chou, J.-Z. Wang, M. Choucair, H.-K. Liu, J.A. Stride, S.-X. Dou, Enhanced reversible lithium storage in a nanosize silicon/graphene composite, Electrochemistry Communications 12(2) (2010) 303-306.

[24] J. Luo, X. Zhao, J. Wu, H.D. Jang, H.H. Kung, J. Huang, Crumpled graphene-encapsulated Si nanoparticles for lithium ion battery anodes, The Journal of Physical Chemistry Letters 3(13) (2012) 1824-1829.

[25] Y. Wen, Y. Zhu, A. Langrock, A. Manivannan, S.H. Ehrman, C. Wang, Graphene-bonded and-encapsulated Si nanoparticles for lithium ion battery anodes, Small 9(16) (2013) 2810-2816.

[26] J. Ji, H. Ji, L.L. Zhang, X. Zhao, X. Bai, X. Fan, F. Zhang, R.S. Ruoff, Graphene-encapsulated Si on ultrathin-graphite foam as anode for high capacity lithium-ion batteries, Advanced Materials 25(33) (2013) 4673-4677.

[27] M. Ko, S. Chae, S. Jeong, P. Oh, J. Cho, Elastic a-silicon nanoparticle backboned graphene hybrid as a self-compacting anode for high-rate lithium ion batteries, ACS Nano 8(8) (2014) 8591-8599.

[28] M.-Q. Zhao, Q. Zhang, J.-Q. Huang, G.-L. Tian, J.-Q. Nie, H.-J. Peng, F. Wei, Unstacked double-layer templated graphene for high-rate lithium–sulphur batteries, Nature Communications 5(1) (2014) 1-8.

[29] G. Zhou, S. Pei, L. Li, D.W. Wang, S. Wang, K. Huang, L.C. Yin, F. Li, H.M. Cheng, A graphene–pure-sulfur sandwich structure for ultrafast, long-life lithium–sulfur batteries, Advanced Materials 26(4) (2014) 625-631.

[30] M.K. Datta, R. Epur, P. Saha, K. Kadakia, S.K. Park, P.N. Kumta, Tin and graphite based nanocomposites: Potential anode for sodium ion batteries, Journal of Power Sources 225 (2013) 316-322.

[31] Y. Yang, G. Zheng, Y. Cui, Nanostructured sulfur cathodes, Chemical Society Reviews 42(7) (2013) 3018-3032.

[32] S. Basu, S. Suresh, K. Ghatak, S.F. Bartolucci, T. Gupta, P. Hundekar, R. Kumar, T.-M. Lu, D. Datta, Y. Shi, Utilizing van der Waals slippery interfaces to enhance the electrochemical stability of Silicon film anodes in Lithium-ion batteries, ACS Applied Materials & Interfaces (2018).

[33] K. Rana, J. Singh, J.-T. Lee, J.H. Park, J.-H. Ahn, Highly conductive freestanding graphene films as anode current collectors for flexible lithium-ion batteries, ACS Applied Materials & Interfaces 6(14) (2014) 11158-11166.

[34] M.-S. Park, S. Rajendran, Y.-M. Kang, K.-S. Han, Y.-S. Han, J.-Y. Lee, Si–Ni alloy–graphite composite synthesized by arc-melting and high-energy mechanical milling for use as an anode in lithium-ion batteries, Journal of Power Sources 158(1) (2006) 650-653.

[35] G. Schmuelling, M. Winter, T. Placke, Investigating the Mg–Si binary system via combinatorial sputter deposition as high energy density anodes for lithium-ion batteries, ACS Applied Materials & Interfaces 7(36) (2015) 20124-20133.

[36] M.K. Datta, P.N. Kumta, Silicon and carbon based composite anodes for lithium ion batteries, Journal of Power Sources 158(1) (2006) 557-563.

[37] J. Shu, H. Li, R. Yang, Y. Shi, X. Huang, Cage-like carbon nanotubes/Si composite as anode material for lithium ion batteries, Electrochemistry Communications 8(1) (2006) 51-54.

[38] J. Maranchi, A. Hepp, A. Evans, N. Nuhfer, P. Kumta, Interfacial properties of the a-Si⁄Cu: active–inactive thin-film anode system for lithium-ion batteries, Journal of the Electrochemical Society 153(6) (2006) A1246-A1253.

[39] K.S. Novoselov, A.K. Geim, S.V. Morozov, D. Jiang, Y. Zhang, S.V. Dubonos, I.V. Grigorieva, A.A. Firsov, Electric field effect in atomically thin carbon films, Science 306(5696) (2004) 666-669.

[40] X. Li, L. Zhi, Graphene hybridization for energy storage applications, Chemical Society Reviews 47(9) (2018) 3189-3216.

[41] E. Pomerantseva, Y. Gogotsi, Two-dimensional heterostructures for energy storage, Nature Energy 2(7) (2017) 1-6.

[42] H. Wang, F. Liu, W. Fu, Z. Fang, W. Zhou, Z. Liu, Two-dimensional heterostructures: fabrication, characterization, and application, Nanoscale 6(21) (2014) 12250-12272.

[43] S. Gbadamasi, M. Mohiuddin, V. Krishnamurthi, R. Verma, M.W. Khan, S. Pathak, K. Kalantar-Zadeh, N. Mahmood, Interface chemistry of two-dimensional heterostructures–fundamentals to applications, Chemical Society Reviews (2021).

[44] D. Purdie, N. Pugno, T. Taniguchi, K. Watanabe, A. Ferrari, A. Lombardo, Cleaning interfaces in layered materials heterostructures, Nature communications 9(1) (2018) 1-12.

[45] J.K. Lee, K.B. Smith, C.M. Hayner, H.H. Kung, Silicon nanoparticles–graphene paper composites for Li ion battery anodes, Chemical communications 46(12) (2010) 2025-2027.

[46] B. Wang, X. Li, B. Luo, L. Hao, M. Zhou, X. Zhang, Z. Fan, L. Zhi, Approaching the downsizing limit of silicon for surface-controlled lithium storage, Advanced Materials 27(9) (2015) 1526-1532.

[47] X. Zhao, C.M. Hayner, M.C. Kung, H.H. Kung, In-plane vacancy-enabled high-power Si–graphene composite electrode for lithium-ion batteries, Advanced Energy Materials 1(6) (2011) 1079-1084.

[48] Y. Zhao, X. Li, B. Yan, D. Li, S. Lawes, X. Sun, Significant impact of 2D graphene nanosheets on large volume change tin-based anodes in lithium-ion batteries: a review, Journal of Power Sources 274 (2015) 869-884.

[49] B. Luo, T. Qiu, D. Ye, L. Wang, L. Zhi, Tin nanoparticles encapsulated in graphene backboned carbonaceous foams as high-performance anodes for lithium-ion and sodium-ion storage, Nano Energy 22 (2016) 232-240.

[50] B. Luo, B. Wang, X. Li, Y. Jia, M. Liang, L. Zhi, Graphene-confined Sn nanosheets with enhanced lithium storage capability, Advanced Materials 24(26) (2012) 3538-3543.

[51] A.M. Chockla, M.G. Panthani, V.C. Holmberg, C.M. Hessel, D.K. Reid, T.D. Bogart, J.T. Harris, C.B. Mullins, B.A. Korgel, Electrochemical lithiation of graphene-supported silicon and germanium for rechargeable batteries, The Journal of Physical Chemistry C 116(22) (2012) 11917-11923.

[52] D. Li, K.H. Seng, D. Shi, Z. Chen, H.K. Liu, Z. Guo, A unique sandwich-structured C/Ge/graphene nanocomposite as an anode material for high power lithium ion batteries, Journal of Materials Chemistry A 1(45) (2013) 14115-14121.

[53] J. Cheng, J. Du, Facile synthesis of germanium–graphene nanocomposites and their application as anode materials for lithium ion batteries, CrystEngComm 14(2) (2012) 397-400.

[54] S. Abbas, High-performance graphene/sulphur electrodes for flexible Li-ion batteries using the low-temperature spraying method, Nanoscale 7(17) (2015) 8093-8100.

[55] K. Xi, P.R. Kidambi, R. Chen, C. Gao, X. Peng, C. Ducati, S. Hofmann, R.V. Kumar, Binder free three-dimensional sulphur/few-layer graphene foam cathode with enhanced high-rate capability for rechargeable lithium sulphur batteries, Nanoscale 6(11) (2014) 5746-5753.

[56] J. Zhang, Y. Xu, L. Fan, Y. Zhu, J. Liang, Y. Qian, Graphene–encapsulated selenium/polyaniline core–shell nanowires with enhanced electrochemical performance for Li–Se batteries, Nano Energy 13 (2015) 592-600.

[57] D. Kundu, F. Krumeich, R. Nesper, Investigation of nano-fibrous selenium and its polypyrrole and graphene composite as cathode material for rechargeable Li-batteries, Journal of Power Sources 236 (2013) 112-117.

[58] X. Zhang, L. Huang, P. Zeng, L. Wu, Q. Shen, Z. Gao, Y. Chen, Hierarchical MoS2 anchored on core-shell Si@ C with increased active-sites and charge transfer for superior cycling and rate capability in lithium-ion batteries, Chemical Engineering Journal 357 (2019) 625-632.

[59] S. Wang, B.Y. Guan, L. Yu, X.W. Lou, Rational design of three-layered TiO2@ Carbon@ MoS2 hierarchical nanotubes for enhanced lithium storage, Advanced Materials 29(37) (2017) 1702724.

[60] U.V. Kawade, A.A. Ambalkar, R.P. Panmand, R.S. Kalubarme, S.R. Kadam, S.D. Naik, M.V. Kulkarni, B.B. Kale, Silicon nanoparticle-sandwiched ultrathin MoS 2–graphene layers as an anode material for Li-ion batteries, Materials Chemistry Frontiers 3(4) (2019) 587-596.

[61] M. Naguib, M. Kurtoglu, V. Presser, J. Lu, J. Niu, M. Heon, L. Hultman, Y. Gogotsi, M.W. Barsoum, Two-dimensional nanocrystals produced by exfoliation of Ti3AlC2, Advanced Materials 23(37) (2011) 4248-4253.

[62] J. Pang, R.G. Mendes, A. Bachmatiuk, L. Zhao, H.Q. Ta, T. Gemming, H. Liu, Z. Liu, M.H. Rummeli, Applications of 2D MXenes in energy conversion and storage systems, Chemical Society Reviews 48(1) (2019) 72-133.

[63] F. Kong, X. He, Q. Liu, X. Qi, D. Sun, Y. Zheng, R. Wang, Y. Bai, Enhanced reversible Li-ion storage in Si@ Ti3C2 MXene nanocomposite, Electrochemistry Communications 97 (2018) 16-21.

[64] C.J. Zhang, S.-H. Park, A. Seral-Ascaso, S. Barwich, N. McEvoy, C.S. Boland, J.N. Coleman, Y. Gogotsi, V. Nicolosi, High capacity silicon anodes enabled by MXene viscous aqueous ink, Nature Communications 10(1) (2019) 1-9.

[65] H. Böhm, G. Beyermann, ZEBRA batteries, enhanced power by doping, Journal of Power Sources 84(2) (1999) 270-274.

[66] C. Nithya, S. Gopukumar, Sodium ion batteries: a newer electrochemical storage, Wiley Interdisciplinary Reviews: Energy and Environment 4(3) (2015) 253-278.

[67] N. Yabuuchi, K. Kubota, M. Dahbi, S. Komaba, Research development on sodium-ion batteries, Chemical Reviews 114(23) (2014) 11636-11682.

[68] D. Kundu, E. Talaie, V. Duffort, L.F. Nazar, The emerging chemistry of sodium ion batteries for electrochemical energy storage, Angewandte Chemie International Edition 54(11) (2015) 3431-3448.

[69] M. Stojić, D. Kostić, B. Stošić, The behaviour of sodium in Ge, Si and GaAs, Physica B+ C 138(1-2) (1986) 125-128.

[70] C. Delmas, C. Fouassier, P. Hagenmuller, Structural classification and properties of the layered oxides, Physica B+ C 99(1-4) (1980) 81-85.

[71] R. Berthelot, D. Carlier, C. Delmas, Electrochemical investigation of the P2–NaxCoO2 phase diagram, Nature Materials 10(1) (2011) 74-80.

[72] K. Shiva, P. Singh, W. Zhou, J.B. Goodenough, NaFe 2 PO 4 (SO 4) 2: a potential cathode for a Na-ion battery, Energy & Environmental Science 9(10) (2016) 3103-3106.

[73] J. Xu, D.H. Lee, Y.S. Meng, Recent advances in sodium intercalation positive electrode materials for sodium ion batteries, Functional Materials Letters 6(01) (2013) 1330001.

[74] Y. Okamoto, Density functional theory calculations of alkali metal (Li, Na, and K) graphite intercalation compounds, The Journal of Physical Chemistry C 118(1) (2013) 16-19.

[75] M.-S. Balogun, Y. Luo, W. Qiu, P. Liu, Y. Tong, A review of carbon materials and their composites with alloy metals for sodium ion battery anodes, Carbon 98 (2016) 162-178.

[76] V. Chevrier, G. Ceder, Challenges for Na-ion negative electrodes, Journal of The Electrochemical Society 158(9) (2011) A1011-A1014.

[77] B. Jache, P. Adelhelm, Use of Graphite as a Highly Reversible Electrode with Superior Cycle Life for Sodium-Ion Batteries by Making Use of Co-Intercalation Phenomena, Angewandte Chemie International Edition 53(38) (2014) 10169-10173.

[78] Y. Wen, K. He, Y. Zhu, F. Han, Y. Xu, I. Matsuda, Y. Ishii, J. Cumings, C. Wang, Expanded graphite as superior anode for sodium-ion batteries, Nature communications 5 (2014) 4033.

[79] Y. Mei, Y. Huang, X. Hu, Nanostructured Ti-based anode materials for Na-ion batteries, Journal of Materials Chemistry A 4(31) (2016) 12001-12013.

[80] F. Legrain, O. Malyi, S. Manzhos, Insertion energetics of lithium, sodium, and magnesium in crystalline and amorphous titanium dioxide: A comparative first-principles study, Journal of Power Sources 278 (2015) 197-202.

[81] W. Li, M. Zhou, H. Li, K. Wang, S. Cheng, K. Jiang, A high performance sulfur-doped disordered carbon anode for sodium ion batteries, Energy & Environmental Science 8(10) (2015) 2916-2921.

[82] F. Klein, B. Jache, A. Bhide, P. Adelhelm, Conversion reactions for sodium-ion batteries, Physical Chemistry Chemical Physics 15(38) (2013) 15876-15887.

[83] M. Mortazavi, Q. Ye, N. Birbilis, N.V. Medhekar, High capacity group-15 alloy anodes for Na-ion batteries: Electrochemical and mechanical insights, Journal of Power Sources 285 (2015) 29-36.

[84] M. Mortazavi, J. Deng, V.B. Shenoy, N.V. Medhekar, Elastic softening of alloy negative electrodes for Na-ion batteries, Journal of Power Sources 225 (2013) 207-214.

[85] D. Stevens, J. Dahn, An In Situ Small-Angle X-Ray Scattering Study of Sodium Insertion into a Nanoporous Carbon Anode Material within an Operating Electrochemical Cell, Journal of The Electrochemical Society 147(12) (2000) 4428-4431.

[86] Y.-X. Wang, S.-L. Chou, H.-K. Liu, S.-X. Dou, Reduced graphene oxide with superior cycling stability and rate capability for sodium storage, Carbon 57 (2013) 202-208.

[87] D. Li, L. Zhang, H. Chen, J. Wang, L.-X. Ding, S. Wang, P.J. Ashman, H. Wang, Graphene-based nitrogen-doped carbon sandwich nanosheets: a new capacitive process controlled anode material for high-performance sodium-ion batteries, Journal of Materials Chemistry A 4(22) (2016) 8630-8635.

[88] H. Usui, S. Yoshioka, K. Wasada, M. Shimizu, H. Sakaguchi, Nb-doped rutile TiO2: a potential anode material for Na-ion battery, ACS Applied Materials & Interfaces 7(12) (2015) 6567-6573.

[89] T. Umebayashi, T. Yamaki, H. Itoh, K. Asai, Band gap narrowing of titanium dioxide by sulfur doping, Applied Physics Letters 81(3) (2002) 454-456.

[90] S. Fu, J. Ni, Y. Xu, Q. Zhang, L. Li, Hydrogenation driven conductive Na2Ti3O7 nanoarrays as robust binder-free anodes for Sodium-ion batteries, Nano letters 16(7) (2016) 4544-4551.

[91] H. Li, H. Fei, X. Liu, J. Yang, M. Wei, In situ synthesis of Na 2 Ti 7 O 15 nanotubes on a Ti net substrate as a high performance anode for Na-ion batteries, Chemical Communications 51(45) (2015) 9298-9300.

[92] S.C. Jung, D.S. Jung, J.W. Choi, Y.-K. Han, Atom-level understanding of the sodiation process in silicon anode material, The Journal of Physical Chemistry Letters 5(7) (2014) 1283-1288.

[93] P.R. Abel, Y.-M. Lin, T. de Souza, C.-Y. Chou, A. Gupta, J.B. Goodenough, G.S. Hwang, A. Heller, C.B. Mullins, Nanocolumnar germanium thin films as a high-rate sodium-ion battery anode material, The Journal of Physical Chemistry C 117(37) (2013) 18885-18890.

[94] S. Komaba, Y. Matsuura, T. Ishikawa, N. Yabuuchi, W. Murata, S. Kuze, Redox reaction of Sn-polyacrylate electrodes in aprotic Na cell, Electrochemistry Communications 21 (2012) 65-68.

[95] J.C. Pramudita, D. Sehrawat, D. Goonetilleke, N. Sharma, An initial review of the status of electrode materials for potassium-ion batteries, Advanced Energy Materials 7(24) (2017) 1602911.

[96] S. Komaba, T. Hasegawa, M. Dahbi, K. Kubota, Potassium intercalation into graphite to realize high-voltage/high-power potassium-ion batteries and potassium-ion capacitors, Electrochemistry Communications 60 (2015) 172-175.

[97] K. Nobuhara, H. Nakayama, M. Nose, S. Nakanishi, H. Iba, First-principles study of alkali metal-graphite intercalation compounds, Journal of Power Sources 243 (2013) 585-587.

[98] M.H. Han, E. Gonzalo, G. Singh, T. Rojo, A comprehensive review of sodium layered oxides: powerful cathodes for Na-ion batteries, Energy & Environmental Science 8(1) (2015) 81-102.

[99] C. Vaalma, G.A. Giffin, D. Buchholz, S. Passerini, Non-aqueous K-ion battery based on layered K0. 3MnO2 and hard carbon/carbon black, Journal of The Electrochemical Society 163(7) (2016) A1295.

[100] C. Zhang, Y. Xu, M. Zhou, L. Liang, H. Dong, M. Wu, Y. Yang, Y. Lei, Potassium Prussian blue nanoparticles: a low-cost cathode material for potassium-ion batteries, Advanced Functional Materials 27(4) (2017) 1604307.

[101] E. Nossol, V.H. Souza, A.J. Zarbin, Carbon nanotube/Prussian blue thin films as cathodes for flexible, transparent and ITO-free potassium secondary battery, Journal of Colloid and Interface Science 478 (2016) 107-116.

[102] C.D. Wessells, S.V. Peddada, R.A. Huggins, Y. Cui, Nickel hexacyanoferrate nanoparticle electrodes for aqueous sodium and potassium ion batteries, Nano Letters 11(12) (2011) 5421-5425.

[103] D. Su, A. McDonagh, S.Z. Qiao, G. Wang, High-capacity aqueous potassium-ion batteries for large-scale energy storage, Advanced Materials 29(1) (2017) 1604007.

[104] Y. Chen, W. Luo, M. Carter, L. Zhou, J. Dai, K. Fu, S. Lacey, T. Li, J. Wan, X. Han, Organic electrode for non-aqueous potassium-ion batteries, Nano Energy 18 (2015) 205-211.

[105] Z. Jian, Y. Liang, I.A. Rodríguez-Pérez, Y. Yao, X. Ji, Poly (anthraquinonyl sulfide) cathode for potassium-ion batteries, Electrochemistry Communications 71 (2016) 5-8.

[106] M. Steinhauser, Multiscale modeling of fluids and solids-theory and applications, ASIN 3540751165 (2008).

[107] J.T. Oden, K. Vemaganti, N. Moës, Hierarchical modeling of heterogeneous solids, Computer Methods in Applied Mechanics and Engineering 172(1-4) (1999) 3-25.

[108] M.F. Horstemeyer, Multiscale modeling: a review, Practical Aspects of Computational Chemistry (2009) 87-135.

[109] X. Zheng, P. Zheng, R.-Z. Zhang, Machine learning material properties from the periodic table using convolutional neural networks, Chemical Science 9(44) (2018) 8426-8432.

[110] J. Wei, X. Chu, X.Y. Sun, K. Xu, H.X. Deng, J. Chen, Z. Wei, M. Lei, Machine learning in materials science, InfoMat 1(3) (2019) 338-358.

[111] G. Pilania, C. Wang, X. Jiang, S. Rajasekaran, R. Ramprasad, Accelerating materials property predictions using machine learning, Scientific Reports 3(1) (2013) 1-6.

[112] P. Hohenberg, W. Kohn, Inhomogeneous electron gas, Physical Review 136(3B) (1964) B864.

[113] W. Kohn, L.J. Sham, Self-consistent equations including exchange and correlation effects, Physical review 140(4A) (1965) A1133.

[114] J. Kohanoff, Electronic structure calculations for solids and molecules: theory and computational methods, Cambridge university press 2006.

[115] P. Lykos, G. Pratt, Discussion on the Hartree-Fock approximation, Reviews of Modern Physics 35(3) (1963) 496.

[116] M. Born, J.R. Oppenheimer, On the quantum theory of molecules, Сборник статей к мультимедийному электронному учебно-методическому комплексу по дисциплине «физика атома и атомных явлений»/отв. ред. Шундалов МБ; БГУ, Физический факультет (1927).

[117] M. Aydinol, A. Kohan, G. Ceder, K. Cho, J. Joannopoulos, Ab initio study of lithium intercalation in metal oxides and metal dichalcogenides, Physical Review B 56(3) (1997) 1354.

[118] H. Kim, C.-Y. Chou, J.G. Ekerdt, G.S. Hwang, Structure and properties of Li− Si alloys: a first-principles study, The Journal of Physical Chemistry C 115(5) (2011) 2514-2521.

[119] J.P. Perdew, K. Burke, M. Ernzerhof, Generalized gradient approximation made simple, Physical review letters 77(18) (1996) 3865.

[120] Y. Li, S. Huang, C. Wei, D. Zhou, B. Li, C. Wu, V.N. Mochalin, Adhesion Between MXenes and Other 2D Materials, ACS Applied Materials & Interfaces 13(3) (2021) 4682-4691.

[121] M.E. Stournara, X. Xiao, Y. Qi, P. Johari, P. Lu, B.W. Sheldon, H. Gao, V.B. Shenoy, Li segregation induces structure and strength changes at the amorphous Si/Cu interface, Nano Letters 13(10) (2013) 4759-4768.

[122] X.-Y. Fan, F.-S. Ke, G.-Z. Wei, L. Huang, S.-G. Sun, Sn–Co alloy anode using porous Cu as current collector for lithium ion battery, Journal of Alloys and Compounds 476(1-2) (2009) 70-73.

[123] S. Kang, H. Xie, W. Zhai, Z. Ma, R. Wang, W. Zhang, Enhancing performance of a lithium ion battery by optimizing the surface properties of the current collector, International Journal of Electrochemical Science 10 (2015) 2324-2335.

[124] H. Jeon, I. Cho, H. Jo, K. Kim, M.-H. Ryou, Y.M. Lee, Highly rough copper current collector: improving adhesion property between a silicon electrode and current collector for flexible lithium-ion batteries, RSC Advances 7(57) (2017) 35681-35686.

[125] S. Basu, S. Suresh, K. Ghatak, S.F. Bartolucci, T. Gupta, P. Hundekar, R. Kumar, T.-M. Lu, D. Datta, Y. Shi, Utilizing van der Waals slippery interfaces to enhance the electrochemical stability of silicon film anodes in lithium-ion batteries, ACS Applied Materials & Interfaces 10(16) (2018) 13442-13451.

[126] M.E. Stournara, Y. Qi, V.B. Shenoy, From ab initio calculations to multiscale design of Si/C core–shell particles for Li-ion anodes, Nano Letters 14(4) (2014) 2140-2149.

[127] X. Feng, M. Ouyang, X. Liu, L. Lu, Y. Xia, X. He, Thermal runaway mechanism of lithium ion battery for electric vehicles: A review, Energy Storage Materials 10 (2018) 246-267.

[128] A. Naha, A. Khandelwal, S. Agarwal, P. Tagade, K.S. Hariharan, A. Kaushik, A. Yadu, S.M. Kolake, S. Han, B. Oh, Internal short circuit detection in Li-ion batteries using supervised machine learning, Scientific Reports 10(1) (2020) 1-10.

[129] S. Suresh, Z.P. Wu, S.F. Bartolucci, S. Basu, R. Mukherjee, T. Gupta, P. Hundekar, Y. Shi, T.-M. Lu, N. Koratkar, Protecting silicon film anodes in lithium-ion batteries using an atomically thin graphene drape, ACS Nano 11(5) (2017) 5051-5061.

[130] T. Foroozan, F.A. Soto, V. Yurkiv, S. Sharifi-Asl, R. Deivanayagam, Z. Huang, R. Rojaee, F. Mashayek, P.B. Balbuena, R. Shahbazian-Yassar, Synergistic effect of graphene oxide for impeding the dendritic plating of Li, Advanced Functional Materials 28(15) (2018) 1705917.

[131] M. Aykol, P. Herring, A. Anapolsky, Machine learning for continuous innovation in battery technologies, Nature Reviews Materials 5(10) (2020) 725-727.

[132] V.L. Deringer, Modelling and understanding battery materials with machine-learning-driven atomistic simulations, Journal of Physics: Energy 2(4) (2020) 041003.

[133] S.K. Kauwe, T.D. Rhone, T.D. Sparks, Data-driven studies of li-ion-battery materials, Crystals 9(1) (2019) 54.

[134] G. Houchins, V. Viswanathan, An accurate machine-learning calculator for optimization of Li-ion battery cathodes, The Journal of Chemical Physics 153(5) (2020) 054124.

[135] A. Dave, J. Mitchell, K. Kandasamy, H. Wang, S. Burke, B. Paria, B. Póczos, J. Whitacre, V. Viswanathan, Autonomous discovery of battery electrolytes with robotic experimentation and machine learning, Cell Reports Physical Science 1(12) (2020) 100264.

[136] I.A. Moses, R.P. Joshi, B. Ozdemir, N. Kumar, J. Eickholt, V. Barone, Machine Learning Screening of Metal-Ion Battery Electrode Materials, ACS Applied Materials & Interfaces (2021).

[137] S.M. Moosavi, K.M. Jablonka, B. Smit, The role of machine learning in the understanding and design of materials, Journal of the American Chemical Society 142(48) (2020) 20273-20287.

[138] R.P. Joshi, J. Eickholt, L. Li, M. Fornari, V. Barone, J.E. Peralta, Machine learning the voltage of electrode materials in metal-ion batteries, ACS Applied Materials & Interfaces 11(20) (2019) 18494-18503.

[139] M. Chandran, S. Lee, J.-H. Shim, Machine learning assisted first-principles calculation of multicomponent solid solutions: estimation of interface energy in Ni-based superalloys, Modelling and Simulation in Materials Science and Engineering 26(2) (2018) 025010.

[140] O.I. Malyi, T.L. Tan, S. Manzhos, A comparative computational study of structures, diffusion, and dopant interactions between Li and Na insertion into Si, Applied Physics Express 6(2) (2013) 027301.

[141] V.V. Kulish, O.I. Malyi, M.-F. Ng, Z. Chen, S. Manzhos, P. Wu, Controlling Na diffusion by rational design of Si-based layered architectures, Physical Chemistry Chemical Physics 16(9) (2014) 4260-4267.

[142] G. Kresse, J. Furthmüller, Efficient iterative schemes for ab initio total-energy calculations using a plane-wave basis set, Physical Review B 54(16) (1996) 11169.

[143] P.E. Blöchl, Projector augmented-wave method, Physical Review B 50(24) (1994) 17953.

[144] G. Kresse, D. Joubert, From ultrasoft pseudopotentials to the projector augmented-wave method, Physical Review B 59(3) (1999) 1758.

[145] L. Baggetto, J.K. Keum, J.F. Browning, G.M. Veith, Germanium as negative electrode material for sodium-ion batteries, Electrochemistry Communications 34 (2013) 41-44.

[146] P. Johari, Y. Qi, V.B. Shenoy, The mixing mechanism during lithiation of Si negative electrode in Li-ion batteries: an ab initio molecular dynamics study, Nano Letters 11(12) (2011) 5494-5500.

[147] J.-Y. Hwang, S.-T. Myung, Y.-K. Sun, Sodium-ion batteries: present and future, Chemical Society Reviews 46(12) (2017) 3529-3614.

[148] R. Grigorovici, R. Mănăilă, Short-range order in amorphous germanium, Journal of Non-Crystalline Solids 1(5) (1969) 371-387.

[149] S.C. Jung, H.-J. Kim, Y.-J. Kang, Y.-K. Han, Advantages of Ge anode for Na-ion batteries: Ge vs. Si and Sn, Journal of Alloys and Compounds 688 (2016) 158-163.

[150] L. Baggetto, P. Ganesh, R.P. Meisner, R.R. Unocic, J.-C. Jumas, C.A. Bridges, G.M. Veith, Characterization of sodium ion electrochemical reaction with tin anodes: experiment and theory, Journal of Power Sources 234 (2013) 48-59.

[151] P.M. Panchmatia, A.R. Armstrong, P.G. Bruce, M.S. Islam, Lithium-ion diffusion mechanisms in the battery anode material Li 1+ x V 1− x O 2, Physical Chemistry Chemical Physics 16(39) (2014) 21114-21118.

[152] D. Lv, J. Zheng, Q. Li, X. Xie, S. Ferrara, Z. Nie, L.B. Mehdi, N.D. Browning, J.G. Zhang, G.L. Graff, High energy density lithium–sulfur batteries: challenges of thick sulfur cathodes, Advanced Energy Materials 5(16) (2015) 1402290.

[153] Y.V. Mikhaylik, J.R. Akridge, Polysulfide shuttle study in the Li/S battery system, Journal of the Electrochemical Society 151(11) (2004) A1969.

[154] Q. Pang, X. Liang, C.Y. Kwok, L.F. Nazar, Advances in lithium–sulfur batteries based on multifunctional cathodes and electrolytes, Nature Energy 1(9) (2016) 1-11.

[155] G. Xu, B. Ding, J. Pan, P. Nie, L. Shen, X. Zhang, High performance lithium–sulfur batteries: advances and challenges, Journal of Materials Chemistry A 2(32) (2014) 12662-12676.

[156] D. Su, D. Zhou, C. Wang, G. Wang, Lithium-Sulfur Batteries: Toward High Performance Lithium–Sulfur Batteries Based on Li2S Cathodes and Beyond: Status, Challenges, and Perspectives (Adv. Funct. Mater. 38/2018), Advanced Functional Materials 28(38) (2018) 1870273.

[157] J. Zhang, Y.X. Yin, Y. You, Y. Yan, Y.G. Guo, A High-Capacity Tellurium@ Carbon Anode Material for Lithium-Ion Batteries, Energy Technology 2(9-10) (2014) 757-762.

[158] Y. Liu, J. Wang, Y. Xu, Y. Zhu, D. Bigio, C. Wang, Lithium–tellurium batteries based on tellurium/porous carbon composite, Journal of Materials Chemistry A 2(31) (2014) 12201-12207.

[159] J.-U. Seo, G.-K. Seong, C.-M. Park, Te/C nanocomposites for Li-Te secondary batteries, Scientific reports 5(1) (2015) 1-7.

[160] N. Ding, S.F. Chen, D.S. Geng, S.W. Chien, T. An, T.A. Hor, Z.L. Liu, S.H. Yu, Y. Zong, Tellurium@ Ordered Macroporous Carbon Composite and Free-Standing Tellurium Nanowire Mat as Cathode Materials for Rechargeable Lithium–Tellurium Batteries, Advanced Energy Materials 5(8) (2015) 1401999.

[161] A. Abouimrane, D. Dambournet, K.W. Chapman, P.J. Chupas, W. Weng, K. Amine, A new class of lithium and sodium rechargeable batteries based on selenium and selenium–sulfur as a positive electrode, Journal of the American chemical society 134(10) (2012) 4505-4508.

[162] L. Liu, Y. Hou, X. Wu, S. Xiao, Z. Chang, Y. Yang, Y. Wu, Nanoporous selenium as a cathode material for rechargeable lithium–selenium batteries, Chemical Communications 49(98) (2013) 11515-11517.

[163] J.T. Lee, H. Kim, M. Oschatz, D.C. Lee, F. Wu, H.T. Lin, B. Zdyrko, W.I. Cho, S. Kaskel, G. Yushin, Micro-and Mesoporous Carbide-Derived Carbon–Selenium Cathodes for High-Performance Lithium Selenium Batteries, Advanced Energy Materials 5(1) (2015) 1400981.

[164] Y. Cui, A. Abouimrane, J. Lu, T. Bolin, Y. Ren, W. Weng, C. Sun, V.A. Maroni, S.M. Heald, K. Amine, (De) Lithiation mechanism of Li/SeS x (x= 0–7) batteries determined by in situ synchrotron X-ray diffraction and X-ray absorption spectroscopy, Journal of the American Chemical Society 135(21) (2013) 8047-8056.

[165] C.P. Yang, S. Xin, Y.X. Yin, H. Ye, J. Zhang, Y.G. Guo, An advanced selenium–carbon cathode for rechargeable lithium–selenium batteries, Angewandte Chemie International Edition 52(32) (2013) 8363-8367.

[166] Z. Zhang, X. Yang, Z. Guo, Y. Qu, J. Li, Y. Lai, Selenium/carbon-rich core–shell composites as cathode materials for rechargeable lithium–selenium batteries, Journal of Power Sources 279 (2015) 88-93.

[167] J. Zhou, M. Chen, T. Wang, S. Li, Q. Zhang, M. Zhang, H. Xu, J. Liu, J. Liang, J. Zhu, Covalent Selenium Embedded in Hierarchical Carbon Nanofibers for Ultra-High Areal Capacity Li-Se Batteries, Iscience 23(3) (2020) 100919.

[168] Z. Li, L. Yuan, Z. Yi, Y. Liu, Y. Huang, Confined selenium within porous carbon nanospheres as cathode for advanced Li–Se batteries, Nano Energy 9 (2014) 229-236.

[169] I. Srivastava, D.S. Bolintineanu, J.B. Lechman, S.A. Roberts, Controlling Binder Adhesion to Impact Electrode Mesostructures and Transport, ACS Applied Materials & Interfaces 12(31) (2020) 34919-34930.

[170] A. Goldan, C. Li, S. Pennycook, J. Schneider, A. Blom, W. Zhao, Molecular structure of vapor-deposited amorphous selenium, Journal of Applied Physics 120(13) (2016) 135101.

[171] M. Dion, H. Rydberg, E. Schröder, D.C. Langreth, B.I. Lundqvist, Van der Waals density functional for general geometries, Physical Review Letters 92(24) (2004) 246401.

[172] J. Klimeš, D.R. Bowler, A. Michaelides, Chemical accuracy for the van der Waals density functional, Journal of Physics: Condensed Matter 22(2) (2009) 022201.

[173] J. Klimeš, D.R. Bowler, A. Michaelides, Van der Waals density functionals applied to solids, Physical Review B 83(19) (2011) 195131.

[174] V. Sharma, K. Ghatak, D. Datta, Amorphous germanium as a promising anode material for sodium ion batteries: a first principle study, Journal of Materials Science 53(20) (2018) 14423-14434.

[175] C. Escoffery, S. Halperin, Studies on the Polymorphic Transformation of Selenium, Transactions of The Electrochemical Society 90(1) (1946) 163.

[176] Y.-Z. Chen, Y.-T. You, P.-J. Chen, D. Li, T.-Y. Su, L. Lee, Y.-C. Shih, C.-W. Chen, C.-C. Chang, Y.-C. Wang, Environmentally and mechanically stable selenium 1D/2D hybrid structures for broad-range photoresponse from ultraviolet to infrared wavelengths, ACS Applied Materials & Interfaces 10(41) (2018) 35477-35486.

[177] M. Tao, D. Udeshi, N. Basit, E. Maldonado, W.P. Kirk, Removal of dangling bonds and surface states on silicon (001) with a monolayer of selenium, Applied Physics Letters 82(10) (2003) 1559-1561.

[178] M. Lannoo, The role of dangling bonds in the properties of surfaces and interfaces of semiconductors, Revue de Physique Appliquée 25(9) (1990) 887-894.

[179] E. Sanville, S.D. Kenny, R. Smith, G. Henkelman, Improved grid-based algorithm for Bader charge allocation, Journal of Computational Chemistry 28(5) (2007) 899-908.

[180] F. Sen, Y. Qi, A. Alpas, Anchoring platinum on graphene using metallic adatoms: a first principles investigation, Journal of Physics: Condensed Matter 24(22) (2012) 225003.

[181] K. Nakada, A. Ishii, Migration of adatom adsorption on graphene using DFT calculation, Solid State Communications 151(1) (2011) 13-16.

[182] M. Peressi, N. Binggeli, A. Baldereschi, Band engineering at interfaces: theory and numerical experiments, Journal of Physics D: Applied Physics 31(11) (1998) 1273.

[183] D. Li, L. Guo, L. Li, H. Lu, Electron work function–a probe for interfacial diagnosis, Scientific reports 7(1) (2017) 1-8.

[184] Y. Liu, Z. Tai, Q. Zhang, H. Wang, W.K. Pang, H.K. Liu, K. Konstantinov, Z. Guo, A new energy storage system: Rechargeable potassium-selenium battery, Nano Energy 35 (2017) 36-43.

[185] X. Zhou, L. Wang, Y. Yao, Y. Jiang, R. Xu, H. Wang, X. Wu, Y. Yu, Integrating Conductivity, Captivity, and Immobility Ability into N/O Dual-Doped Porous Carbon Nanocage Anchored with CNT as an Effective Se Host for Advanced K-Se Battery, Advanced Functional Materials 30(43) (2020) 2003871.

[186] X. Huang, W. Wang, J. Deng, W. Gao, D. Liu, Q. Ma, M. Xu, A Se-hollow porous carbon composite for high-performance rechargeable K–Se batteries, Inorganic Chemistry Frontiers 6(8) (2019) 2118-2125.

[187] X. Huang, J. Deng, Y. Qi, D. Liu, Y. Wu, W. Gao, W. Zhong, F. Zhang, S. Bao, M. Xu, A highly-effective nitrogen-doped porous carbon sponge electrode for advanced K–Se batteries, Inorganic Chemistry Frontiers 7(5) (2020) 1182-1189.

[188] J.K. Kim, Y.C. Kang, Encapsulation of Se into Hierarchically Porous Carbon Microspheres with Optimized Pore Structure for Advanced Na–Se and K–Se Batteries, ACS Nano 14(10) (2020) 13203-13216.

[189] D. Li, L. Wang, X. Cheng, Y. Yao, Y. Jiang, P. Shi, Y. Wu, X. Wu, C. Ma, Y. Yu, Manipulating selenium molecular configuration in N/O dual-doped porous carbon for high performance potassium-ion storage, Journal of Energy Chemistry 62 (2021) 581-589.

[190] R. Xu, Y. Yao, H. Wang, Y. Yuan, J. Wang, H. Yang, Y. Jiang, P. Shi, X. Wu, Z. Peng, Unraveling the Nature of Excellent Potassium Storage in Small-Molecule Se@ Peapod-Like N-Doped Carbon Nanofibers, Advanced Materials 32(52) (2020) 2003879.

[191] R. Cai, X. Chen, P. Liu, T. Chen, W. Liu, X. Fan, B. Ouyang, K. Liu, A Novel Cathode Based on Selenium Confined in Biomass Carbon and Graphene Oxide for Potassium-Selenium Battery, ChemElectroChem 7(21) (2020) 4477-4483.

[192] X.L. Huang, Z. Guo, S.X. Dou, Z.M. Wang, Rechargeable Potassium–Selenium Batteries, Advanced Functional Materials (2021) 2102326.

[193] N. Deng, Y. Feng, G. Wang, X. Wang, L. Wang, Q. Li, L. Zhang, W. Kang, B. Cheng, Y. Liu, Rational structure designs of 2D materials and their applications toward advanced lithium-sulfur battery and lithium-selenium battery, Chemical Engineering Journal 401 (2020) 125976.

[194] J. Ding, H. Zhou, H. Zhang, T. Stephenson, Z. Li, D. Karpuzov, D. Mitlin, Exceptional energy and new insight with a sodium–selenium battery based on a carbon nanosheet cathode and a pseudographite anode, Energy & Environmental Science 10(1) (2017) 153-165.

[195] K. Han, Z. Liu, H. Ye, F. Dai, Flexible self-standing graphene–Se@ CNT composite film as a binder-free cathode for rechargeable Li–Se batteries, Journal of Power Sources 263 (2014) 85-89.

[196] D. Huang, S. Li, Y. Luo, X. Xiao, L. Gao, M. Wang, Y. Shen, Graphene oxide-protected three dimensional Se as a binder-free cathode for Li-Se battery, Electrochimica Acta 190 (2016) 258-263.

[197] C. Luo, Y. Xu, Y. Zhu, Y. Liu, S. Zheng, Y. Liu, A. Langrock, C. Wang, Selenium@ mesoporous carbon composite with superior lithium and sodium storage capacity, ACS Nano 7(9) (2013) 8003-8010.

[198] X. Peng, L. Wang, X. Zhang, B. Gao, J. Fu, S. Xiao, K. Huo, P.K. Chu, Reduced graphene oxide encapsulated selenium nanoparticles for high-power lithium–selenium battery cathode, Journal of Power Sources 288 (2015) 214-220.

[199] K. Han, Z. Liu, J. Shen, Y. Lin, F. Dai, H. Ye, A free-standing and ultralong-life lithium-selenium battery cathode enabled by 3D mesoporous carbon/graphene hierarchical architecture, Advanced Functional Materials 25(3) (2015) 455-463.

[200] L. Sha, P. Gao, X. Ren, Q. Chi, Y. Chen, P. Yang, A Self-Repairing Cathode Material for Lithium–Selenium Batteries: Se− C Chemically Bonded Selenium–Graphene Composite, Chemistry–A European Journal 24(9) (2018) 2151-2156.

[201] G.-L. Xu, T. Ma, C.-J. Sun, C. Luo, L. Cheng, Y. Ren, S.M. Heald, C. Wang, L. Curtiss, J. Wen, Insight into the capacity fading mechanism of amorphous Se2S5 confined in micro/mesoporous carbon matrix in ether-based electrolytes, Nano Letters 16(4) (2016) 2663-2673.

[202] V. Sharma, D. Mitlin, D. Datta, Understanding the Strength of the Selenium–Graphene Interfaces for Energy Storage Systems, Langmuir 37(6) (2021) 2029-2039.

[203] K. Nakada, A. Ishii, First-principles investigation of charge density analysis of various adatom adsorptions on graphene, AIP Conference Proceedings, American Institute of Physics, 2011, pp. 793-794.

[204] C. Liu, Z.G. Neale, G. Cao, Understanding electrochemical potentials of cathode materials in rechargeable batteries, Materials Today 19(2) (2016) 109-123.

[205] G. Ceder, K. Persson, The materials project: A materials genome approach, 2010.

[206] G.-L. Xu, J. Liu, R. Amine, Z. Chen, K. Amine, Selenium and selenium–sulfur chemistry for rechargeable lithium batteries: interplay of cathode structures, electrolytes, and interfaces, ACS Energy Letters 2(3) (2017) 605-614.

[207] S. Mukherjee, L. Kavalsky, K. Chattopadhyay, C.V. Singh, Adsorption and diffusion of lithium polysulfides over blue phosphorene for Li–S batteries, Nanoscale 10(45) (2018) 21335-21352.

[208] K. Ghatak, S. Basu, T. Das, V. Sharma, H. Kumar, D. Datta, Effect of cobalt content on the electrochemical properties and structural stability of NCA type cathode materials, Physical Chemistry Chemical Physics 20(35) (2018) 22805-22817.

[209] A. Eftekhari, The rise of lithium–selenium batteries, Sustainable energy & fuels 1(1) (2017) 14-29.

[210] X. Wang, Z. Zhang, Y. Qu, G. Wang, Y. Lai, J. Li, Solution-based synthesis of multi-walled carbon nanotube/selenium composites for high performance lithium–selenium battery, Journal of Power Sources 287 (2015) 247-252.

[211] M. Wagemaker, F.M. Mulder, A. Van der Ven, The role of surface and interface energy on phase stability of nanosized insertion compounds, Advanced Materials 21(25-26) (2009) 2703-2709.

[212] A. Van der Ven, K. Garikipati, S. Kim, M. Wagemaker, The role of coherency strains on phase stability in Li x FePO4: needle crystallites minimize coherency strain and overpotential, Journal of the Electrochemical Society 156(11) (2009) A949.

[213] Q. Li, H. Liu, Z. Yao, J. Cheng, T. Li, Y. Li, C. Wolverton, J. Wu, V.P. Dravid, Electrochemistry of selenium with sodium and lithium: Kinetics and reaction mechanism, ACS Nano 10(9) (2016) 8788-8795.

[214] Y. Zhang, Z. Mu, J. Lai, Y. Chao, Y. Yang, P. Zhou, Y. Li, W. Yang, Z. Xia, S. Guo, MXene/Si@ SiO x@ C layer-by-layer superstructure with autoadjustable function for superior stable lithium storage, ACS Nano 13(2) (2019) 2167-2175.

[215] F. Zhang, Z. Jia, C. Wang, A. Feng, K. Wang, T. Hou, J. Liu, Y. Zhang, G. Wu, Sandwich-like silicon/Ti3C2Tx MXene composite by electrostatic self-assembly for high performance lithium ion battery, Energy 195 (2020) 117047.

[216] Y. Tian, Y. An, J. Feng, Flexible and freestanding silicon/MXene composite papers for high-performance lithium-ion batteries, ACS Applied Materials & Interfaces 11(10) (2019) 10004-10011.

[217] M. Khazaei, A. Ranjbar, M. Arai, T. Sasaki, S. Yunoki, Electronic properties and applications of MXenes: a theoretical review, Journal of Materials Chemistry C 5(10) (2017) 2488-2503.

[218] M. Naguib, J. Come, B. Dyatkin, V. Presser, P.-L. Taberna, P. Simon, M.W. Barsoum, Y. Gogotsi, MXene: a promising transition metal carbide anode for lithium-ion batteries, Electrochemistry Communications 16(1) (2012) 61-64.

[219] Q. Tang, Z. Zhou, P. Shen, Are MXenes promising anode materials for Li ion batteries? Computational studies on electronic properties and Li storage capability of Ti3C2 and Ti3C2X2 (X= F, OH) monolayer, Journal of the American Chemical Society 134(40) (2012) 16909-16916.

[220] D. Er, J. Li, M. Naguib, Y. Gogotsi, V.B. Shenoy, Ti3C2 MXene as a high capacity electrode material for metal (Li, Na, K, Ca) ion batteries, ACS Applied Materials & Interfaces 6(14) (2014) 11173-11179.

[221] X. Wang, X. Shen, Y. Gao, Z. Wang, R. Yu, L. Chen, Atomic-scale recognition of surface structure and intercalation mechanism of Ti3C2X, Journal of the American Chemical Society 137(7) (2015) 2715-2721.

[222] Y.-X. Yu, Prediction of mobility, enhanced storage capacity, and volume change during sodiation on interlayer-expanded functionalized Ti3C2 MXene anode materials for sodium-ion batteries, The Journal of Physical Chemistry C 120(10) (2016) 5288-5296.

[223] C.-H. Wang, N. Kurra, M. Alhabeb, J.-K. Chang, H.N. Alshareef, Y. Gogotsi, Titanium Carbide (MXene) as a Current Collector for Lithium-Ion Batteries, ACS Omega 3(10) (2018) 12489-12494.

[224] Y. Bai, K. Zhou, N. Srikanth, J.H. Pang, X. He, R. Wang, Dependence of elastic and optical properties on surface terminated groups in two-dimensional MXene monolayers: a first-principles study, RSC Advances 6(42) (2016) 35731-35739.

[225] Y. Liu, H. Xiao, W.A. Goddard III, Schottky-barrier-free contacts with two-dimensional semiconductors by surface-engineered MXenes, Journal of the American Chemical Society 138(49) (2016) 15853-15856.

[226] T. Schultz, N.C. Frey, K. Hantanasirisakul, S. Park, S.J. May, V.B. Shenoy, Y. Gogotsi, N. Koch, Surface Termination Dependent Work Function and Electronic Properties of Ti3C2T x MXene, Chemistry of Materials 31(17) (2019) 6590-6597.

[227] J. Zhu, A. Chroneos, U. Schwingenschlögl, Nb-based MXenes for Li-ion battery applications, Physica Status Solidi (RRL)–Rapid Research Letters 9(12) (2015) 726-729.

[228] J. Zhu, U. Schwingenschlögl, P and Si functionalized MXenes for metal-ion battery applications, 2D Materials 4(2) (2017) 025073.

[229] J. Zhu, A. Chroneos, J. Eppinger, U. Schwingenschlögl, S-functionalized MXenes as electrode materials for Li-ion batteries, Applied Materials Today 5 (2016) 19-24.

[230] Q. Meng, J. Ma, Y. Zhang, Z. Li, C. Zhi, A. Hu, J. Fan, The S-functionalized Ti 3 C 2 Mxene as a high capacity electrode material for Na-ion batteries: a DFT study, Nanoscale 10(7) (2018) 3385-3392.

[231] Y. Gao, Y. Cao, Y. Gu, H. Zhuo, G. Zhuang, S. Deng, X. Zhong, Z. Wei, J. Chen, X. Pan, Functionalization Ti3C2 MXene by the adsorption or substitution of single metal atom, Applied Surface Science 465 (2019) 911-918.

[232] Y. Li, S. Huang, C. Wei, C. Wu, V.N. Mochalin, Adhesion of two-dimensional titanium carbides (MXenes) and graphene to silicon, Nature Communications 10(1) (2019) 1-8.

[233] M. Naguib, V. Mochalin, M.W. Barsoum, Y.G. Gogotsi, MXenes: A New Family of Two-Dimensional Materials--25th Anniversary Article, (2014).

[234] M. Khazaei, M. Arai, T. Sasaki, C.Y. Chung, N.S. Venkataramanan, M. Estili, Y. Sakka, Y. Kawazoe, Novel electronic and magnetic properties of two-dimensional transition metal carbides and nitrides, Advanced Functional Materials 23(17) (2013) 2185-2192.

[235] Y. Xie, M. Naguib, V.N. Mochalin, M.W. Barsoum, Y. Gogotsi, X. Yu, K.-W. Nam, X.-Q. Yang, A.I. Kolesnikov, P.R. Kent, Role of surface structure on Li-ion energy storage capacity of two-dimensional transition-metal carbides, Journal of the American Chemical Society 136(17) (2014) 6385-6394.

[236] P. Srivastava, A. Mishra, H. Mizuseki, K.-R. Lee, A.K. Singh, Mechanistic insight into the chemical exfoliation and functionalization of Ti3C2 MXene, ACS Applied Materials & Interfaces 8(36) (2016) 24256-24264.

[237] S.M. Kozlov, F. Viñes, A. Görling, Bonding mechanisms of graphene on metal surfaces, The Journal of Physical Chemistry C 116(13) (2012) 7360-7366.

[238] P. Khomyakov, G. Giovannetti, P. Rusu, G.v. Brocks, J. Van den Brink, P.J. Kelly, First-principles study of the interaction and charge transfer between graphene and metals, Physical Review B 79(19) (2009) 195425.

[239] N. Zhang, Y. Hong, S. Yazdanparast, M.A. Zaeem, Superior structural, elastic and electronic properties of 2D titanium nitride MXenes over carbide MXenes: a comprehensive first principles study, 2D Materials 5(4) (2018) 045004.

[240] M. Khazaei, A. Ranjbar, M. Ghorbani-Asl, M. Arai, T. Sasaki, Y. Liang, S. Yunoki, Nearly free electron states in MXenes, Physical Review B 93(20) (2016) 205125.

[241] E. Margine, V.H. Crespi, Universal behavior of nearly free electron states in carbon nanotubes, Physical Review Letters 96(19) (2006) 196803.

[242] J. Behler, Atom-centered symmetry functions for constructing high-dimensional neural network potentials, The Journal of Chemical Physics 134(7) (2011) 074106.

[243] Y. Zuo, C. Chen, X. Li, Z. Deng, Y. Chen, J.r. Behler, G. Csányi, A.V. Shapeev, A.P. Thompson, M.A. Wood, Performance and cost assessment of machine learning interatomic potentials, The Journal of Physical Chemistry A 124(4) (2020) 731-745.

[244] A.P. Thompson, L.P. Swiler, C.R. Trott, S.M. Foiles, G.J. Tucker, Spectral neighbor analysis method for automated generation of quantum-accurate interatomic potentials, Journal of Computational Physics 285 (2015) 316-330.

[245] A.V. Shapeev, Moment tensor potentials: A class of systematically improvable interatomic potentials, Multiscale Modeling & Simulation 14(3) (2016) 1153-1173.

[246] A.P. Bartók, M.C. Payne, R. Kondor, G. Csányi, Gaussian approximation potentials: The accuracy of quantum mechanics, without the electrons, Physical Review Letters 104(13) (2010) 136403.

[247] S. Fujikake, V.L. Deringer, T.H. Lee, M. Krynski, S.R. Elliott, G. Csányi, Gaussian approximation potential modeling of lithium intercalation in carbon nanostructures, The Journal of Chemical Physics 148(24) (2018) 241714.

[248] J. Behler, M. Parrinello, Generalized neural-network representation of high-dimensional potential-energy surfaces, Physical Review Letters 98(14) (2007) 146401.

[249] P.W. Battaglia, J.B. Hamrick, V. Bapst, A. Sanchez-Gonzalez, V. Zambaldi, M. Malinowski, A. Tacchetti, D. Raposo, A. Santoro, R. Faulkner, Relational inductive biases, deep learning, and graph networks, ArXiv preprint arXiv:1806.01261 (2018).

[250] K.T. Schütt, P.-J. Kindermans, H.E. Sauceda, S. Chmiela, A. Tkatchenko, K.-R. Müller, Schnet: A continuous-filter convolutional neural network for modeling quantum interactions, ArXiv preprint arXiv:1706.08566 (2017).

[251] H. Yanxon, D. Zagaceta, B.C. Wood, Q. Zhu, Neural network potential from bispectrum components: A case study on crystalline silicon, The Journal of Chemical Physics 153(5) (2020) 054118.

[252] S. Kondati Natarajan, J.r. Behler, Self-Diffusion of surface defects at copper–water interfaces, The Journal of Physical Chemistry C 121(8) (2017) 4368-4383.

[253] N. Artrith, A.M. Kolpak, Understanding the composition and activity of electrocatalytic nanoalloys in aqueous solvents: A combination of DFT and accurate neural network potentials, Nano Letters 14(5) (2014) 2670-2676.

[254] J. Behler, R. Martoňák, D. Donadio, M. Parrinello, Metadynamics simulations of the high-pressure phases of silicon employing a high-dimensional neural network potential, Physical Review Letters 100(18) (2008) 185501.

[255] J.r. Behler, Four Generations of High-Dimensional Neural Network Potentials, Chemical Reviews (2021).

[256] L. Zhang, J. Han, H. Wang, R. Car, E. Weinan, Deep potential molecular dynamics: a scalable model with the accuracy of quantum mechanics, Physical Review Letters 120(14) (2018) 143001.

[257] J. Han, L. Zhang, R. Car, Deep potential: A general representation of a many-body potential energy surface, ArXiv preprint arXiv:1707.01478 (2017).

[258] M. Gastegger, L. Schwiedrzik, M. Bittermann, F. Berzsenyi, P. Marquetand, wACSF—Weighted atom-centered symmetry functions as descriptors in machine learning potentials, The Journal of Chemical Physics 148(24) (2018) 241709.

[259] L. Himanen, M.O. Jäger, E.V. Morooka, F.F. Canova, Y.S. Ranawat, D.Z. Gao, P. Rinke, A.S. Foster, DScribe: Library of descriptors for machine learning in materials science, Computer Physics Communications 247 (2020) 106949.

[260] H. Gao, J. Wang, J. Sun, Improve the performance of machine-learning potentials by optimizing descriptors, The Journal of Chemical Physics 150(24) (2019) 244110.

[261] H. Yanxon, D. Zagaceta, B. Tang, D.S. Matteson, Q. Zhu, PyXtal_FF: a python library for automated force field generation, Machine Learning: Science and Technology 2(2) (2020) 027001.

[262] Z. Zhang, Improved adam optimizer for deep neural networks, 2018 IEEE/ACM 26th International Symposium on Quality of Service (IWQoS), IEEE, 2018, pp. 1-2.

[263] J. Behler, Neural network potential-energy surfaces in chemistry: a tool for large-scale simulations, Physical Chemistry Chemical Physics 13(40) (2011) 17930-17955.

[264] F. Legrain, S. Manzhos, Understanding the difference in cohesive energies between alpha and beta tin in DFT calculations, AIP Advances 6(4) (2016) 045116.

[265] M. Comin, L.J. Lewis, Deep-learning approach to the structure of amorphous silicon, Physical Review B 100(9) (2019) 094107.

[266] N. Xu, Y. Shi, Y. He, Q. Shao, A Deep-Learning Potential for Crystalline and Amorphous Li–Si Alloys, The Journal of Physical Chemistry C 124(30) (2020) 16278-16288.

[267] K. Novoselov, o.A. Mishchenko, o.A. Carvalho, A.C. Neto, 2D materials and van der Waals heterostructures, Science 353(6298) (2016).

[268] S.-H. Bae, H. Kum, W. Kong, Y. Kim, C. Choi, B. Lee, P. Lin, Y. Park, J. Kim, Integration of bulk materials with two-dimensional materials for physical coupling and applications, Nature Materials 18(6) (2019) 550-560.

[269] S. Schweiger, R. Pfenninger, W.J. Bowman, U. Aschauer, J.L. Rupp, Designing strained interface heterostructures for memristive devices, Advanced Materials 29(15) (2017) 1605049.

[270] Y. Huang, L. Zhao, L. Li, M. Xie, F. Wu, R. Chen, Electrolytes and electrolyte/electrode interfaces in sodium-ion batteries: From scientific research to practical application, Advanced Materials 31(21) (2019) 1808393.

[271] B. Moeremans, H.-W. Cheng, Q. Hu, H.F. Garces, N.P. Padture, F.U. Renner, M. Valtiner, Lithium-ion battery electrolyte mobility at nano-confined graphene interfaces, Nature Communications 7(1) (2016) 1-7.

[272] C. Wei, H. Fei, Y. Tian, Y. An, G. Zeng, J. Feng, Y. Qian, Room-temperature liquid metal confined in MXene paper as a flexible, freestanding, and binder-free anode for next-generation lithium-ion batteries, Small 15(46) (2019) 1903214.

[273] G. Guisbiers, S. Arscott, R. Snyders, An accurate determination of the surface energy of solid selenium, Applied Physics Letters 101(23) (2012) 231606.